A STUDY OF THE IRRADIANCE- AND TEMPERATURE-DEPENDENCE OF MID-WAVE-INFRARED (MWIR) ABSORPTION IN INDIUM ANTIMONIDE (InSb)

THESIS

John M. Callahan
AFIT/GEO/ENP/08-S01

DEPARTMENT OF THE AIR FORCE
AIR UNIVERSITY

AIR FORCE INSTITUTE OF TECHNOLOGY

Wright-Patterson Air Force Base, Ohio

AFIT/GEO/ENP/08-S01

A STUDY OF THE IRRADIANCE- AND TEMPERATURE-DEPENDENCE OF MID-WAVE-INFRARED (MWIR) ABSORPTION IN INDIUM ANTIMONIDE (InSb)

THESIS

Presented to the Faculty

Department of Engineering Physics

Graduate School of Engineering and Management

Air Force Institute of Technology

Air University

Air Education and Training Command

In Partial Fulfillment of the Requirements for the

Degree of Master of Science in Electrical Engineering

John M. Callahan, AA, AS, BS

August 2008

A STUDY OF THE IRRADIANCE- AND TEMPERATURE-DEPENDENCE OF MID-WAVE-INFRARED (MWIR) ABSORPTION IN INDIUM ANTIMONIDE (InSb)

John M. Callahan, AA, AS, BS

Approved:

Michael A. Marciniak (Chairman)

2 Sep 08

Date

Robert L. Hengehold (Member)

2 Sep '08

Date

Matthew J. Bohn (Member)

2 Sep 08

Date

Abstract

This work entails further investigation of the absorption of photons in indium antimonide (InSb). Previously work at the Air Force Institute of Technology (AFIT) attributed laser blooming effects in InSb focal plane arrays (FPA's) to the Burstein-Moss effect. The contributing effect is from a decrease in the absorption of the InSb material, such that the transmitted optical energy scatters off the integrated circuitry beneath the InSb thin film back into the optical system. To evaluate this, irradiance-dependent laser-absorption experiments were performed on thinned, InSb wafers prior to their FPA fabrication. The samples were illuminated with a focused CO_2 laser at 4.6 μm, and translated along the optical axis to vary the irradiance. A control process to remotely manage the experiment's apparatuses during data collection has been developed utilizing LabView 8.5. The transmission of the InSb sample was measured at different laser powers and temperatures. As the temperature decreases for a determined laser irradiance, it has been observed that the absorption decreases nonlinearly. A model of the absorption-saturation phenomena is also developed so that agreement between the measured and modeled results can be studied for the carrier lifetime and density of carriers.

To ARC

Acknowledgments

I would like to sincerely thank my faculty advisor and mentor, Dr. Michael A. Marciniak, without him this endeavor would not have been possible. I can't leave out Mike Ranft and Greg Smith, both of whom also helped me along the way. Thanks to Dr. Hengehold who believed in me, and supported me. Thanks to my fiancée, who, for many months, stood by waiting for me to finish. She's my perfect counterbalance. Thanks to my family, and extended family, for their sincere encouragement, despite having no actual interest in the subject. And, a special thanks to all my close friends, who make me a rich, rich man.

~ John M. Callahan

Table of Contents

List of Figures

Figure   Page

Figure Page

List of Tables

**A STUDY OF THE IRRADIANCE- AND TEMPERATURE-
DEPENDENCE OF MID-WAVE-INFRARED (MWIR) ABSORPTION
IN INDIUM ANTIMONIDE (InSb)**

1   Introduction

The indium antimonide (InSb) focal plane array (FPA) is an infrared (IR) electro-
optic device. Having the capability to see at night using IR wavelengths gives the InSb
FPA user a clear advantage. The FPA system must be able to distinguish between the
background and the object being observed, where the relative temperatures (IR signature)
of the two are very close. (Noise-equivalent temperature differences (NEDT) on the
order of mK are possible!) This allows for the detector to function, but can render the
InSb FPA useless under high irradiance conditions.

1.1   Background and History

Previous work at AFIT has attributed laser blooming effects in InSb FPA's to the
Burstein-Moss effect.   The contributing dominant effect is from a decrease in the
absorption of the InSb material; the transmitted optical energy then scatters off the read-
out integrated circuitry (ROIC) beneath the InSb thin film back into the optical system.
A focused point source will not extend beyond one or two pixels in a typical FPA
system.(Norman, 2006) Having the high irradiance incident on the detector will cause
blooming effects larger than the diffraction limit on the FPA. This means that it is
possible to have limited or absolute blinding of an imaging system, even though only one
or two pixels are illuminated with high irradiance. This is due to the cascading of the

incident signal across the FPA, caused by optical and electronic phenomena, which leads to the partial or complete blinding of the FPA known as blooming.(Szafranek, 1997)

For typical FPA use, where high irradiances or objects that are a few hundred degrees centigrade are not encountered, blooming is not possible.(Szafranek, 1997) However, when a laser is directed towards the FPA, the high irradiance provided by the focused laser can cause blooming to occur. Once a sufficient number of electrons are excited, the InSb material becomes transparent at the laser's wavelength. This effect is often referred to as the Burstein-Moss shift or absorption-saturation.(Pankove, 1971)

Nurmikko reported that near-absorption-edge wavelengths in InSb can lead to an enhancement of transparency while the InSb is subjected to high irradiances. This is still possible when the crystal is held at cryogenic temperatures, where saturation was observed with less than 1 kW/cm^2 of excitation power. *The carrier lifetime exhibited a sensitive dependence to the equilibrium concentration, energy gap, and temperature. The lifetime can then be varied from microseconds to subnanoseconds by changing these previously stated parameters.(Nurmikko, 1976)* This particular fact is being addressed in this thesis.

Similar work has been reported by Krishnamurthy *et al.* where second-order perturbation theory was used to calculate the Auger and radiative recombination lifetimes. (Krishnamurthy *et al.*, 2007) The carrier lifetime was reported to differ by two orders of magnitude depending on the approximations used to describe the energy bands and wave functions. (Krishnamurthy *et al.*, 1997)

Carrier lifetimes for InSb under high excitation have been reported to be between 80 and 90 nsec.(Norman, 2006) In Norman's work, the rate at which carriers recombined was modeled using a power series expansion where the first three terms dominate.

$$-\frac{dn}{dt} = An + Bn^2 + Cn^3...$$
(1.1)

where An represents recombination from Shockley-Read-Hall processes, Bn^2 represents radiative recombination processes, and Cn^3 accounts for the Auger recombination processes.(Bhattacharya, 1997) Equation (1.1) takes into account three factors that define different process as that contribute to the total carrier lifetime. The overall lifetime of the material is dependent on the density of carriers and cannot be assumed to be an individual value. (An individual value was assumed in the work done by Norman.) In Equation (1.1), the third-order term that is associated to the Auger recombination process becomes dominant with an increase in carrier concentration.(Bhattacharya, 1997) When the sample is illuminated by the laser under high irradiance conditions, the carrier concentration will increase to the point where this third order term is dominant over the others. Noting that the carrier concentration will change with the change in irradiance, it is necessary to model the results with a carrier lifetime that is dependent on the number of carriers, and not assume a single value for a dynamic system as Norman did.

1.2 Problem Description

Current technology cannot produce a detector that is sensitive enough to detect low irradiances and also have the ability to handle high irradiances. The detector saturates at very high irradiances (Figure 1.2-1). A land object may emit an irradiance on a detector

3

system of 10 pW/cm^2, where a laser can easily generate an irradiance of 1 mW/cm^2. (Norman, 2006) It is impossible for current sensor systems to have the capability to distinguish eight orders of magnitude difference without saturating. The FPA can also become ineffective by its automatic gain correction (AGC) algorithm, which alters the contrast ratio of the device in order to distinguish features in the elevated photon flux area. This difference in contrast can cause an inability to distinguish features in the area unaffected by the laser.
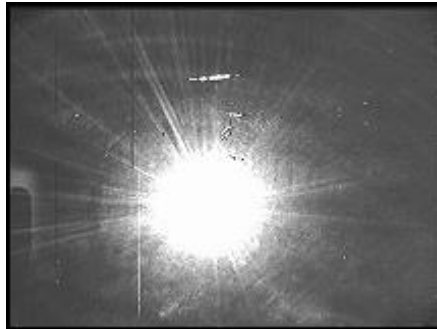
Figure 1.2-1. MWIR sensor that is jammed by a high flux collimated source.(Norman, 2006)

Demonstrations with devices built from commercial-off-the-shelf laser systems have produced jamming that greatly reduced a detector system's ability to track an object.(Ristich, 1996) Having the ability to produce an adverse device, both cheaply and with little effort, poses great challenges.

There are two suggested plausible causes for laser blooming in these detectors, electronic and optical. The first is from a high photon flux incident on the FPA. Large numbers of photons can potentially build up a charge on the sensor; in affect, this potentially would back-bias the p-n junctions in a photovoltaic detector, allowing charge to diffuse laterally through the FPA into neighboring pixels. Once this occurred, the

4

effected areas would be useless for detection purposes. The charge-diffusion effect is limited in the FPA and cannot explain the laser blooming as a whole.(Szafranek, 1997; Wysocki, 2005)

The second source for blooming is a result of optical effects, where optical scatter in the detector system causes the FPA to saturate. To prove this point, Wysocki masked a FPA with a 30-μm pinhole. The mask covered most of the FPA and prevented optical scatter from being incident on it. This also allowed for observation of the carrier diffusion found around the pinhole, where a signal is detected under the mask's edge as shown in Figure 1.2-2.

(a)   (b)
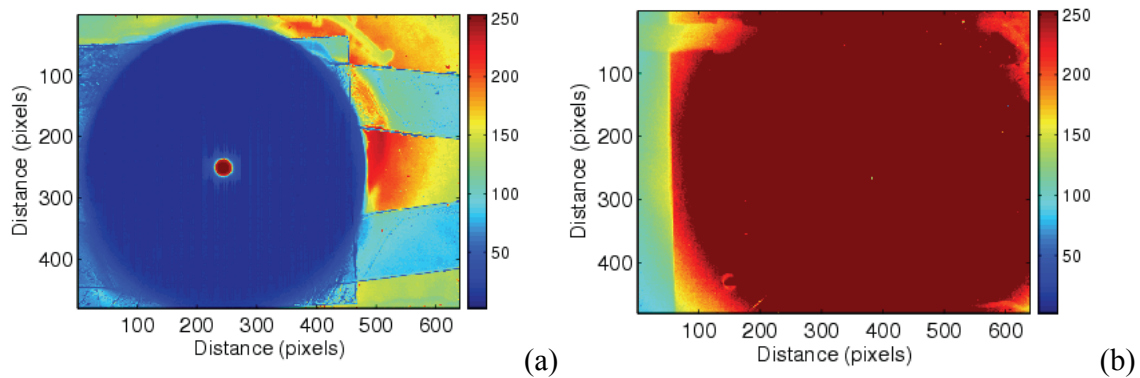
Figure 1.2-2. FPA (a) masked and (b) unmasked with a constant irradiance. Note that (a) is not completely covered by the mask, which is apparent in the top right corner of the figure.(Wysocki, 2005)

The possibility that the FPA system could be rendered useless to its operator poses significant risks that must be mitigated. In order to investigate and determine possible countermeasures for the saturable absorption phenomenon, two samples of bulk n-InSb, 15- and 30-μm thick, were obtained affixed to a silicon substrate for mechanical stability that are typically used to fabricate FPA's. The InSb was tellurium (Te)-doped n-type at 5.0 x 10^{14} cm^{-3}. These samples were investigated through irradiance-dependent laser-absorption experiments and modeled.

5

1.3   Research Objectives

The primary goal of this study is to generate experimental data for the absorption-saturation phenomenon found when InSb is subjected to high irradiances for 5 K to 300 K.   Previous work by Norman only included measurements performed at room temperature (300 K). A model of the semiconductors' absorption process is created that predicts the carrier lifetimes and carrier densities within the bleached InSb samples. The data is modeled with both irradiance and temperature dependence, and a more rigorous carrier lifetime model is used than in Norman's work to account for a carrier lifetime that is both temperature and carrier concentration dependent.

1.4   Preview

Chapter 2 will focus on the theory behind the experiment performed. Basic semiconductor theory is used to guide the reader through the absorption characteristic of semiconductors. Ultimately, this leads to a description of absorption as a function of irradiance on the sample which is thought to be a major source of optical blooming in the system that was used for testing.

Chapter 3 will describe in detail the experimental setup. A brief overview is given in the chapter's introduction, and details are given for each apparatus in the chapter's sections.

Chapter 4 explains the mathematical model used to predict the absorption-saturation in the InSb material under high irradiances.

Chapter 5 addresses the results of the experiments described in Chapter 3. Particular attention is paid to the absorption as a function of irradiance. The results of this test are then compared to the model developed in Chapter 4.

Chapter 6 explains the predicted results from the model, which include the carrier lifetime as a function of carrier density and the carrier densities during blooming.

Chapter 7 will conclude this thesis and provide recommendations for continuing engineering of InSb FPA and operational use, along with suggested future work in this area.

2   Semiconductor Physics

Semiconductor physics is a very broad topic-matter containing many detailed facets that cannot be explained in their entirety within this document. For this reason, only the necessities for understanding crystalline InSb shall be considered. For a more detailed understanding on other areas, refer to an *Introduction to Solid State Physic*s by Charles Kittel and *Solid State and Semiconductor Physics* by John Philip McKelvey. The primary goal of this chapter is to familiarize the reader with the basic concepts to comprehend the absorption-saturation process. Once this process is understood, the experiment and model can be presented.

2.1 Atoms and Orbits

Solids are categorized as being an insulator, a conductor, or a semiconductor based on their ability to conduct electrons. To understand the creation of semiconductor crystals, it is necessary to begin with a single atom. The atom has a nucleus at its core containing protons, neutrons, and several electrons bound to the nucleus in orbits. These orbits are located at discreet energy levels, and each electron in an orbit can only exist at that energy level. The outermost shell or orbit is responsible for the atom's behavior in electrical and chemical interactions. The electron can absorb energy from several different stimuli, such as electromagnetic radiation (photon). When it does, it may gain enough energy to jump to the next highest energy level, which is farther from the nucleus of the atom. The electron cannot exist between orbits (energy levels). The electronic energy levels of the individual atom represent the binding force of the atom's electrons.

The electrons located at the inner core are bound tightly to the atom and have large binding energies. The electrons in the outer shell are not bound as tightly, due to the shielding caused by the inner core electrons of the electrostatic forces from the nucleolus to the valence electrons (classical model). Because electrons are fermions, no two electrons can occupy the same exact energy level; thus, a band of energies is needed to hold all the electrons from a particular atomic orbital when a macroscopic solid is formed (Figure 2.1-1).

Semiconductors are considered to be between an insulator and conductor by their physical properties. An insulator's forbidden energy gap is large, and usually cannot be crossed. A metal is typically understood not to have a forbidden energy gap; instead, the conduction and valence bands overlap (Figure 2.1-2). In a semiconductor, the gap is large enough that the electrons do not normally gain enough energy to jump the forbidden energy gap without an external stimulus providing energy. An example of such stimulus could be a photon from a laser with an energy larger than the forbidden energy gap. This gap is referred to as the energy band gap (E_g) of a semiconductor. Electrons fill the energy levels or orbits around an atom by filling the closest to the nucleus or lowest energy level first. If a semiconductor is held at absolute zero, all of the electrons that would normally be free to move around are frozen in place in their lowest energy levels. The highest energy band filled at absolute zero is considered to be the valence band. It is important to distinguish at this point the difference between the valence band and conduction band. After the band gap, the first energy band (which is empty due to being at absolute zero) higher than the valence band is referred to as the conduction band.
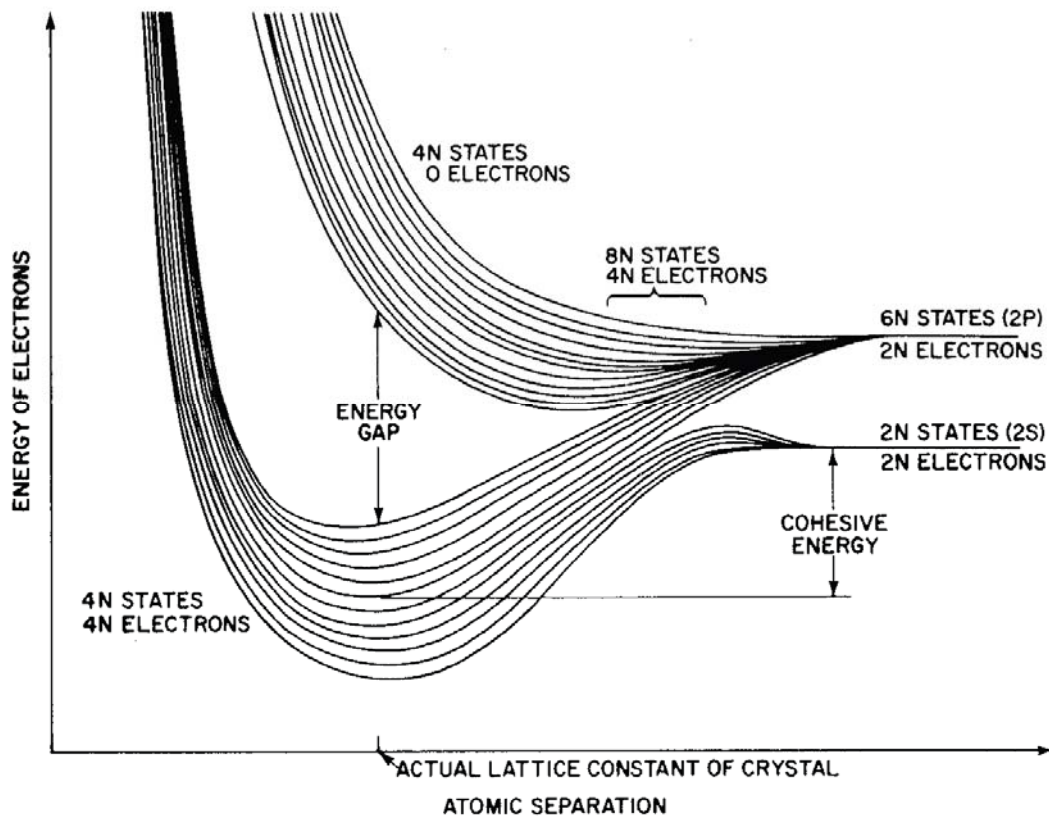
Figure 2.1-1. Banding of energy states as atomic separation decreases.(Pankove, 1971)

Semiconductors are crystalline structures, and InSb has a zincblende structure (Figure 2.1-3) and is a III-V compound semiconductor. These compounds are known as III-V from the grouping found on the periodic table of the elements. A zincblende structure is identical to the diamond structure except that the In is contained on one of the face-centered cubic (FCC) lattices and Sb is contained on the other FCC lattice. An FCC lattice is shown in Figure 2.1-4. In this arrangement, each In atom is tetragonally bonded to four Sb atoms around it and vice versa.

Within the material, many different defects can occur. The most common are point defects that can be formed by a vacancy in the lattice structure, interstitial atoms

which are located in the crystal structure at other than lattice sites, or substitutional atoms that replace the normal lattice atom with an impurity atom. There are many other forms of defects, as well, that can occur which break the crystalline structure and performance of the semiconductor.

Metal

Conduction Band

Valence Band

Semiconductor

Conduction Band

E_g

Valence Band

Insulator

Conduction Band

E_g

Valence Band
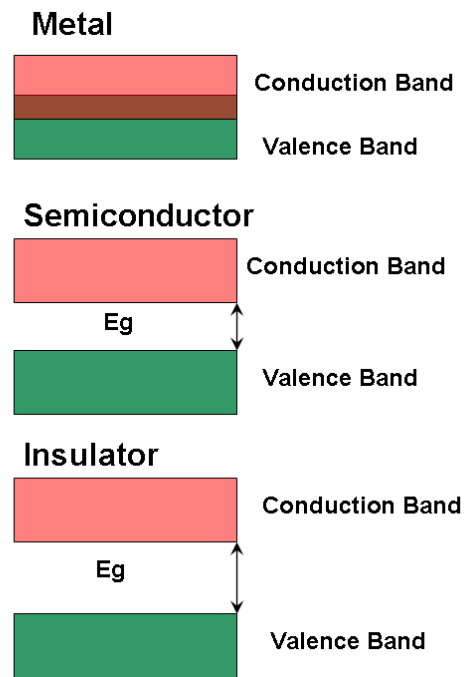
Figure 2.1-2. The energy bands for a metal, semiconductor, and insulator. The forbidden energy gap is represented by E_g.
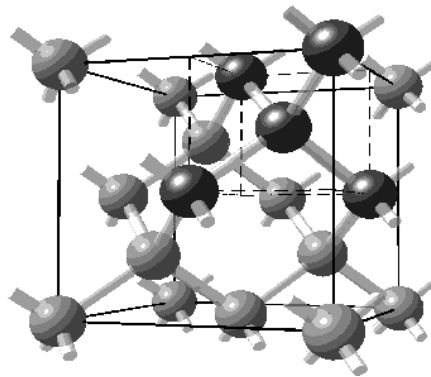
Figure 2.1-3. Zincblende crystal lattice, which contains two FCC crystal lattices.(Kittel, 2003:76)
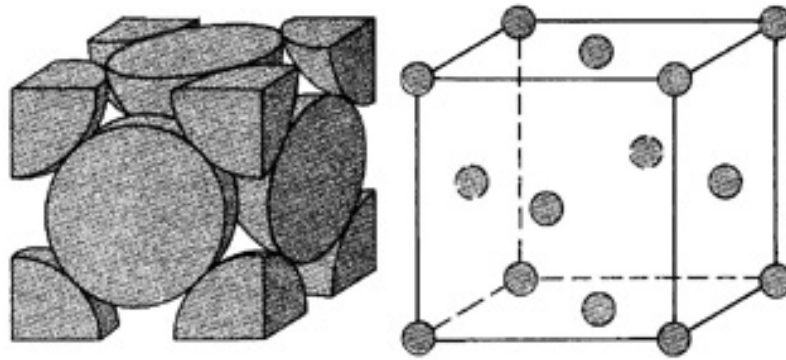
Figure 2.1-4. The face centered cubic crystal lattice structure. On the right is a possible configuration of the electron shells. To the left is the placement of the atoms nucli's.(Farlow, 2004)

2.2 Impurity Atoms

Two different types of semiconductors exist: pure and impure. The pure semiconductor, or intrinsic, contain only the semiconductor material – basic elements with no impurities within the material. Extrinsic semiconductors contain the basic elements with impurity atoms, which act as donors or acceptors of electrons. These semiconductors, in turn, are fabricated from a single element, two, three, or even four different elements combined, besides the possible impurity atoms. Semiconductors that contain one element are referred to as elemental semiconductors and those composed of more than one are considered to be compound semiconductors.

An elemental extrinsic semiconductor can be formed by taking an intrinsic elemental semiconductor and adding in impurity atoms to it through doping. Doping can take place while the crystal is being grown, insitu, or after crystal growth is completed. A dopant can either give or accept electrons. If the dopant atom has one less electron than what is needed to form a complete bond to the crystal lattice into which it is being

introduced, it will create a hole that contributes to the conduction process which is known as an acceptor. A semiconductor which contains acceptor atoms is referred to as a p-type material. The p stands for positive, where the holes are positive charge carriers. On the other hand, there are dopants that have one extra electron after bonding. These types of dopants are called donors because they donate an electron to the conduction process in the crystal which is called n-type. The n stands for negative, where the electrons are negative charge carriers. A flat-band energy diagram of where the donor and acceptor levels are generally located is shown in Figure 2.2-1, where the conduction and valence bands are near the donor and acceptor energy levels, respectively.
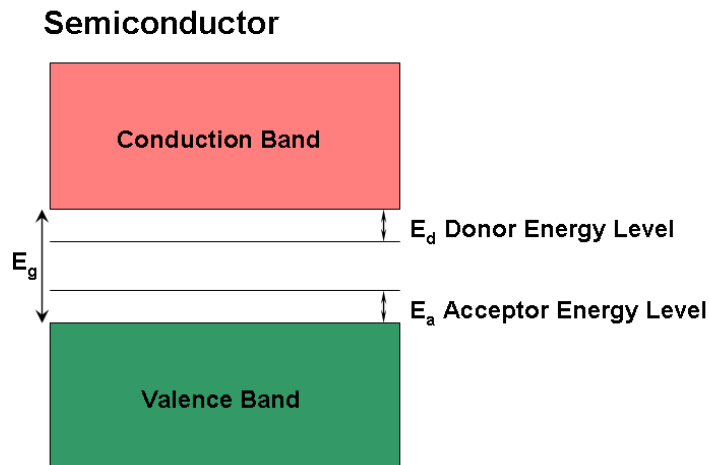
Figure 2.2-1. The valence and conduction bands found in a semiconductor with the donor and acceptor energy levels. Dopant energy levels are measured from the valence band to the acceptor level and from the conduction band to the donor level.

Compound semiconductors such as InSb can also be doped; when the dopant is added, it can sit on either lattice site. Depending on which FCC lattice site the dopant sits will change how it affects the crystal's net charge. An atom from group-II will act as an

acceptor when it is filling the group-III lattice site in the III-V semiconductors. The group-VI atom will act as a donor when it is in place of the group-V atom in the III-V semiconductors. Interestingly, atoms from group-IV can act as donors or acceptors depending on whether they are located on the lattice site of a group-III or group-V atom, respectively. A dopant with this capability is known as an amphoteric impurity. To determine if the material was doped p-type or n-type, it is necessary to take Hall measurements on the fabricated bulk semiconductor. Shown in Figure 2.2-2 are the outer valence electrons which contribute to atomic bonding, where an intrinsic, p-type and n-type semiconductor are all shown. The p-type and n-type figures show where the free electron and hole are located around the donor or acceptor atom after bonding.

Intrinsic   **p-type**   **n-type**
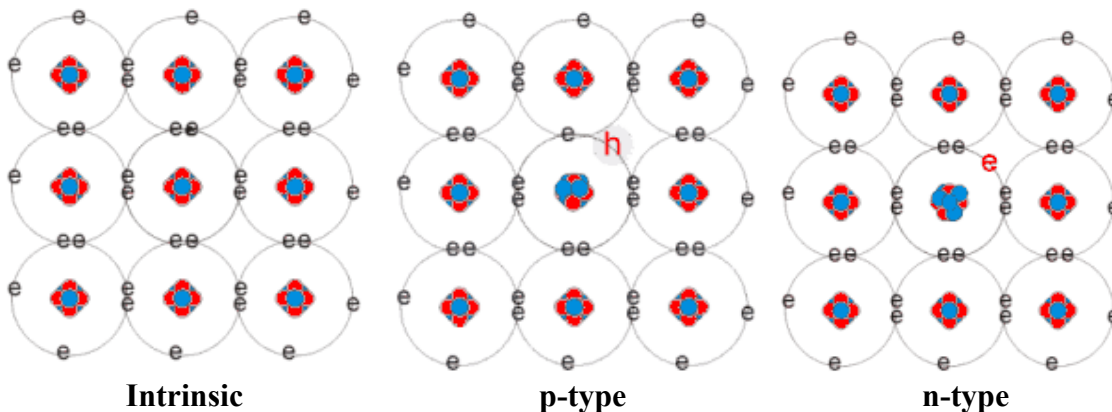
Figure 2.2-2. The valence electron orbit, where bonding of the atoms occurs. Shown left to right, intrinsic, p-type, and n-type semiconductor.(Farlow, 2004)

Now that a general idea of the semiconductor structure is understood, the mathematical representation of the interactions between the valence and conduction bands when the electrons and holes are moving about can be investigated. In this representation of the energy bands, the dopant atoms, once the temperature is above $T = 0$

K, can begin to be thermally ionized, releasing carriers into the bands and conducting electricity. This is because the effective mass is smaller than that of the radius of the orbit. The thermal ionization energy of the carriers can be estimated as

$$k_B T \approx E_d \qquad (2.1)$$

where k_B is Boltzmann's constant, T is the temperature and E_d is the donor energy level.

For a direct band gap semiconductor, when the momentum of the electrons is $\mathbf{K} = 0$, the valence band has a maximum called the Γ point (see section 4.1 for more detail). The conduction band will then also have a minimum point that occurs when the momentum is once again $\mathbf{K} = 0$. An indirect gap semiconductor would have one of the maximum and minimum points shifted so that they were not aligned in k-space. InSb has three valence bands with maxima occurring at $\mathbf{K} = 0$: the light-hole, heavy-hole, and spin-orbit split-off bands. These bands can be considered as parabolic functions in k-space while investigating them close to the band edges. Allowed energies in the conduction band are

$$E = E_g + \frac{\hbar^2 k^2}{2m_e} \qquad (2.2)$$

and in the valence band,

$$E = -\frac{\hbar^2 k^2}{2m_h} \qquad (2.3)$$

where $\hbar$ is Planck's constant divided by 2π, and m_e and m_h are the effective masses of the holes in the valence band and electrons in the conduction band, respectively. The effective masses are derived from the wave-like particle duality behavior of the electrons. Consider a wave packet, and within it, a wave. This packet then contains several

15

frequencies spread across a range, w, where the center frequency is w_o and the entire packet moves with a velocity of

$$v_g = \frac{dw}{dk} = \frac{1}{\hbar}\frac{dE}{dk} \tag{2.4}$$

where E is the energy. When the wave packet moves a distance dx in time dt by the application of an electric field, E_{field}, then the change in energy that the wave packet experiences is

$$dE = -qE_{field}dx \tag{2.5}$$

where q is the charge of an electron. This change in time and distance will have a corresponding change in k-space where dk is the change from k around a central value, k_o, which is

$$dk = \frac{dk}{dE}dE = \frac{1}{\hbar v_g}dE \tag{2.6}$$

which can be expressed as

$$dk\frac{dk}{dt} = \lim_{dt \to 0}\frac{dk}{dt} = \frac{1}{\hbar v_g}\frac{dE}{d} = -qE_{feild}\frac{1}{\hbar v_g}\frac{dx}{dt} \tag{2.7}$$

and $\frac{dx}{dt} = v_g$, which means that $\hbar\frac{dk}{dt} = -qE_{feild}$. In order to find the acceleration, a derivative in time can be taken on the velocity

$$\frac{dv_g}{dt} = \frac{1}{\hbar}\frac{d}{dt}\frac{dE}{dk} = \frac{1}{\hbar}\frac{d}{dk}\frac{dE}{dk}\cdot\frac{dk}{dt} = \frac{1}{\hbar}\frac{d^2E}{dk^2}\frac{dk}{dt} \tag{2.8}$$

and then substituting $\frac{dk}{dt}$ into the acceleration equation gives

$$\frac{dv_g}{dt} = -\frac{1}{\hbar^2}\frac{d^2E}{dk^2}qE_{field}. \tag{2.9}$$

16

Comparing these two solutions gives rise to the effective mass of the electron in the semiconductor as

$$m_e = \frac{\hbar^2}{\left(\dfrac{d^2E}{dk^2}\right)}$$

(2.10)

In order to find the effective mass of a hole, the process is the nearly the same for the derivation of that of the electron. The only difference is that the derivation must allow for one vacancy in a state where the others are completely filled within the valence band. This gives a similar result that can be interpreted as an electron with a positive charge and has a mass of

$$m_h = -\frac{\hbar^2}{\left(\dfrac{d^2E}{dk^2}\right)}$$

(2.11)

The electrons within the semiconductor are described by Fermi-Dirac statistics where the electrons are considered Fermions. These Fermions are described by the Fermi-Dirac distribution function, which gives the probability that an energy level is occupied by Fermions. The Fermions may have a spin up or spin down associated to them, and must follow the Pauli Exclusion Principle from quantum mechanics, where only a single Fermion may occupy a quantum state. This means that when the Fermions are added to an atom at $T = 0$ K, they will fill the available energy levels from the lowest energy to the highest. This follows as stated from the classical view mentioned earlier. When all the electrons from an atom are in a respective energy state, and when the semiconductor is then held at absolute zero, there is no movement of electrons. The highest energy level filled is the Fermi-energy level. The Fermi function thus describes

the probability that at a certain energy level, E, is occupied by an electron. The Fermi function is

$$F(E) = \frac{1}{e^{\frac{E-E_f}{k_B T}} + 1} \tag{2.12}$$

and for holes, is

$$F_h(E) = 1 - F(E) \tag{2.13}$$

where E_f is the Fermi Energy of the semiconductor which is the energy where there would be a 50% chance of finding an electron if all the possible energy levels were allowed.

Interestingly, the distribution function for the donor impurities is different than the Fermi-Dirac distribution function previously mentioned, despite the fact that they are Fermions, as well. This needs to be considered for the n-type InSb. To distinguish between the two, consider that the ionized donor energy level will still have electrons in it with either spin up or down, and the donor energy level cannot be empty at any time. Therefore, there is a factor of ½ added to the PDF for the donor impurities, which is given by

$$F_d(E_d) = \frac{1}{1 + \frac{1}{2} e^{\frac{E_d - E_f}{k_B T}}} \tag{2.14}$$

It may be worth mentioning that the acceptors have a different PDF, as well, but is not needed for the model.

2.3 Density of States

The density of states for either the conduction band or valence band is equal to the density per unit volume and energy of the number of solutions given by Schrodinger's wave equation. In order to derive the density of states, assume that the semiconductor's energy levels are bound within an infinite quantum well where the physical dimensions of the material are given as a cube with a side of length, L. By making this assumption, there is no change to the result because the solution is density of states per unit volume, and solving for any volume from any shape will work. Starting with the solution to the Schrodinger's wave equation given by

$$\Psi = A\sin(k_x x) + B\cos(k_x x) \tag{2.15}$$

where A and B are variables that are solved, k_x is the wave vector and x is the distance. For a realistic solution, the wave function will need to be equal to zero at the quantum well's walls or barriers. When $x = L$, Equation (2.15) must equal zero so that the wave number, k_x, has the solution of

$$k_x = \frac{n\pi}{L}, n = 1, 2, 3... \tag{2.16}$$

where n is the number of nodes in the wave. Solving this again for the y- and z-axis will give the full solution to the cube in momentum space or **k**-space (Figure 2.3-1).

In order to find the complete solution, the volume of 1/8 of a sphere is calculated that has a radius of k which is divided by a volume for a single solution $(\pi/L)^3$ which gives a solution of

$$N = 2\frac{1}{8}\left(\frac{L}{\pi}\right)^3 \frac{4}{3}\pi k^3 \tag{2.17}$$

19

where the factor of two accounts for the Fermions ability to have either spin up or spin down.
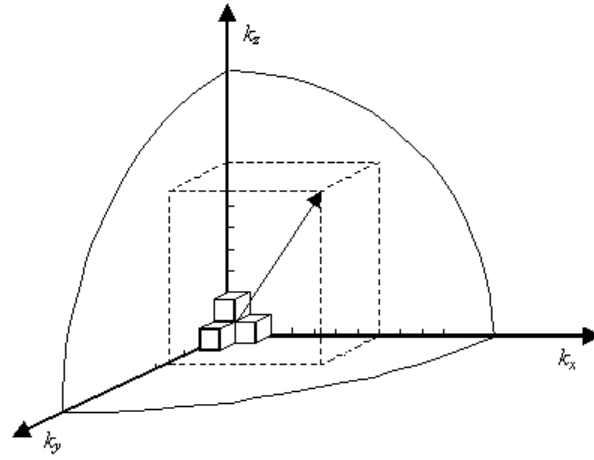
Figure 2.3-1. Momentum space, κ-space, showing the simplified method for finding the density of states within a quantum well assuming it is a cube instead of a sphere.

The density per unit energy is

$$\frac{dN}{dE} = \frac{dN}{dk}\frac{dk}{dE} = \left(\frac{L}{\pi}\right)^3 \pi k^2 \frac{dk}{dE} \tag{2.18}$$

and the wave number is related to the kinetic energy of a particle by

$$E(k) = \frac{\hbar^2 k^2}{2m^*} \tag{2.19}$$

where m^* is the mass of the particle, and providing that

$$\frac{dk}{dE} = \frac{m^*}{\hbar^2 k} \tag{2.20}$$

and

$$k = \frac{\sqrt{2m^* E}}{\hbar}. \tag{2.21}$$

The density of states then is given by

$$g(E) = \frac{1}{L^3}\frac{dN}{dE} = \frac{8\pi\sqrt{2}}{h^3}m^{*3/2}\sqrt{E}\ , \text{ when } E \geq 0 \qquad (2.22)$$

where the function must be zero at the bottom of the well and for negative energies. Following the same type of analysis, the density of states for a semiconductor can be derived, where the effective mass accounts for the periodic potential on the electron. The lowest energy level that an electron can fill in the bottom of the conduction band is E_c and, the density of states in the conduction band then follows as

$$g_c(E) = (2m_c*)^{3/2}\frac{\sqrt{E - E_c}}{2\pi^2\hbar^3} \qquad (2.23)$$

and for the valence band as

$$g_v(E) = (2m_v*)^{3/2}\frac{\sqrt{E_v - E}}{2\pi^2\hbar^3} \qquad (2.24)$$

where E is the energy of the level which is being investigated, and E_c is the bottom of the conduction band taken to be E_g, and E_v is the top of the valence energy level taken to be zero. Knowing the PDF and the density of states for the conduction band, the density of electrons within the band can be found as

$$n_o = \int_{Eg}^{\infty} g_c(E)F(E)dE \qquad (2.25)$$

where the integration takes place from the bottom of the conduction band edge to infinity, allowing for all possible energy levels in the band as they increase in energy. For the valence band holes,

$$p_o = \int_{-\infty}^{0} g_v(E)F_h(E)dE \qquad (2.26)$$

21

where the integration takes place from negative infinity to the top of the valence band allowing for all possible energy levels in the band as they decrease in energy. A graphical representation of how the density of states and the Fermi function combine to give the electron and hole distributions is shown in Figure 2.3-2.
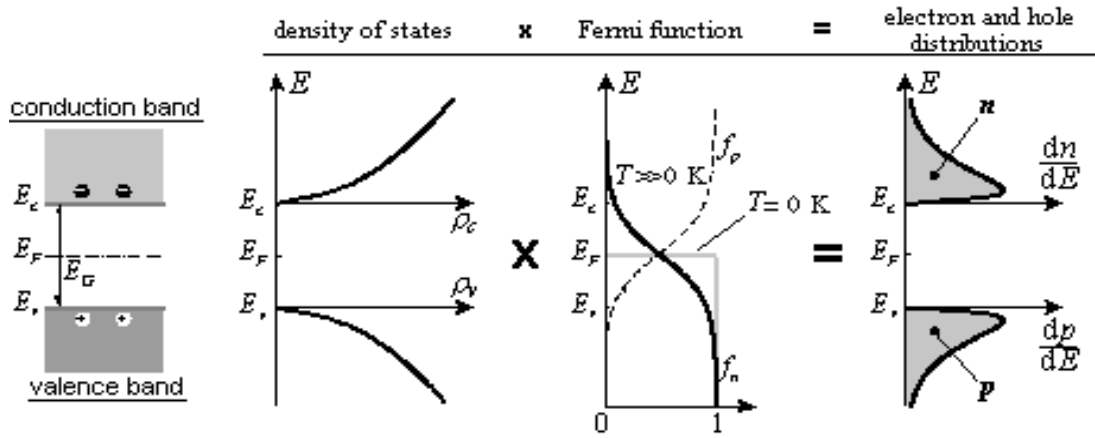
Figure 2.3-2. The distribution of electrons and holes in a semiconductor, where the density of states times the Fermi function equals the differential carrier distribution.(Farlow, 2004)

The number of electrons times the number of holes:

$$n_o p_o = n_i^2 = N_c N_v Exp\left(\frac{-E_g}{2k_B T}\right) \tag{2.27}$$

gives the number of intrinsic carriers within the material squared, known as the mass action law. This relationship can then be used to determine the number of intrinsic carriers for non-degenerate semiconductors as

$$n_i = \sqrt{N_c N_v} Exp\left(\frac{-E_g}{2k_B T}\right) \tag{2.28}$$

where N_c and N_v are

$$N_c = 2 \left(\frac{2 \pi m_c {}^* k_B T}{h^2} \right) \qquad (2.29)$$

$$N_v = 2 \left(\frac{2 \pi m_v {}^* k_B T}{h^2} \right) \qquad (2.30)$$

(Note that Equations (2.29) and (2.30) are derived from the Boltzmann approximation and not Fermi statistics, as such they cannot be used in general.) For degenerate semiconductors, the intrinsic carriers can be found from

$$n_i = \sqrt{n_o p_o} \qquad (2.31)$$

where n_o and p_o are given by Equations (2.25) and (2.26), respectively.

When the sample is doped, such as the n-type InSb, it is necessary to consider the number of ionized donors. When the donor atom's electron becomes ionized, it leaves behind a positively charged donor ion, and the conduction band gains an electron. There are two different types of impurities to consider, shallow and deep impurities. A shallow impurity is one that requires little energy to become ionized, which means that at room temperature, it could be assumed that all of the shallow donors are thermally ionized. There are then also deep level impurities that require a large amount of energy to ionize, and only a fraction of them would be thermally ionized at room temperature. Deep impurities are referred to as traps because they can form recombination centers where holes and electrons are captured and annihilated. Once either type of impurity is ionized, their electrons contribute to the free electrons and begin the conduction process in the semiconductor.

Charge neutrality states that the total number of electrons must equal the total number of holes, meaning there is no net charge in the semiconductor, and is given by

$$n_o + N_a^- = p_o + N_d^+ \tag{2.32}$$

where N_a^- and N_d^+ are the number of ionized acceptors and donors, respectively. The total number of ionized donor sites is given by

$$N_d^+ = N_d \left(1 - F\left(E_g - E_d\right)\right) \tag{2.33}$$

If the semiconductor material is held at a high temperature, the carrier density will be equal to the intrinsic carrier concentration. If the semiconductor is at a low temperature, the carrier density will be dominated by the ionization from the impurity donors (Figure 2.3-3). If a semiconductor does not have many donors in it or is lightly doped, it may suffer from freeze-out at low temperatures. This is when the donor impurities are frozen in place and cannot gain enough energy to be ionized, and cannot contribute to the free electron population. If a semiconductor is heavily doped, it will freeze-out at a lower temperature, or not at all. When the semiconductor does not freeze-out, it is considered to be degenerately doped. This occurs when the donor impurity level is no longer a discrete energy level but forms a band that overlaps the conduction band. The donor energy band is formed from the total number of donor atoms being significantly large so that the atoms' valence electrons begin to form an energy band. Since no two electrons can occupy the same energy level, they spread out into higher allowed energy levels, in the same manner that the crystal lattice atoms did prior to doping (Figure 2.1-1). In this fashion, the donors' electrons are always contributing to the conduction process to 0 K and eliminate the freeze-out effect.
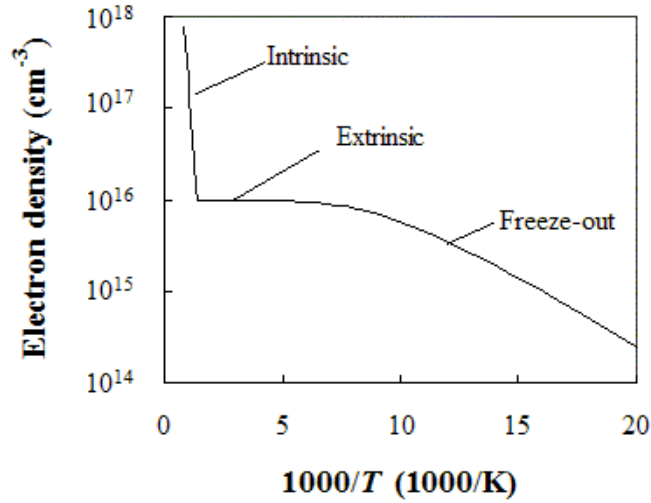
Figure 2.3-3. The carrier density for an n-type semiconductor versus inverse temperature. Labeled are the three areas of differing behavior due to temperature changes of the crystal lattice.

If the semiconductor is given energy from an external source such as a battery, or electromagnetic radiation, it will no longer be in thermal equilibrium. This external energy then will stimulate new free carriers within the semiconductor that were not there at thermal equilibrium and Fermi statistics still hold true. The Fermi energy changes to account for the new carriers in the system. Once the semiconductor is no longer in thermal equilibrium, the Fermi energy level will adjust for the added energy in the system and can now be considered as a quasi-Fermi energy level which is described by the same PDF as the Fermi energy level except that the Fermi energy is now altered to respect that of the non-thermal equilibrium condition. For the valence band, it is given as

$$F_{QV}(E) = \frac{1}{e^{\frac{-E+E_{QFV}}{k_B T}} + 1} \tag{2.34}$$

and for the conduction band,

$$F_{QC}(E) = \frac{1}{e^{\frac{E - E_{QFC}}{k_B T}} + 1}$$ (2.35)

where E_{QFC} and E_{QFV} are the quasi-Fermi energies for the conduction and valence bands, respectively. The number of free carriers that are in the n-type semiconductor when not in equilibrium for the conduction band electrons by

$$\Delta n = \int_{E_g(T)}^{\infty} g_c(E) F_{QC}(E) dE - n_o - N_d^+$$ (2.36)

and for the valence band holes

$$\Delta p = \int_{-\infty}^{0} g_v(E) F_{QV}(E) dE - p_o$$ (2.37)

where the limits of integration incorporate the conduction and valence bands, respectively. The basic understanding of semiconductor physics that are applied to this problem should now be understood enough to progress to absorption of IR radiation.

2.4 Absorption Physics

When a photon is incident on a solid such as a semiconductor, several different processes can take place. The first process to be considered is reflection. The amount of reflection off of the semiconductor is dependent on the wavelength of the photon that is incident on the interface and the material parameters. The interface shall be considered to be between the semiconductor and air. Reflection then can also change based on the incident angle of the incoming photon. If only normally incident photons are considered, the explanation of the process is simplified. The reflection is given by

$$R = \left(\frac{n_a - n_s}{n_a + n_s} \right)^2$$ (2.38)

26

where n_a is the index of refraction of air and n_s is the index of refraction for the semiconductor. The index of refraction for air is known to be one and that of InSb for $\lambda = 4.636$ μm is taken to be 3.9, so that $R = 35$ %.

From this point forth, only those photons that were not reflected at the interface will be considered. Once the incident photons start to pass through the interface, they will be absorbed by several different absorption processes. These processes all depend on the ability of an electron to absorb the photon's energy; both free electrons and bound electrons may absorb photons. These electrons are then found in different states within the material, valence-band electrons, free-carriers that include valence-band holes and conduction-band electrons, and electrons that are bound to the dopant in the material and any other defects.(Moss, 1973:48) Each can contribute to a different absorption process (Figure 2.4-1).

The first of these to be considered is the dominant absorption process that occurs for $\lambda = 4.636$ μm in InSb, band-to-band absorption. In this process, the photon is absorbed by giving its energy to a valence-band electron, which is then excited to the conduction-band, leaving a hole in the valence-band. The photon energy is given by

$$E = \frac{hc}{\lambda} \tag{2.39}$$

where h is Planck's constant, c is the speed of light, and λ is the wavelength of the photon. The absorption edge will occur when the photon's energy equals that of E_g. This then will produce a sharp absorption edge at that wavelength (Figure 2.4-2). The absorption spectrum shown in Figure 2.4-2 is that of a semiconductor and is not specific

to n-InSb. It is known that doping a semiconductor will shift the Fermi-energy level, it also shifts the absorption edge. The shift can be calculated from

$$EF = \frac{\hbar^2}{2m_c^*}\left(3\pi^2 N_d\right)^{2/3}$$ (2.40)

where here, N_d = 5.0 x 10^{14} cm^{-3}, m_c^* = 0.014 m_e, and EF = 1.6 meV.(Ioffe, 2008) At absolute zero, E_g = 0.24 eV, and with the added shift, $E_{g\ shifted}$ = 0.2416 eV. For n-type semiconductors, when the density of states in the conduction band is low enough that a small number of electrons can fill the band to a significant depth, the lowest energy levels in the conduction band are then filled.
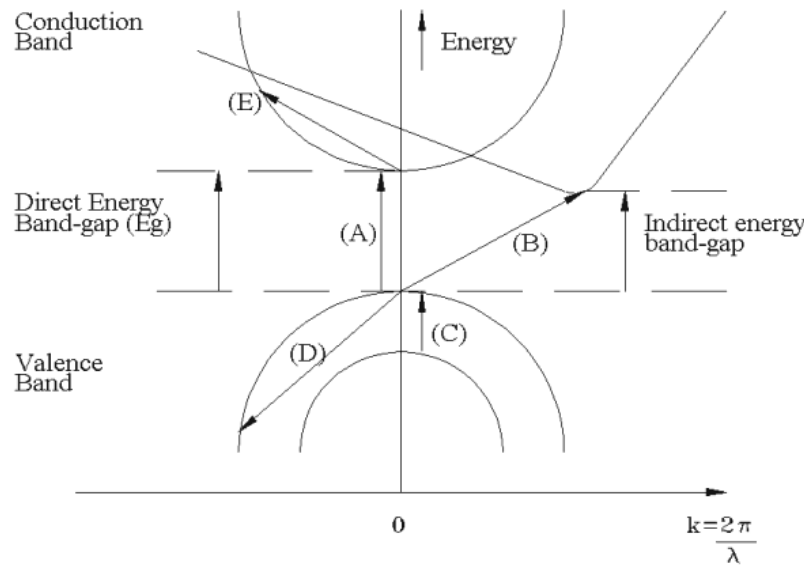
Figure 2.4-1. Parabolic energy band diagram of a semiconductor, showing the different locations of absorption process: (A) Direct valence to conduction band transitions (constant *k* vector), (B) Indirect valence to conduction band transitions aided by photon/phonon coupling interactions, (C) Inter-valence band transitions, (D) Valence band free-carrier transitions aided by impurities or photon/phonon interactions, (E) Conduction band free-carrier transitions aided by impurities or photon/phonon interactions.(Bennett *et al.*, 1990)
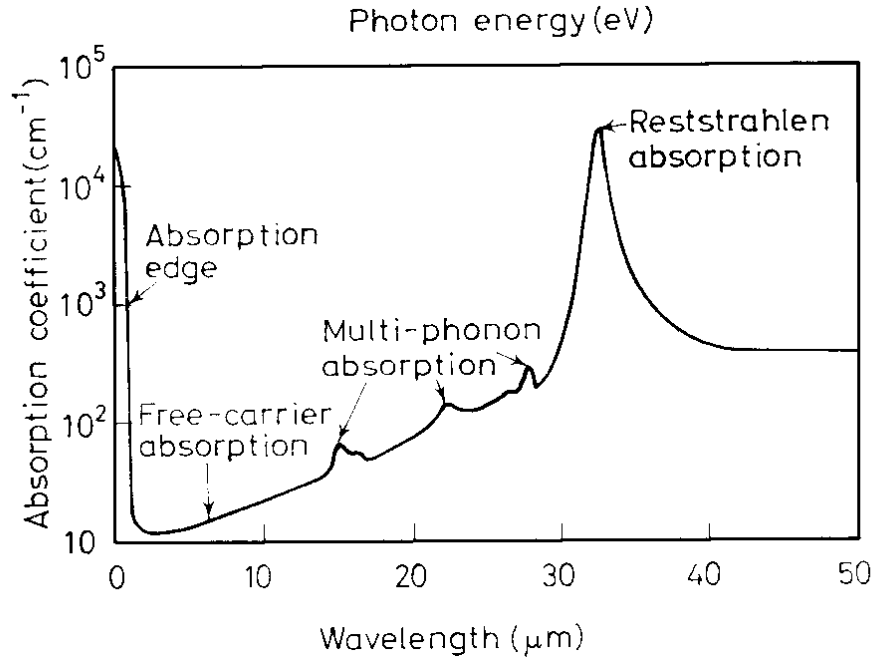
Figure 2.4-2. Absorption band edge verse wavelength.(Moss, 1973:53)

The electrons from the valence band will require an energy that is greater than the bandgap energy to be optically excited into the conduction band. There is then a decrease in the absorption coefficient for energies above the bandgap.(Bennett *et al.*, 1990) For more information on band-to-band absorption, see Pankove.

Another process that can occur is free carrier absorption (FCA). In this process, the photon is absorbed by a free electron or hole. The free carrier is located in one of the bands. When it absorbs the photon, it transitions from one energy level to a higher one within the same band, while conserving momentum.(Li, 2006:252) FCA can be expressed as

$$\alpha_{FCA} = \frac{Nq^2\lambda^2}{m^*8\pi^2 n_2 c^3 \tau}$$

(2.41)

29

where N is the carrier concentration, n_2 is the index of refraction for InSb, c is the speed of light through vacuum, and τ is the carrier lifetime.(Pankove, 1971:75)   At room temperature, where FCA is greater than T = 0 K, $\alpha_{FCA} = 2.9 \times 10^{-14}$ m^{-1}, which will be shown to be significantly less than band-to-band absorption.   For this reason FCA is neglected in this research. The temperature dependent α_{FCA} is shown in Figure 2.4-3.

Two photon absorption (TPA) occurs when phase-coherent photons are absorbed by an electron and excite it by two times the amount in energy of a single photon. For TPA to occur, hv must be less than E_g, which it is not the case in this experiment.(Pankove, 1971:268) Therefore, TPA is also neglected in this work.

In this explanation of saturable absorption, only interband absorption is considered. Saturable absorption can occur in semiconductors when an intense laser pulse that has photon energy, hv, is absorbed by the material and this energy must be larger than the band gap energy, E_g, to be absorbed. The electrons from the valence band are excited to the conduction band, and start to fill up the states at the bottom of the conduction band. Then, the states in the top of the valence band will begin to empty. After a sufficient number of photons have been absorbed, absorption of the photons that have energies close to E_g will stop being absorbed. This occurs because there are no more electrons in the valence band to absorb photons, and the states in the conduction band are full; thus, the photons pass through the material.(Fox, 2001:249)
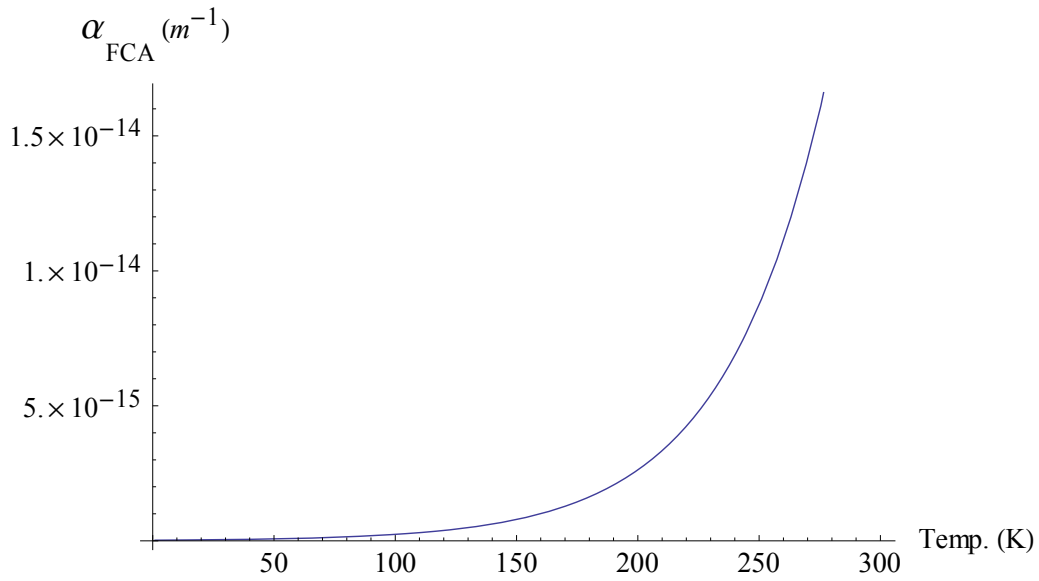
Figure 2.4-3. The temperature dependent free carrier absorption for n-InSb. Note that the absorption present is extremely small.

2.5   Conclusion to Theory

In Chapter 2, the physics of the semiconductor material were discussed for completeness. The main points covered were the interactions of the electrons from the conduction band and valence band during the absorption process of photons. These basic concepts and assumptions are used in the mathematical model (Chapter 4). Having the familiarity of the interactions that take place during absorption in the InSb material leads to the development and implementation of the experiment (Chapter 3).

3   Experimental Apparatus

The saturable-absorption process was studied experimentally by creating an ideal situation for the InSb material to bleach. Having already understood the physics behind this process, a detailed discussion of the experimental apparatus can be entertained. The experiment will be described by following Figure 3.2-1 and the corresponding numbered elements. Each critical element of the experiment will then be explained in detail in the chapter's sections.

3.1   Overview of Experiment

A Coherent DEOS Laser (1) was used for the excitation photon energy and was controlled by a separate remote (2), both of which were cooled by a Neslab CFT-75 chiller. A Coherent FieldMax-TO power meter (9), working with a thermal detector PowerMax PM30(10), measured the laser output power. The DEOS laser's beam first passed through a Lasnix attenuator (4) with variable attenuation by means of five metal membranes (mesh screens). After passing through the attenuator, the beam passed through a beam splitter (6), whose second function allowed for a helium neon (HeNe) laser (5) to be coupled onto the DEOS laser's path. Directly opposite of the HeNe laser was the first InSb detector (8). This unit monitored the DEOS laser output power as it fluctuated over time. Between the InSb detector (8) and the beam splitter was a variable neutral density filter (7) that prevented damage to the detector. After the beam splitter, two irises (11) and (16) were placed for co-alignment of the HeNe and DEOS lasers.

Next was the first zinc selenide (ZnSe) lens, with focal length, $F = 20$ mm and diameter, $dia = 50$ mm(12). Then, a second ZnSe lens with $F = 100$ mm and $dia = 50$ mm (13) was placed a distance of 102 mm away from the first lens; placing the two optics (12,13) in these positions formed a beam expander. Following the beam expander was a ZnSe lens with $F = 76$ mm and $dia = 50$ cm (14), which acted as the focusing optic for the experiment; the sample traversed this focal point. The Advanced Research Systems Inc. LT-3-110 open-cycle Helitran (cryostat) sample chamber (15) was then traversed by an automated Zaber linear translation stage T-LSR 150a, which moved the unit through the z-axis of the experiment through the focal point. A ZnSe collecting optic with $F = 100$ mm and $dia = 50$ cm (17) was placed two times its focal length from the focal point of lens (14), and also two times its focal length from the second InSb detector (18). This allowed all of the transmitted photons from the sample to be collected onto the InSb detector (18). The InSb detectors were powered by two HP direct current power supplies E3611A (22) and were managed by a LeCroy Wavepro 7300 Oscilloscope (O-scope) (21). A Laptop running LabVIEW 8.5 (19) communicated with the cryostat, LakeShore Cryogenics 331 Temperature Controller (23), translation stage (under the cryostat), and the router (20), which then communicated with the O-scope (21). An Alcatel vacuum pump (25) maintained 15 mtorr pressure in the cryostat. Liquid helium was then held in a 60-liter dewar (26) with a continuous flow siphon tube to the cryostat, and positive pressure was maintained in the dewar with compressed helium(27).

3.2 Coherent DEOS Laser

During the experiment, a Coherent MID-IR-2 RF-Excited Frequency-Doubled Pulsed CO^2 WaveGuide Laser of $\lambda = 4.636$ μm, peak power of 2.3 watts, and operated at 10.947 KHz, was used. Each laser pulse has a length of 91.285 ns, and repetition time of 683 ns, giving the InSb detector's signal adequate time to decay. The time delay between pulses will be discussed with the explanation of the InSb detectors in Section 3.11.
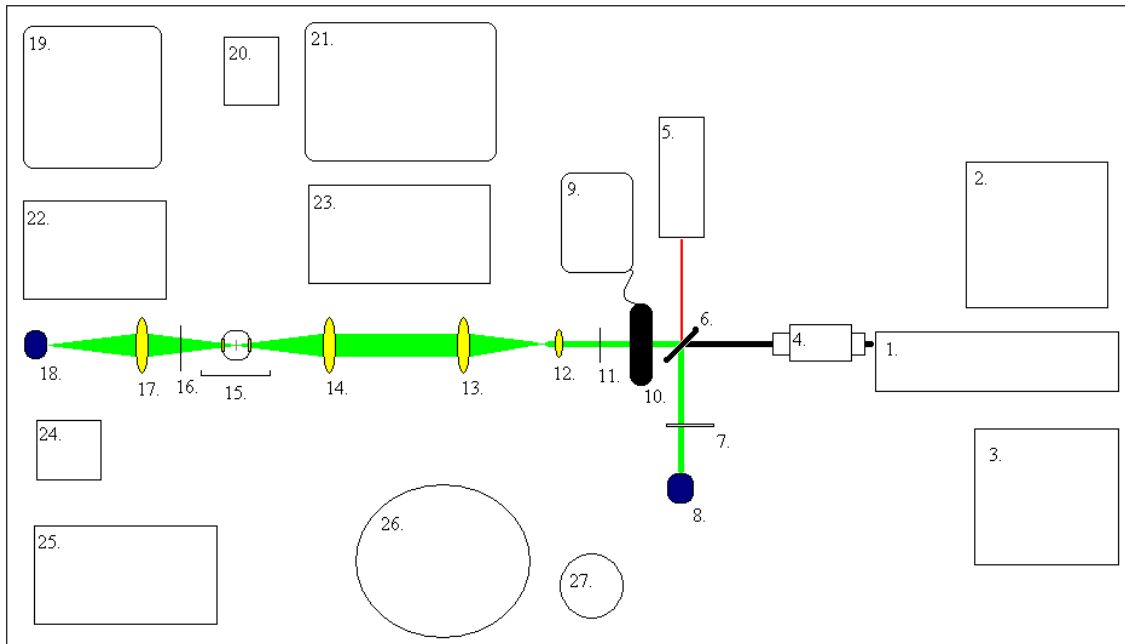
Figure 3.2-1. Top down view of the absorption-saturation experiment. The major parts of the experiment are: 1. Coherent DEOS laser 2. DEOS laser controls 3. DEOS laser cooling unit 4. Lasnix attenuator 5. HeNe laser 6. IR beam splitter 7. Neutral density filter 8. InSb detector 9. Power meter 10. Power meter thermal head 11. Co-alignment iris 12. ZnSe optic 13. ZnSe optic 14. ZnSe optic 15. Helitran cryostat and motorized stage 16. Co-alignment iris 17. ZnSe optic 18. InSb detector 19. LabVIEW 8.5 installed in laptop 20. Ethernet hub 21. Oscilloscope 22. InSb power supplies 23. Cryostat PID temperature controller 24. Cryostat vacuum gauge 25. Cryostat vacuum pump 26. Liquid helium dewar 27. Compressed helium cylinder.

34

The laser was cooled with liquid Dow Frost coolant. This helped to maintain thermal stability of the laser cavity, as well as prevent overheating to the laser and subsequent damage. During the experiment, the laser output power was tracked with the use of an InSb detector that was cooled to liquid nitrogen temperature in order to follow irregularities during the long data collection process. It was found that the laser output power oscillates in a sinusoidal fashion during the data collection, as shown in

Figure 3.2-2. This occurrence represents a 6.5-hour period, where the error reaches no more than 10% from the measured output laser power. Then, note that the laser output power varies again by each data point collected within 30 seconds by 2.72%. These values have been collected to justify a component of the error from the model that assumes a steady state laser output power to the experiment.
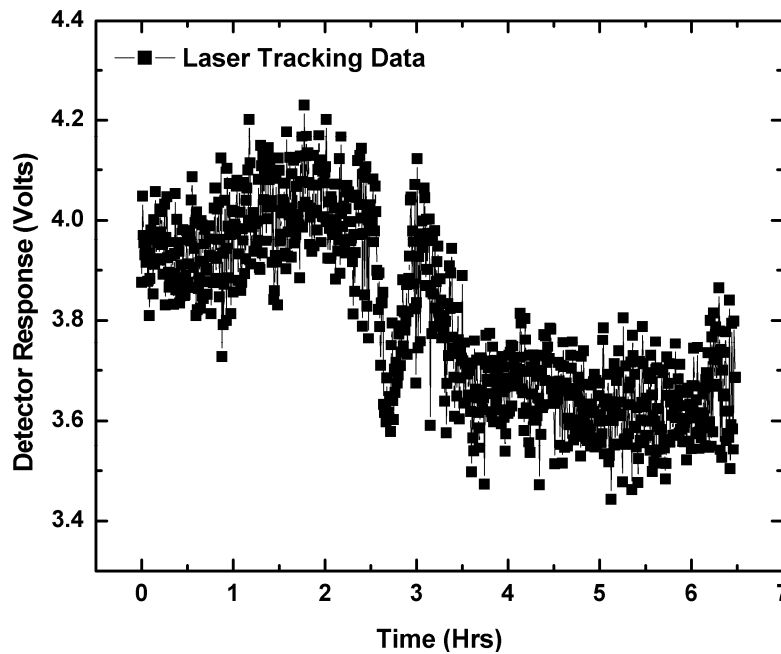
Figure 3.2-2. The DEOS laser output power expressed as a voltage response given by an InSb detector versus time.

3.3 HeNe Laser

A class-2 Helium Neon (HeNe) laser with output power of 1.5 mW and $\lambda = 633$ nm was co-aligned with the DEOS laser so that the two beams followed the same vector down the z-axis of the experiment. The co-alignment was done using the two irises (11) and (16) closed down to *dia* = 1 mm, and propagating both lasers through them. After the alignment was complete, the irises were opened to prevent them from acting as

apertures in the optical system. The HeNe was used in the experiment for several reasons; the first concerns the alignment of the experiment. The HeNe was not used to focus any of the optics, only to aid the placement of the optics and InSb detectors so that the exact centers of the apertures were utilized. Finding the centers of the apertures is critical in order to limit aberrations. In this fashion, photon emission through the experiment was optimized.

The reason the HeNe was not used for focusing the optics was that the wavelength of the DEOS and that of the HeNe are $\lambda = 4636$ nm and $\lambda = 633$ nm, respectively, nearly one order of magnitude different. From Snell's law, $n_1 \sin \theta_1 = n_2 \sin \theta_2$, where n_1 is the index of refraction of air, θ_1 is the angle of the incident ray, n_2 is the index of refraction of the optic, and θ_2 is the angle of the refracted ray. Given that $n_{1air} = 1$, $n_{2HeNe} = 2.58643$ for $\lambda = 633$ nm, and $n_{2DEOS} = 2.4309$ for $\lambda = 4.636$ µm (Luxpop, 2008), it can be determined that the light from the HeNe will travel slower through the lens than the light from the DEOS. This, in turn, will result in the HeNe focused closer to the lens than the DEOS beam. This would cause the cone of rays leaving the focusing optic for the DEOS to converge farther out than the HeNe's focused spot. If the HeNe was visually focused,

then the DEOS would not be in focus, which would cause the power per unit area of the DEOS spot to be limited. This would make it more difficult to bleach the sample.

The HeNe was also utilized in order to maintain a point for studying the sample while traversing in the cryostat. The sample was studied over a one week period. From one day to the next, it was possible that the vacuum pump or liquid helium dewar had been bumped, possibly shifting the sample. Though these events did not occur, it was noted that at the beginning of each day, the HeNe was still at same spot on the sample as

it was the previous day. This spot was also maintained as the sample traversed along the z-axis of the translation stage. The HeNe was turned off during data collection to prevent contamination of the data from absorption of the HeNe photons in the InSb samples. The main concern for maintaining a single spot on the sample was to insure that the data was consistent from one day to the next. This allowed that no minor deviation in sample's geometry or doping profile would need to be considered during analysis.

3.4 Lasnix Attenuator

A Lasnix infrared attenuator model 102 was used directly after the DEOS laser in order to manage the laser output power. In basic principle, the attenuator operates by diffraction. The laser was passed through very fine metal membranes within the attenuator. Attenuation was achieved instantly once the laser passed through the first membrane. For higher levels of attenuation, another membrane was placed in the laser's path, each additional element creates an additive effect in decibels. The laser's output power was then calibrated with several different configurations of membrane placements

in and out of the beam path, and laser output power measurements were performed. When all of the mesh screens were in the beam path, the laser output was attenuated from 2 W to 6 mW. By doing this, a desired output laser power could be set instantaneously without changing the laser timing controls and ultimately disrupting the laser's stability during the experiment.

3.5 Optics

To insure accurate absorption measurements were collected, the photons from the laser needed to pass through the experimental system with as little loss as possible. In a normal non-cleanroom laboratory, there are hundreds of thousands of dust particles per cubic meter. Some dust will deposit on the optics that are not visible to the unaided eye. To control this contamination, the optics in the system were cleaned before the 15- and 30-μm samples' data were collected. While the experiment was not in operation, the optical elements were covered with protective plastic. The optics were not repetitively cleaned, because over-cleaning of any coated optic will drastically shorten the life span of that optic's coating. In general, optical coatings are usually twice as expensive as the optic. Cleaning was performed using methanol, a hemostat, and lens paper.

The optics of the experiment were all constructed of ZnSe with an anti-reflective (AR) coating at 4.6 μm. ZnSe transmits very well from 0.6 μm in the visible to 15 μm in the infrared (Figure 3.5-1).

An AR-coated lens allowed a higher percentage of the incident photons at a desired wavelength to be transmitted, as opposed to being reflected. It should be noted that both interfaces were coated because reflection will take place at the interface where

the photons entered, as well as the interface where the photons exited. The percent

transmittance of the optics was measured using a Corey spectrometer. The material was

then interrogated from 2 to 3.4 μm (Figure 3.5-2).
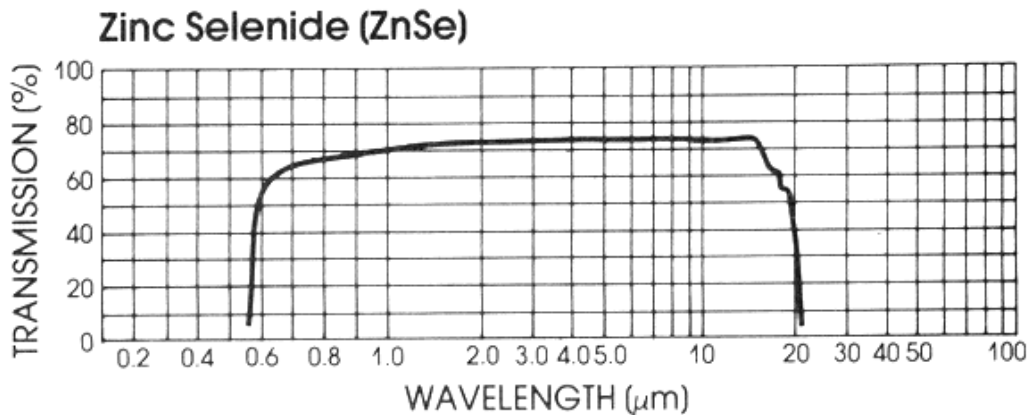
Figure 3.5-1. The transmission spectrum of ZnSe (without AR coating), shown as percent transmission versus wavelength.(Del Mar Ventures 2006)

This range did not cover the actual wavelength used in the experiment, but it did allow

for a comparison to that of the manufacturer of the lenses. The optical elements were

interrogated with the Corey by a linear progression in focal length of the element. First, a

ZnSe window was studied which has the highest transmittance of all the elements, and

second, a slow lens was studied, *etc*. The lenses were studied in this fashion because the

spectrometer that was used did not have the capability to dynamically change its focus on

the lenses. Therefore, when a lens was placed into the Corey spectrometer, it caused a

certain amount of loss during the measurement due to the defocus it created. These

values were then compared to data that was provided by the manufacturer and subsequent

transmission values were deduced for each lens. This limited how much laser power was

reaching the sample. When the laser power was measured, it was done before the optics

and not where the sample was located due to spatial confinement. This meant that the recorded laser output power was actually higher than that which reaches the sample. To correct for this possible large error, a calibration was performed. The experimental data and model have been corrected to reflect for the calibration. These values are then reported with negligible error. The data will be discussed in Chapters 5 and 6.
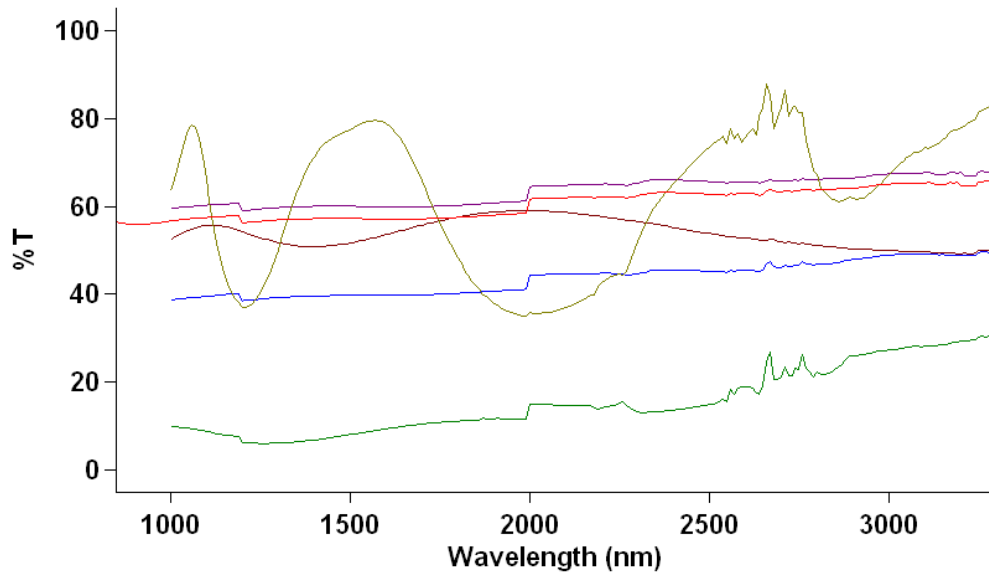
Figure 3.5-2. **Transmission spectrum of the experimental optics in percent transmission versus wavelength (nm). Each element from the top down on the right hand side: (brown) ZnSe cryostat windows, (purple) ZnSe f =75 mm lens, (red) ZnSe f = 82 mm lens, (blue) ZnSe f = 100 mm lens, (green) CF2 beam splitter 2-8 μm.**

Each lens was then centered into the experiment with the convex side facing the laser, using the HeNe laser for a rough estimate in position, and then an IR camera was used in order to fine tune the focus of each lens. The convex portion of the lens was directed toward the laser beam in order to limit aberrations. In an ideal situation, there

would be no aberrations present in the experiment. However, the optics used were not perfect. Thus, by careful alignment, aberrations were limited to a negligible amount.

3.6   Focal Spot

The focal spot was measured using a knife-edge technique where a pinhole of 20 μm was manually translated through the spot.   The laser output intensity profile is normally considered to be Gaussian in nature (Figure 3.6-1).   This data was then plotted in Origin 6.5, and fit to a Gaussian curve as shown in Figure 3.6-2.   The equation used to fit the peak was provided by Origin as

$$y(x) = y_o + \frac{A}{w\sqrt{\frac{x}{2}}}\, e^{-\frac{2(x-x_o)^2}{w^2}}$$

(3.1)

where the full width at half max (FWHM) is w, the area under the fitted Gaussian curve is A, the center of the Gaussian peak is x, and the baseline offset is y_o.   These values were recorded from Origin and plotted into Mathematica using Equation (3.1).   Mathematica allows the curve to be investigated and measured for a standard spot size at $\frac{1}{e^2}$ where e is a known mathematical constant.   The focal spot of the laser was found to be 47.92 μm after the pinhole was deconvolved from the measurement.   A similar measurement was taken for the laser beam at the laser output coupler.   In this measurement, a knife edge was used and manually translated through the beam's path in increments of 2 μm.   After each increment, a power measurement was taken of the beam.   This data was then plotted and fitted as mentioned previously for the focal spot.   This measurement generated a

41

value of 1.83 mm in diameter for the DEOS laser beam at the output coupler; this value

matches that of the laser's data sheet from Coherent with respect to the beam waist.
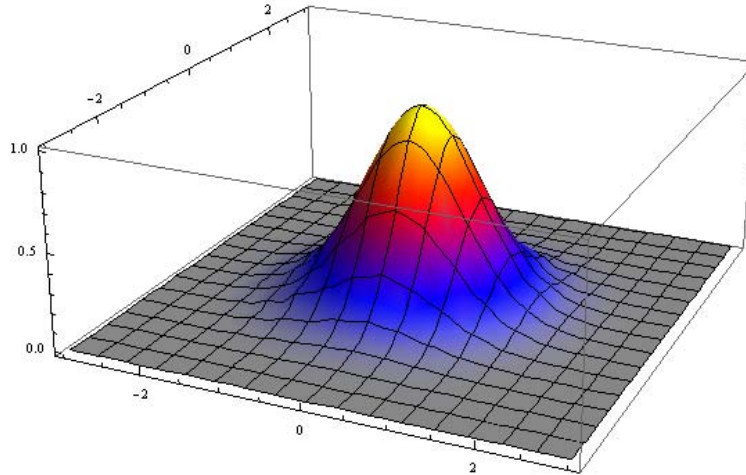
Figure 3.6-1. The Gaussian distribution function representing a laser's irradiance profile when striking an object.
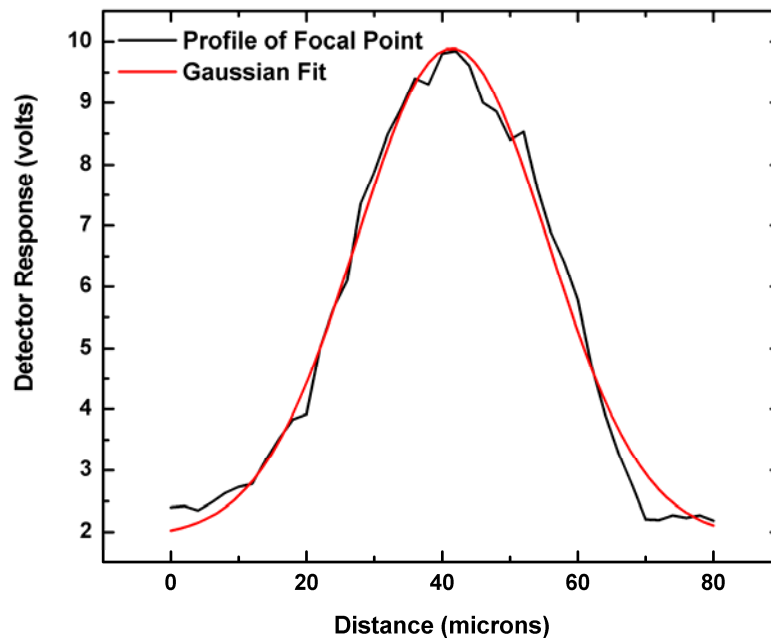
Figure 3.6-2. The Gaussian profile of the beam waist of the focal spot of the laser, 47.9239 μm, where the sample was translated through as a function of the detector's response in intensity and the spot's width in microns.

Knowing the beam waist allows for the experiment to be modeled with geometric optical computations. Starting with the beam expander, it is known that the magnification is given by

$$m = \frac{f_2}{f_1} \tag{3.2}$$

where f_2 = 100 mm is the focal length of the second lens, and f_1 = 20 mm is the first lens of the beam expander, which gives m = 5. This only works if the two lenses are placed such that both of their focal points meet. After the beam passed through the beam expander, it was collimated and has a *dia* = 9.17 mm. The beam entered the focusing optic where the beam waist is given by

$$w(z) = \sqrt{\lambda \frac{\left(1 - \frac{z}{f_3}\right)^2 + \left(\frac{z}{\frac{\pi(b/2)^2}{\lambda}}\right)^2}{\frac{\pi}{\frac{\pi(b/2)^2}{\lambda}}}} \tag{3.3}$$

where z is a position on the z-axis, f_3 = 75 mm is the focal length of the focusing optic, and b is the expanded beam 9.17 mm. Equation (3.3) was then plotted for both a positive and a negative value of w as shown in Figure 3.6-3; the z-axis is across the bottom of the plot and represents the direction in which the sample traversed. The focal spot was then calculated to be 48.26 μm; this value is only 0.71% error from the measured value.
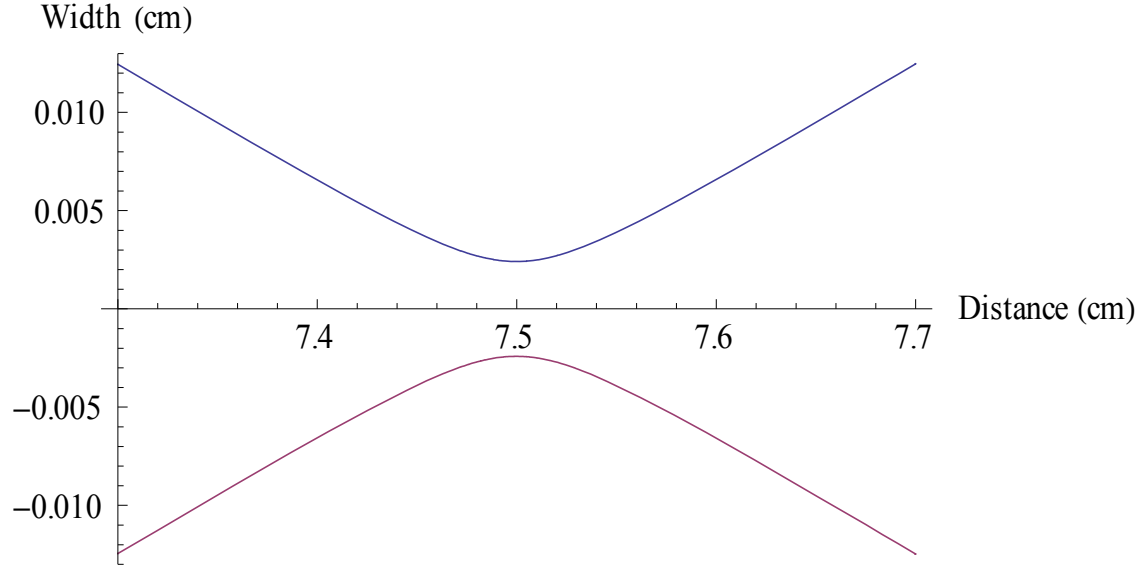
Figure 3.6-3. The modeled focal point as seen from the x-axis, where the z-axis is represented as a distance from 73 mm to 78 mm. At 75 mm is the focal point of the focusing optic where the focal spot had a diameter of 48.26µm.

The irradiance, having units of joules per second-centimeter squared, can be deduced from the above calculations for each position in *z,* as well as each excitation laser power. The area of the beam as a function of *z* was calculated from

$$a(z) = \pi \left(w(z) \right)^2 \tag{3.4}$$

where *w(z)* is the beam waist given by Equation (3.3). The average irradiance is given by

$$Ep(z) = \frac{P}{a(z)} \tag{3.5}$$

where *P* is the laser output power as measured by the power meter. The irradiance as a function of position in the z-axis (Figure 3.6-4) gives a vivid example of the laser irradiance achieved. Translation through a focused laser point to increase and decrease the irradiance on the sample, while translating it through the focal point, is known as a z-

scan. The maximum irradiance found at the focal point (Figure 3.6-4) should be noted to be extraordinarily large compared to an irradiance of just the incident beam when not focused onto the sample (Table 3.6-1).
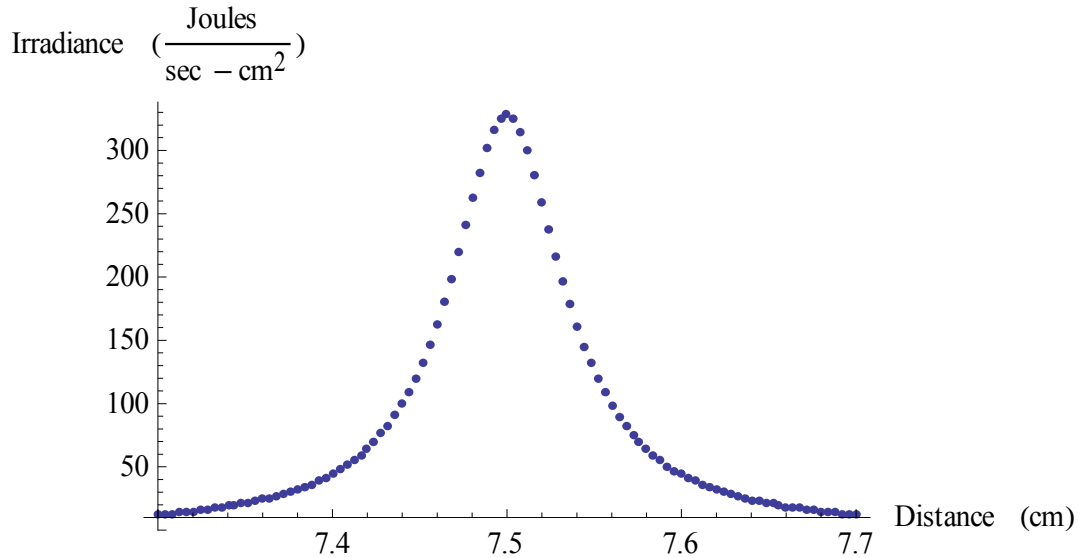
Figure 3.6-4. The irradiance of the focused laser output as a function of distance in the z-axis, where 7.5 cm is the focal point and having a maximum value and laser output power set to 6 mW.

Table 3.6-1. The laser output power and corresponding maximum irradiance found at the focal point. Noting the enormous amount of irradiance generated by a small amount of laser power when focused from when not being focused. Photon irradiance is also calculated for comparison.

DEOS Laser Output Power	Irradiance Focused $\frac{J}{s-cm^2}$	Photon Irradiance Focused $\frac{Photons}{s-cm^2}$	Irradiance Not Focused $\frac{J}{s-cm^2}$	Photon Irradiance Not Focused $\frac{Photons}{s-cm^2}$
6 mW	328	7.65×10^{21}	0.06	1.32×10^{18}
15.8 mW	864	2.01×10^{22}	0.15	3.48×10^{18}
20 mW	1.09×10^3	2.55×10^{22}	0.19	4.41×10^{18}
107 mW	5.84×10^3	1.36×10^{23}	1.01	2.36×10^{19}

.

3.7 Translation Stage

In order to take reliable and repeatable data consecutively, a Zaber motorized linear stage was used (Figure 3.7-1). The stage allowed for travel along the z-axis of the experiment. The cryostat was not directly mounted to the stage due to the numerous lines that go in and out of the cryostat, which produce a significant amount of drag. Instead, a three legged tower was constructed on the moving platform of the stage and pushed the cryostat. The mounting of the cryostat can be found in Section 3.9. Parameters for acceleration, velocity, and distance of travel were then programmed into the attached digital control circuitry and executed by the virtual instrument that was programmed with LabVIEW 8.5. The stage has a resolution of 0.049609 μm and a repeatability of 2.5 μm.(Zaber, 2008) Over the full 4.5-cm data collection range, step sizes of 400 microsteps and 800 microsteps were used for the 15-and 30-μm samples, respectively. A microstep was programmed into the linear stage as being equal to 2 μm. The error introduced from the stage was negligible due to the high fidelity of the instrument. The linear stage was centered under the cryostat at the halfway point of translation and, therefore, creates the need for a known starting position. For the starting position, the cryostat was moved 2 cm toward the drive motor from the center of the stage's translation, so that a total of 4 cm was traversed, 2 cm in front of the focal point and 2 beyond the focal point.

Figure 3.7-1. The Zaber motorized linear stage, T-LSR 150a, was used to translate the sample chamber through the z-axis of the experiment.

3.8 Sample Preparation

Prior to mounting the InSb samples, each was cleaned with acetone, followed by methanol, and then dried with compressed helium. Acetone was flushed over the sample and was used as a solvent in order to remove any deposited organic materials that may have been adhered to the surface. Its high evaporation rate, however, required a subsequent cleaning step in order to avoid striations on the sample. While the sample was still wet with acetone, methanol was flushed over the sample, and was used to remove any residue or particulates. Compressed helium was then used to dry the samples while they were still wet with methanol. This was done to prevent H_2O spots from forming due to the methanol, which absorbs water. Having water spots on the samples would distort the data. The samples were mounted using rubber cement, which will be discussed at the end of Section 3.9.

3.9 Cryostat

The Helitran Open Cycle Cryostat for Optical Spectroscopy (Figure 3.9-1) was used in order to vary the temperature of the sample, and will simply be called the cryostat

from this point forth. The cryostat was mounted on an x-y-z translation stage which was hung above the Zaber translation stage. This robust stage allowed for positioning of the cryostat in the optical path and provided a means to maintain the precise translation of the z-axis. The z-axis of the stage was left free with no stops, to allow the Zaber stage the ability to move the cryostat.

The windows of the cryostat were fabricated from ZnSe and were AR coated for 4.6 μm. The Cryostat controlled the sample temperature, using liquid helium, an internal heater, and a gas flow needle valve. The range in temperature was varied from 4 K to 300 K. The exact settings for a desired temperature are programmed into a proportional-integral-derivative controller (PID controller). The controller compares a measured value from a process with a reference set point value. The difference was processed to calculate a new value for a manipulated process output that brings the process measured value back to its desired set point. Unlike simpler control algorithms, the PID controller can adjust process outputs based on the history and rate of change of the error signal, which gives a more accurate and stable control of the temperature. This allowed the sample to be held at a desired temperature despite irregularities in the liquid helium supply.

The liquid helium was fed through a siphon tube, into the cryostat, and into the cold finger. The sample mount was screwed directly into the cold finger and indium gaskets were used to ensure excellent thermal conduction. A thermistor was attached to the bottom of the sample mount and another was attached to the cold finger. These two thermistors were tested for any divergences from one another by dipping them both into liquid nitrogen and noting that their temperatures were both 77.5 K. This allows the

48

temperature to be recorded above the sample and below the sample; therefore, the sample's temperature can be deduced. When the two thermistors are in agreement, it can be assumed that the sample, if properly bonded to the mount with rubber cement, is also at that temperature for a given range where rubber cement is an effective thermal conductor.
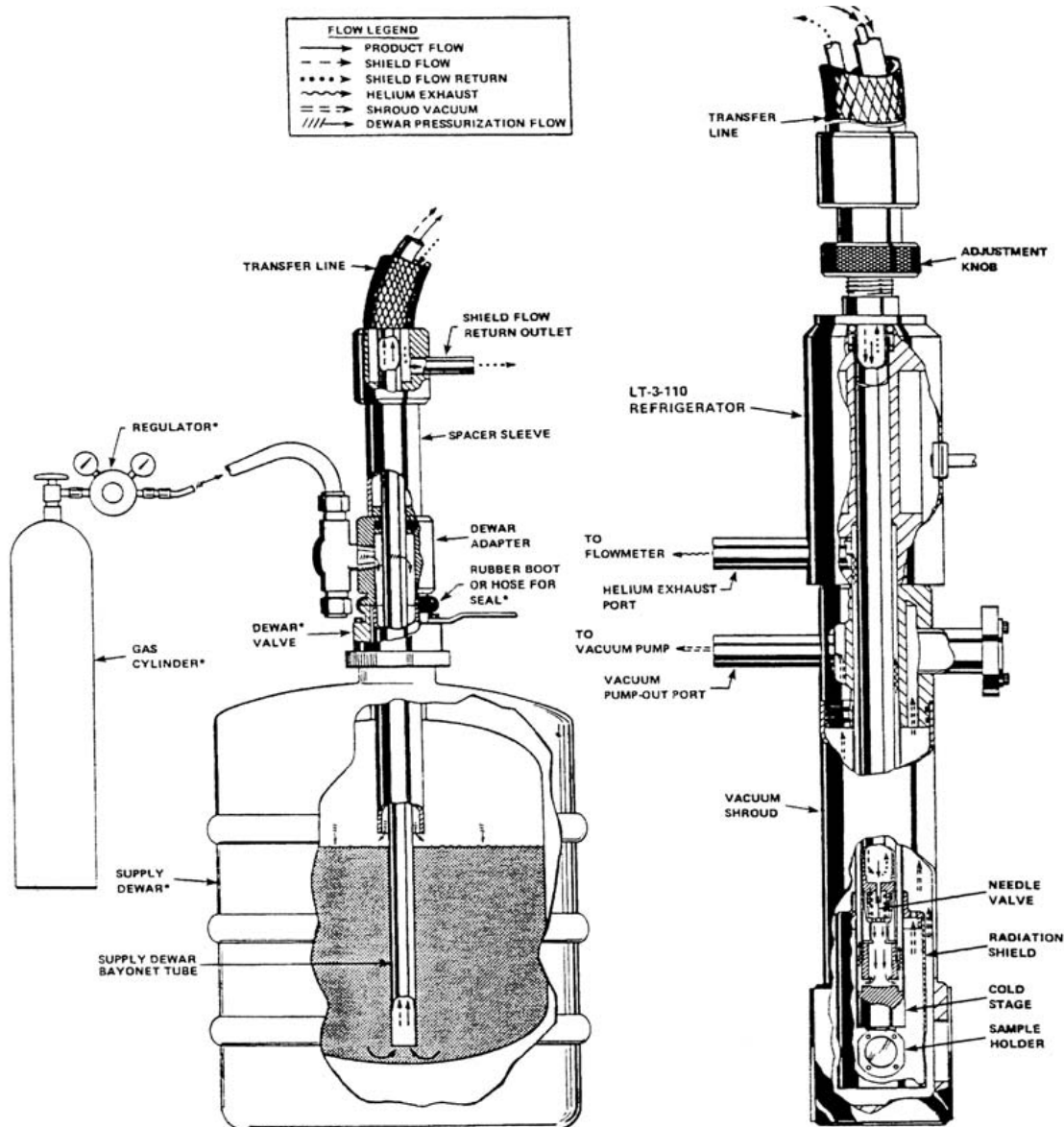
Figure 3.9-1. The cryostat system from right to left: the Helitran open cycle cryostat, liquid helium dewar, and compressed gas helium. (ARS, 2001)

The need for such stringent control arises from the instability of the pressure building capabilities in the liquid helium dewar. The dewar's internal pressure increased and decreased as helium boiled off. This boiling rate was normally constant but it did vary and formed an oscillating process. The gas pressure was relieved as a function of the flow of helium through the cryostat, much like a boiling pot of water; when the pressure builds, the lid lifts, letting the pressure out, and the lid falls to repeat the process. The helium in this case was pushing through the transfer line faster when the pressure increased but slower when it equalized. This made it difficult to hold the sample at a constant temperature. To aid the PID controller, a separate compressed gas helium cylinder was used to add pressure to the liquid helium tank in an effort to maintain the pressure on the liquid helium dewar. This gas cylinder also kept the pressure on the cylinder. As the liquid helium was used, the pressure building ability of the liquid helium decreased as the liquid level decreased.

A third aid that was used to hold the temperature stable was a needle flow valve, which limited the flow of helium as the temperature rose. This was done manually from 5 K to 20 K. For a normal data collection run, temperatures were maintained within a total of 0.1% error. While the sample data was collected, a temperature measurement was taken from the thermistor located at the sample mount at the same time. This temperature data was taken for all of the experimental data for one experimental run (Figure 3.9-2) to verify that the experiment was capable of maintaining the sample temperature while being automated with the above control devices.
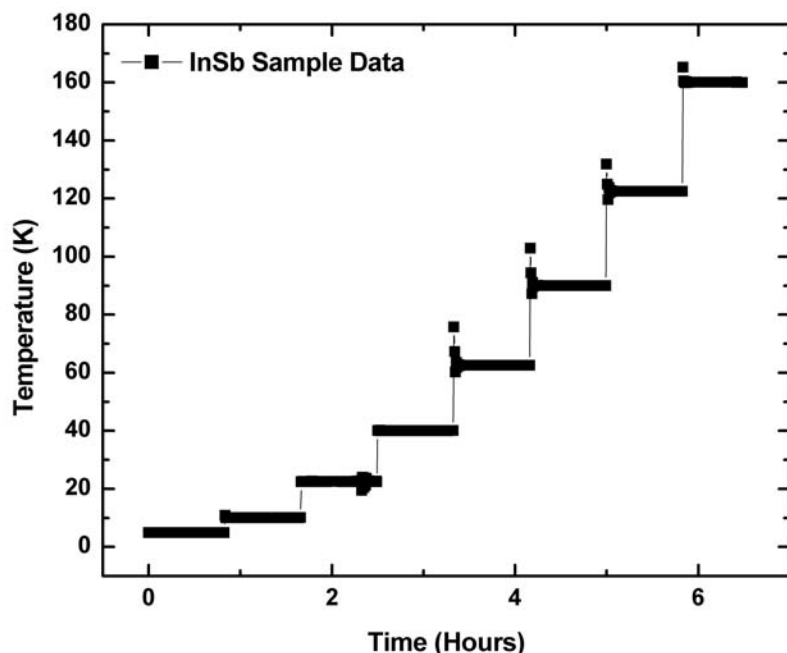
Figure 3.9-2. The temperature measurement taken with the optical absorption data for each point the sample temperature was collected. Note the oscillation at the beginning of the data collection where the temperature had been changed before the PID controller adjusted for error.

Rubber cement was used to mount the sample in the cryostat. Rubber cement is a solid when at cold temperatures such as below freezing of water. The thermal-conduction properties of rubber cement were studied, as well. To do this, the cryostat cold finger thermistor A, was physically attached using a set screw and indium. The other thermistor, B, was bonded to the cold finger using rubber cement in the same fashion that a sample would have been mounted. Care was taken to use the same amount of rubber cement as that which was used on the sample. The cryostat was vacuumed down to 20 mtorr and data was taken from 5 K to 300 K. The results of this test show that the rubber cement from 200 K to 300 K conducts heat as well as the physically attached thermistor A. However, from 5 K to 200 K rubber cement loses its thermal conductivity as a decaying exponential function (Figure 3.9-3).

51
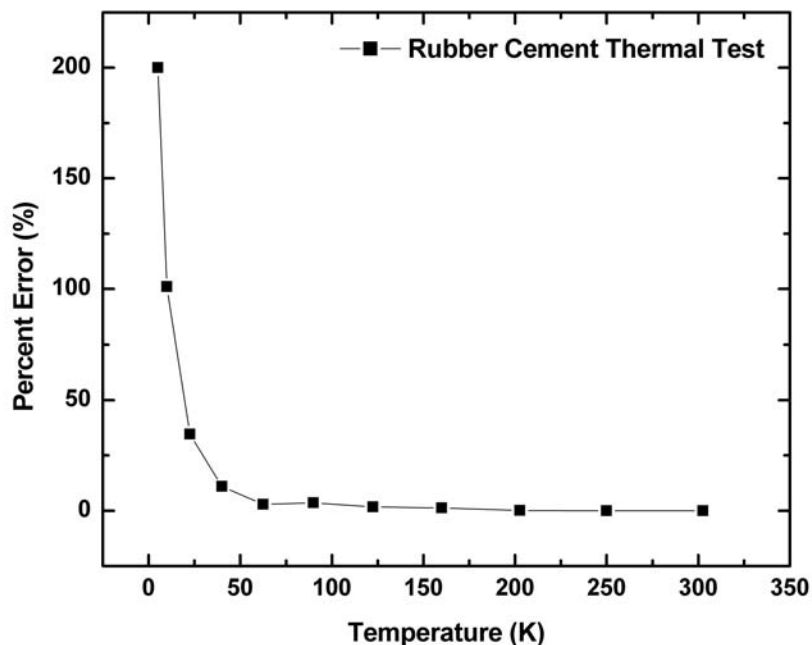
Figure 3.9-3. The percent error of measured temperature from actual temperature found in the sample data, which was introduced from using rubber cement as a bonding agent for the samples.

At 5 K, the total error formed by the lack of thermal conduction of rubber cement is 200%. This error has been treated appropriately in the model. During the analysis of the samples and forming of the analytical model, this error was propagated through appropriately so that the results were accurately compared.

3.10 The Vacuum System

The cryostat was pulled on by an Alcatel vacuum pump. This is done in order to remove ambient gases and moisture from the chamber, in turn lowering the pressure to mtorr range. The pressure of the system needed to be reduced in order to prevent frosting of the sample at cryogenic temperatures. The slightest amount of moisture in the chamber would form crystalline structures on the sample and windows that would hinder

52

photons from passing through the chamber. Also, the vacuum acted as an insulator and avoided thermal transfer from the room by conduction or convection. When the vacuum was being pulled on the system, it was not possible for any oil from the pump to find its way into the sample chamber. However, when the chamber was opened, the vacuum needed to be released in the cryostat. To do this, the vacuum pump was turned off and one of the fittings was loosened to vent atmosphere into the sample chamber. This would have allowed oil to back-flow into the cryostat as atomized oil particles from the vacuum pump and vacuum line, and thus, contaminate the sample and windows in the cryostat. If oil was to adhere to the sample and windows of the cryostat, it would have caused the irradiance to decrease. This would be an unknown amount of absorption and scatter off of the oil surface that would have caused a skew in the experimental data when compared to the calculated model fit. To prevent this from occurring, a one-way valve was placed close to the cryostat on the vacuum line. To break the vacuum, the valve was turned and the fitting on the cryostat was removed. This allowed ambient air to rush into the cryostat, and thus, prevented the possibility of oil exposure.

3.11 InSb Detectors

Two Cincinnati Electronics SDD-32EO-S1 single-element InSb detectors were housed in a cryogenic dewar that had a permanent vacuum chamber and cold window. The detector has a *dia* = 5 mm, and will not act as a field stop in the optical system. These detectors were cooled to 77 K with liquid nitrogen. This allowed the detectors to become sensitive to low levels of photons by binding up thermally excited electrons from the valence band. In turn, this also increased the signal-to-noise ratio. In Figure 3.11-1,

the incident laser pulse on the detector was tracked temporally, which is represented from right to left as the pulse struck the detector (high intensity) and then decayed (slope).

Electrons in the InSb material were stimulated by laser photons, and moved to the conduction band. Once the pulse had hit the detector, it needed time for those excited electrons to cool to the valence band from the conduction band. The response speed of the device was noted to be faster than the laser pulse repetition rate by visual inspection of the detector's response on the O-scope. When the DEOS laser was set to operate at 10.95 KHz, the InSb detector recovery to steady state was confirmed.

The InSb detectors were biased by a positive and negative 15 volts; this voltage was supplied by two separate HP power supplies. Some confusion of the proper set up of the power supplies can lead to erroneous results. The detectors were wired in the following way: The grounded wires from the two power supplies were wired together, while one power supply was grounded to its negative terminal and the other power supply was grounded to its positive terminal. The two detectors were wired in parallel to the power supplies to their proper terminals: one positive, one negative and one ground terminal. The grounded positive and negative terminals were not used.

In order to determine the percent transmittance through the InSb samples, a simple calibration was taken of the experiment. In this process, the absorption experiment was run without the samples. This allowed a value to be recorded that represents 100% transmission that can be used to generate the percent transmittance by dividing it by the data collected with the sample in place. The two detectors were both calibrated in this fashion and swapped back and forth to track any irregularities between the two detectors, an 8% error was found between the two detectors. In order to remove

the noise generated by the laser as previously discussed, the 100% transmission data also included data for tracking the laser. As the laser intensity fluctuated, the signal on the detectors also fluctuated, and once processed, this amount of variation can be accounted for in the data, reducing the total amount of error.
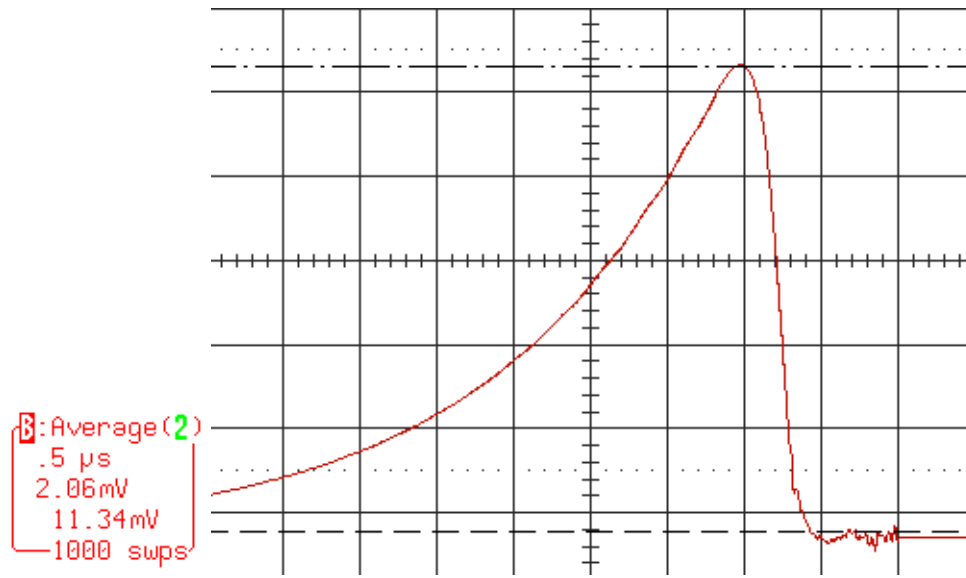
Figure 3.11-1. The response from an InSb detector averaged at 1000 scans, and displayed by an O-scope as a DEOS laser pulse struck the detector (right side) and then decays as a function of time to the left. The pulse is then recorded as a maximum value (mV) (dot dashed line).

A second calibration was performed between the two InSb detectors that were used in the experiment by means of monitoring the output voltage response from the detectors. This was done because some detectors exhibit non-linear responses between high and low irradiances. Three unique excitation power levels were used. The variance in these levels was induced by the Lasnix attenuator. The first measurement was taken at 6 mW, and the subsequent two were almost identical due to the attenuator's mesh screens being nominally the same attenuation. For the second two attenuated power levels, the attenuator's mesh screens were open in the back (O.B.), and open in the middle (O.M.)

55

while the rest were closed. Each measurement was taken as a function of time. When compared, the tracking detector (monitored laser output power during the experiment) and the sample detector (collected all data) have a linear relationship between the excitation power levels and the detector voltage response (Figure 3.11-2). This linear relationship between the high and low excitation powers incident on the detectors allowed for the exact DEOS laser excitation power to be known on the sample at any given point in time.
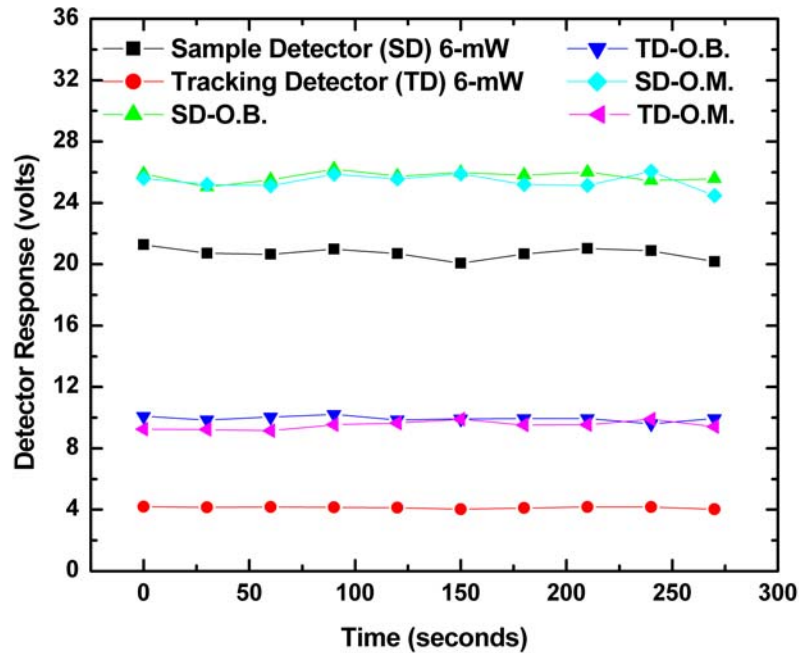
Figure 3.11-2. Results of the calibration between the two InSb detectors used in the experiment showing three unique excitation powers; first where all the mesh screens are closed, second with the back mesh screen open (O.B.), and finally with the middle mesh screen open (O.M.).

3.12 Oscilloscope

The O-scope was used in the experiment to collect the signal response from the InSb detectors. This process was dependent on the DEOS laser for the pulse repetition

rate which was used as the trigger for the O-scope. Once set, the trigger allowed the O-scope to collect data at each pulse when the laser fired. These collections were averaged with 500 pulses in order to raise the signal-to-noise ratio. The values were collected and sent to the computer via ethernet connection through a network hub between the laptop and O-scope.

For clarity, the data collected by the O-scope and averaged will be referred to as a scan, and the data that is collected by LabVIEW and stored will be referred to as a data point. When the system was first run, there had been a large amount of noise in the scans. In order to increase the signal-to-noise ratio, the scans were collected at 10,000 scans and averaged for one data point. The reason this was done was that there are 10,000 pulses per second being emitted by the laser when the laser is set at 10 kHz. This gave a known integration time for the scans that were taken, and a good foundation for statistical averaging. When looking at statistics alone, the noise-to-signal ratio was not significantly affected by taking smaller intervals. Separate runs were collected repetitively, only changing the integration time of the collected scans to prove this point. The data taken at 1,000 scans and compared to the data taken at 200 scans is surprisingly almost identical. The signal-to-noise ratio goes on the order of Sqrt[n], where n is the number of data points being collected.(Bohn: 2007). Once the scans were collected past 200 iterations, no significant appreciation occurred in the data quality. For this reason, the data iteration rate was stepped back to 500 for each scan. These 500 scans were averaged to form one data point that was passed along to LabVIEW.

3.13 Automation

LabVIEW 8.5 Professional is a software package made by National Instruments that allows the user to program sophisticated operations with ultimately unlimited potential. To fully explain the codex used would be outside the scope of this document. Instead, the general understanding of LabVIEW's function and role in the experiment will be discussed.

The front panel (user controls) to the experiment (Figure 3.13-1) allowed for direct manipulation of the three automatable devices. The linear stage component can be found on the far left. The controls from top to bottom are as follows: the communications port setting, the step size in 1/2 μm increments, the drive command (other commands can be found in the Zaber user manual), the number of steps to complete for each temperature, and the starting position.

In order to operate the experiment as desired, several for-loops were constructed with the necessary drivers to run the O-scope, temperature controller, and linear stage. These loops were sequenced by a chronological ordering which gives rise to the following process (Figure 3.13-2). First, the temperature controller was signaled to a desired set point, or temperature. Then, a period of time passed so that the PID algorithm could auto-tune the required heater output requirements, done in order to maintain the temperature inside the cryostat. Next, the linear stage was signaled to move into the starting position of the experiment, a negative z-distance of 2 cm from the focal point. After this occurrence, the O-scope's manually configured settings were saved to LabVIEW and stored back into the O-scope. This resetting of the configuration in the O-

scope allowed it to cycle for each data collection. Once the linear stage reached the starting position and the preset delay time was reached, the O-scope began to collect 500 scans of data for that position on the z-axis. This data was averaged by the O-scope; once the average was complete, all raw data was discarded by the O-scope. This averaging took place for the two signals from both InSb detectors, recalling that they were collecting data on the DEOS laser and the transmitted signal from the sample. These values were collected by LabVIEW through the use of a network hub which connects the laptop and O-scope together. The next segment in LabVIEW signaled the temperature controller to return the temperature measured inside the cryostat which is saved via USB connection to the laptop from the temperature controller. The linear stage was subsequently signaled to move a desired step size toward the focal point in the z-axis, and the data collection process started over again. This sequence of events continued until the stage had moved through the focal point to an equal positive distance on the z-axis from the starting point. This was referred to as one collection of data for a desired temperature. Now, the original process starts over for the next incremented temperature for all eleven temperatures. The temperature in Kelvin was determined by

$$T = \frac{x^2}{4} 10 \qquad (3.6)$$

where x is an integer value 1-11 (Table 3.13-1) that corresponds to the temperature-for-loop iteration number, (Figure 3.13-2). Recall that the original signal from the InSb detectors was discarded by the O-scope after the averaging of the collected data. The averaged data was represented as a waveform which shows the temporal response from the detector as previously mentioned. LabVIEW performed a magnitude measurement

59

on the waveform from the averaged O-scope data. The magnitude of the waveform represents the total irradiance incident on the detector. This value was read as a voltage response from the detector's calibration and converted to percent transmission.
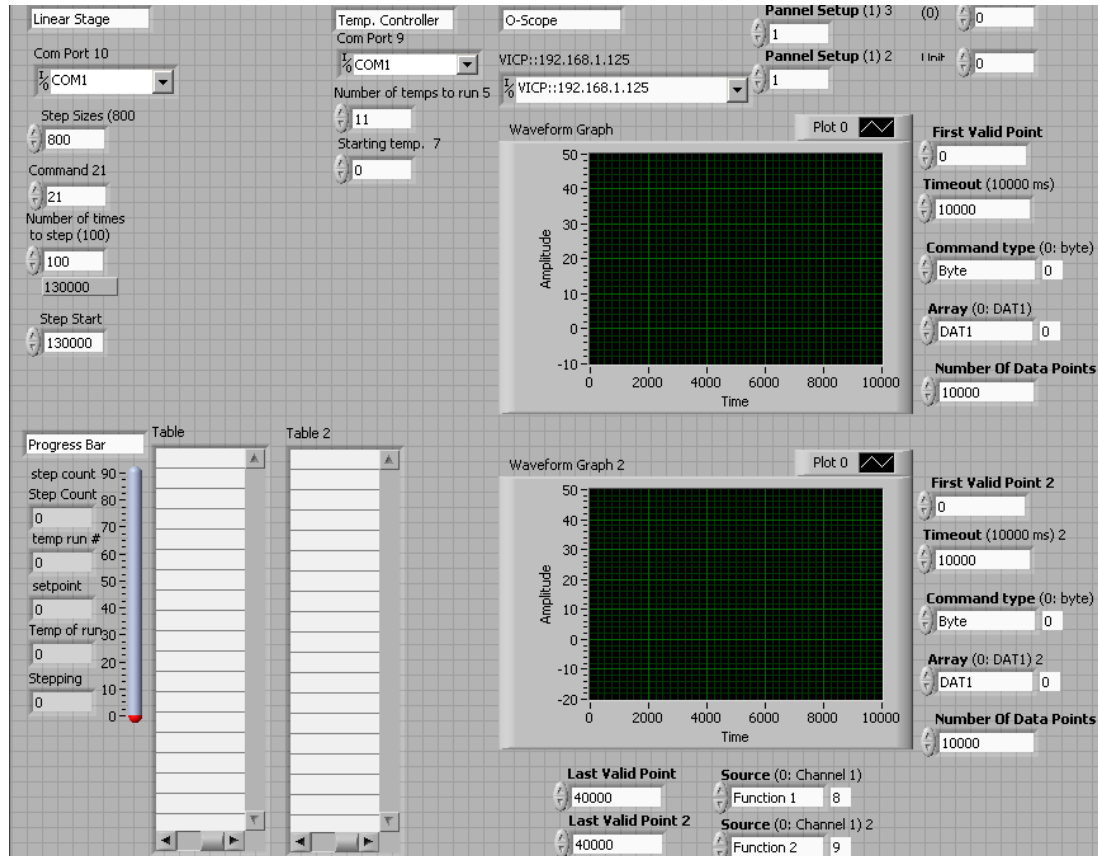
Figure 3.13-1.   The front panel (operators controls) of the LabVIEW virtual instrument that automated the experiment.   Note controls for the O-scope, temperature controller, linear stage and a progress report section.

Table 3.13-1. The output given by Eq. (3.7), which gives the temperature set point of the cryostat as a function of an integer value (1-11) corresponding to the iteration number of the Temperature-for-loop.

$x = 1$ ….......... $T = 2.5$-K $x = x = 4$ ……. $T = 40$-K $x = x = 7$ ……. $T = 122.5$-K$x = x = 10$ ……. $T = 250$-K

$x = 2$ ….......... $T = 10$-K $x = x = 5$ ……. $T = 62.5$-K $x = x = 8$ ……. $T = 160$-K $x = x = 11$ ……. $T = 302.5$-K

$x = 3$ ….......... $T = 22.5$-K $x = x = 6$ ……. $T = 90$-K $x = x = 9$ ……. $T = 202.5$-K

Figure 3.13-2. The different for-loops of the virtual instrument which automated the experiment.

3.14 Conclusion to Experimental Apparatus

Throughout this chapter, detailed explanations of the experimental apparatuses were provided to allow future research to be performed or allow for reproduction of the results by another party without any assumptions. Without the detailed explanations, the integrity and validity of the results may have been questioned. Having a thorough understanding of how the data was collected, the mathematical model that reproduces the data can be discussed.

4   Mathematical Modeling

In this chapter, a solid state physics model for the absorption-saturation phenomenon found in the InSb material will be discussed.   The model predicts and verifies the experimental data by allowing a unique carrier lifetime to be found for each irradiance value. This model advances on a previous model by Norman where the sample was taken as a single unit, at one temperature, and a linear irradiance pattern.

4.1   Considerations for Semiconductors

In this model, the material is characterized at eleven different temperatures from 2.5 K to 300 K and for increasing photon irradiance. The sample is then interrogated as separate slices, where the first slice will absorb photons and leave a smaller amount to be absorbed in the next slice. The photon irradiance will also decrease as it moves through the sample and accounts for the initial Gaussian laser beam profile.

The model utilizes an engineering estimate known as the parabolic band approximation instead of quantum mechanics; the approximation was discussed in the physics chapter. The *L-valley* and *X-valley* are ignored within the model because they are much wider in energy than the *Γ-valley* (Figure 4.1-1). The DEOS laser excitation wave length of λ = 4.636 μm will have energy of E_{deos} = 0.269 eV. This is known from $E = \dfrac{hc}{\lambda}$ where h is Planck's constant and c is the speed of light. Comparing the three valleys' energies, E_L(300 K) = 0.68 eV, E_x(300 K) = 1.0 eV, E_g(300 K) = 0.17 eV, it can be seen that E_{deos} will pass through the *L-valley* and *X-valley*; thus, all optical

absorption for this wavelength will take place at E_g. In order to find E_g as a function of temperature, the Varshni equation and parameters are used

$$E_g(T) = E_g(0K) - \frac{\alpha T^2}{T + \beta}$$ (3.7)

where $E_g(0\ K)$ is the band gap energy at 0 K, α is a parameter used for fitting and has units of eV/K, and β is related to the Debye temperature, the temperature at which the vibrational modes of the crystal begin to be excited.(Marciniak,1995:3-21) This allows empirical data to be used in order to plot the conduction band-edge. The values used in this model for α = 6 x 10^{-4} eV/K and for β = 500 K.(Ioffe, 2008) The valence band does not need to be calculated because it is held at zero for the approximation.
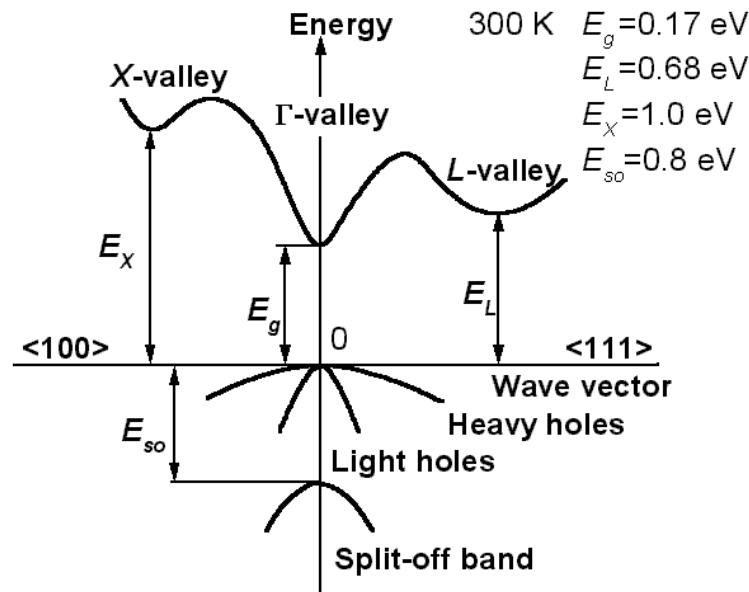
Figure 4.1-1. The band structure of InSb at 300K. Optical absorption for a wavelength of λ = 4.636 μm and energy, E_{deos} = 0.269 eV, will only occur at E_g. All other transitions noted by E_x E_L E_{so} will allow this wavelength to pass through.(Levinshtein, 1996: 92)

The InSb samples are clearly degenerately doped (Figure 4.1-2); there is no freeze-out of the carriers present. The true Fermi-energy level is shown in Figure (4.1-3).

The number of donor atoms added to the material will shift the Fermi-energy level; this is what gives rise to the extrinsic Fermi-energy level. In order to find the extrinsic Fermi-energy level, the doping concentration, N_d^+, needs to be incorporated into the model. Hall measurements were taken on the InSb samples for temperature-dependent sheet carrier densities, which, when divided by the depth of the material, gives the total number of ionized electrons, N_d^+ (Figure 4.1-4). In order to find the doping concentration from N_d^+, the intrinsic carrier concentration, $n_i(T)$, is needed

$$n_i(T) = \sqrt{n_o p_o} \tag{3.8}$$

where n_o and p_o are given by equations (2.25) and (2.26), respectively. The intrinsic carriers are subtracted from the total number of excited carriers to give the doping concentration, $N_d = N_d^+ - n_i$. Recall that the sample is n-type; therefore, the acceptor atoms are negligible ($N_a = 0$).

The ionization energy of the dopant can also be found from the Hall measurements. It is known that tellurium (Te) is a shallow donor in InSb, with an ionization energy of 0.7 meV.(Ioffe, 2008) The ionization energy of the donors is determined by assuming that the sheet carrier concentration, n_s, is proportional to

$$n_s(T) = e^{\frac{-E_A}{k_B T}} \tag{3.9}$$

where E_A is the activation energy, and Equation (3.9) holds true for high temperatures. The activation energy can then be extracted using a graphical method, an Arrhenius plot, where the slope of the curve is fitted using a least squares fit as $\ln(n_s)$ versus $1/T$ (Figure 4.1-5).
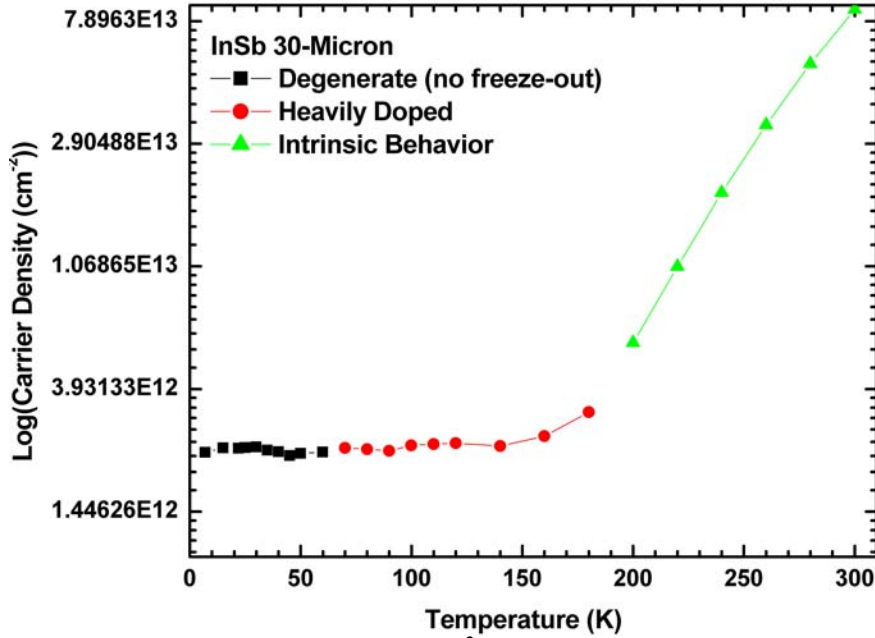
Figure 4.1-2. The carrier density (cm^{-2}) of the 30-μm InSb sample plotted on a Log scale versus temperature (K) showing the behavior of the free carriers as temperature changes, allowing for the known intrinsic behavior and heavily doping effects to be seen.

The ionization energy is then subtracted from the band gap energy; this gives rise to Te's donor energy level in the band gap: $E_D(T) = E_g(T) – E_{ion}$. This ionization energy is then used to find the number of ionized donors given as

$$n_d(T, E_f) = \frac{N_d}{1 + 2Exp\left(\dfrac{E_f - E_D(T)}{k_B T}\right)}$$ (3.10)

The ionized donor concentration gives the number of dopant atoms that have been thermally ionized due to lattice heating. Unfortunately, when the sample is degenerately doped, the Arrhenius plot method yields incorrect results for the ionization energies of the dopants. It is then impossible to determine what the doping concentration is between the two dopant species. For this reason, a known value was assumed for Te's ionization

66

energy (0.7 meV). It was then assumed in the model that only Te was present in the InSb

samples, and the second species was neglected.
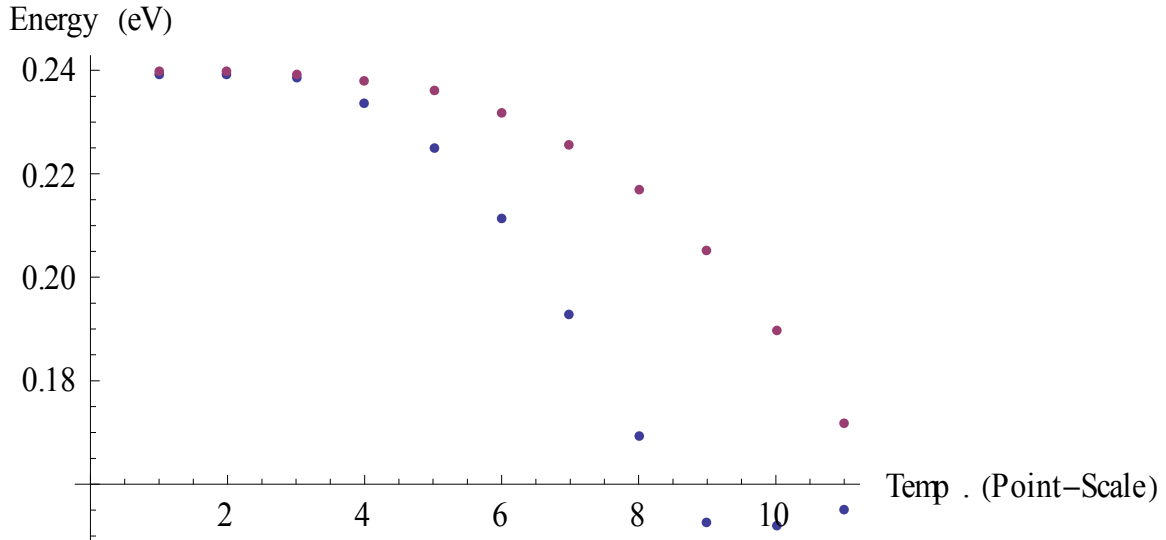
Energy (eV)

Figure 4.1-3. The extrinsic Fermi-Energy level of the InSb samples. The purple dots (top) represent the conduction bandedge and the blue dots (center) represent E_f. The x-axis is displayed as iteration numbers, where the values range from 0 to 11 and represent 0 K to 302.5 K, respectively.

It should be noted, that the dopant concentration in the sample is eight orders of

magnitude less than the number of excited carriers from the laser while the sample is

being bleached; this would dwarf the effects that the dopant species would have in the

sample. For this reason, the dopants could have been neglected in the model altogether

due to their insignificance to the dynamic system under high irradiance.
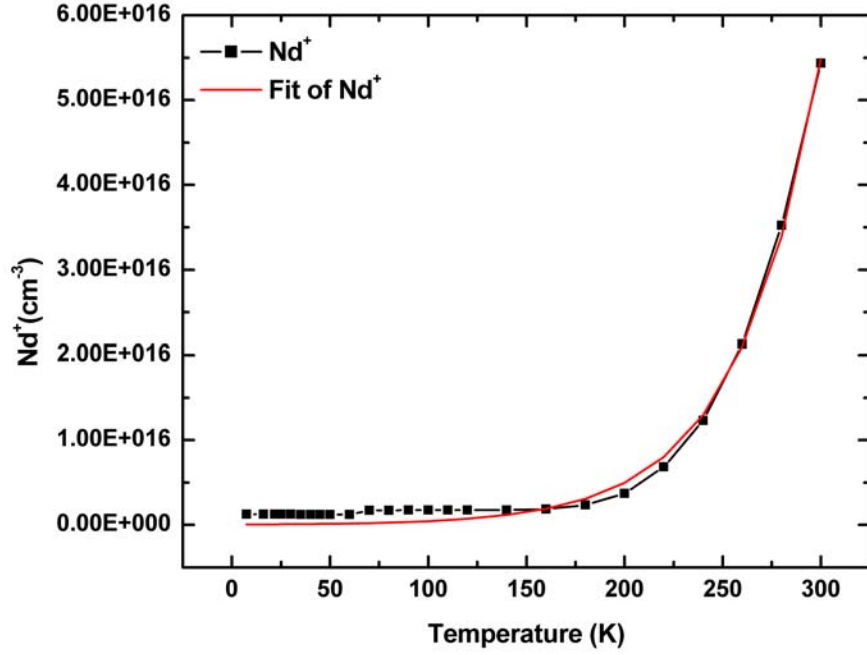
Figure 4.1-4. **Hall measurement data showing the temperature-dependent total number of ionized electrons, N_d^+, and the fit to the empirical data shown in red for the 15-µm InSb sample.**
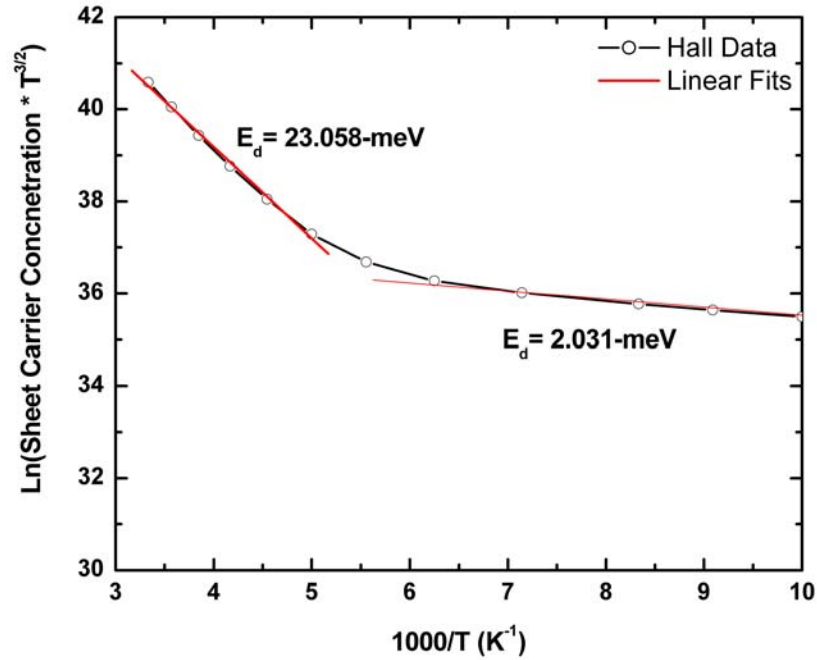
Figure 4.1-5. **The sheet carrier concentration on a natural log scale verse 1000/T, when fitted to linear lines. The ionization energy of the two impurities can be deduced from the slope of the line. Plotted for the 15 µm InSb sample.**

The density of states for the conduction band, $g_c(E,T)$, and valence band, $g_v(E)$, are also needed in order to calculate the extrinsic Fermi-energy level

$$g_c(E,T) = (2m_c*)^{3/2} \frac{\sqrt{E - E_g(T)}}{2\pi^2\hbar^3} \qquad (3.11)$$

$$g_v(E) = (2m_v*)^{3/2} \frac{\sqrt{-E}}{2\pi^2\hbar^3} \qquad (3.12)$$

where E is an energy that is left open for computations later on, but it does give rise to the extrinsic Fermi-energy level and cannot be assumed that they are one in the same. Here, E is a range of possible energy levels. The Fermi-Dirac PDF is then needed in order to find the free-electron and hole concentrations in the conduction and valence bands

$$f(E, E_f, T) = \frac{1}{Exp\left(\dfrac{E - E_f}{k_B T}\right) + 1} \qquad (3.13)$$

where E_f is the extrinsic Fermi-energy level; note that it is left as a variable in this equation in order to solve for a numerical solution later on. The PDF is then multiplied by the density of states for the conduction band and then the valence band and integrated, which gives rise to the free-electron concentrations as previously mentioned

$$n(T, E_f) = \int_{E_g(T)}^{10E_g(T)} g_c(E,T) f(E, E_f, T) dE \qquad (3.14)$$

where the limits of integration go from the edge of the conduction band, $E_g(T)$, to what can be considered infinity in the numerical solution, $10E_g(T)$. The upper limit is assuming that no electrons will populate the higher states. For holes in the valence band, a similar approach is taken

$$p(T, E_f) = \int\limits_{-10E_g(T)}^{0} g_v(E)\big(1 - f(E, E_f, T)\big)dE \qquad (3.15)$$

where the limits of integration for the holes in the valence band range from well below any possible filled states, *-10E_g(T)*, to the edge of the valence band, zero. Recall that in the parabolic band approximation the valence band is held constant at zero.

In order for a numerical solution to be found, one can use charge neutrality, which must be maintained. In the model, a "FindRoot" command is used that allows for many iterations to be performed autonomously between a range of 2.4×10^{-20} J and 3.85×10^{-20} J. The range was selected using a graphical solution to the charge neutrality equation, given as

$$n(T, E_f) - p(T, E_f) - n_d(T, E_f) = 0 \qquad (3.16)$$

where the number of free electrons, minus the number of holes, minus the number of free electrons from dopants, must equal zero. Note that Equation (3.16) allows for the temperature to be varied. Within the model, one temperature is selected and then the extrinsic Fermi-energy level is numerically solved; once completed, the next temperature is selected and the corresponding Fermi-energy is solved, through all eleven temperatures.

Now that the extrinsic Fermi energy level is known, the quasi-Fermi-energy levels can be found, as can the corresponding quasi-equilibrium electron and hole concentrations for the conduction and valence bands, respectively. The quasi-Fermi function for the conduction band is given by

$$f_c(E, E_{FC}, T) = \frac{1}{Exp\left(\dfrac{E - E_{FC}}{k_B T}\right) + 1} \tag{3.17}$$

where E_{FC} is the quasi-Fermi-energy level in the conduction band, T is once again left open for the eleven different temperatures, and E is then left open again as the energy levels that can be occupied in the band. For the valence band,

$$f_v(E, E_{Fv}, T) = \frac{1}{Exp\left(-\dfrac{E - E_{Fv}}{k_B T}\right) + 1} \tag{3.18}$$

where E_{FV} is the quasi-Fermi-energy level in the valence band and E is left open for integration later on within the states that can be occupied in the valence band. From here, the quasi-equilibrium hole concentrations can be found from

$$\Delta n(T, E_{FC}, E_f) = \left(\int_{E_g(T)}^{\infty} g_c(E, T) f_c(E, E_{fc}, T) dE\right) - n(T, E_f) - n_d(T, E_f) \tag{3.19}$$

where it can be noted that the limits of integration follow the same principle as used before, E is a range of energy that spans the density of states that the electrons can fill. The quasi-equilibrium hole concentration is given by

$$\Delta p(T, E_{Fv}, E_f) = \left(\int_{-\infty}^{0} g_v(E) f_c(E, E_{fv}, T) dE\right) - p(T, E_f) \tag{3.20}$$

where the limits of integration follow as they did before from the allowed states that can be filled. Unfortunately, Δn and Δp create computational errors when the numerical integration is solved in Mathematica and n and p, respectively, are subtracted from them. The integration creates numbers that are extremely large. When a very large number is subtracted from a second very large number, n and p, the machine precision is too small

to maintain the necessary significant digits required for a meaningful solution. For this reason, Δn and Δp, were simplified. The true expression for Δn is

$$\Delta n = \int_{E_g(T)}^{\infty} g_c(E,T)\frac{1}{e^{\frac{E-E_{FC}}{k_BT}}+1}dE - \int_{E_g(T)}^{\infty} g_c(E,T)\frac{1}{e^{\frac{E-E_f}{k_BT}}+1}dE - n_d(T,E_f). \quad (3.21)$$

The simplified expression for Δn that is mathematically incorrect is

$$\Delta n = \int_{E_g(T)}^{\infty} g_c(E,T)\left\{\left(e^{\frac{E_{FC}-E}{k_BT}}+1\right)-\left(e^{\frac{E_f-E}{k_BT}}+1\right)\right\}dE - n_d(T,E_f) \quad (3.22)$$

The benefit of this expression is that it allowed the numerical integration to be solved in Mathematica quickly. Its incorrectness mathematically was not completely realized until after many hours of computation time had been spent generating the data found in Chapter 6. Reperforming this analysis with a mathematically correct model is not practical now with current computational ability, and the time allotted for this thesis. Therefore, an analysis of the differences in the results generated by Equations(4.17) and (4.18) will be discussed in Chapter 6.1.5.

Returning to Equation(4.18), the ones cancel from the exponentials.

$$\Delta n = \int_{E_g(T)}^{\infty} g_c(E,T)\left\{\left(e^{\frac{E_{FC}-E}{k_BT}}\right)-\left(e^{\frac{E_f-E}{k_BT}}\right)\right\}dE - n_d(T,E_f) \quad (3.23)$$

Then, e^{-E/k_BT} can be factored from exponentials.

$$\Delta n = \int_{E_g(T)}^{\infty} g_c(E,T)e^{\frac{-E}{k_BT}}\left\{e^{\frac{E_{FC}}{k_BT}}-e^{\frac{E_f}{k_BT}}\right\}dE - n_d(T,E_f) \quad (3.24)$$

This leaves the exponentials as constants where they can be positioned outside of the integral.

$$\Delta n = \left\{ e^{\frac{E_{FC}}{k_BT}} - e^{\frac{E_f}{k_BT}} \right\} \int\limits_{E_g(T)}^{\infty} g_c(E,T) e^{\frac{-E}{k_BT}} dE - n_d(T,E_f) \qquad (3.25)$$

Then, the density of states can be expanded,

$$\Delta n = \left\{ e^{\frac{E_{FC}}{k_BT}} - e^{\frac{E_f}{k_BT}} \right\} \int\limits_{E_g(T)}^{\infty} \left(2m_c{}^*\right)^{3/2} \frac{\sqrt{E - E_g(T)}}{2\pi^2\hbar^3} e^{\frac{-E}{k_BT}} dE - n_d(T,E_f) \qquad (3.26)$$

and constants within the density of states can be moved outside of the integral, as well.

$$\Delta n = \frac{\left(2m_c{}^*\right)^{3/2}}{2\pi^2\hbar^3} \left\{ e^{\frac{E_{FC}}{k_BT}} - e^{\frac{E_f}{k_BT}} \right\} \int\limits_{E_g(T)}^{\infty} \sqrt{E - E_g(T)} e^{\frac{-E}{k_BT}} dE - n_d(T,E_f) \qquad (3.27)$$

Let the constants be equal to $\beta = \dfrac{\left(2m_c{}^*\right)^{3/2}}{2\pi^2\hbar^3} \left\{ e^{\frac{E_{FC}}{k_BT}} - e^{\frac{E_f}{k_BT}} \right\}$ so that

$$\Delta n = \beta \int\limits_{E_g(T)}^{\infty} \sqrt{E - E_g(T)} e^{\frac{-E}{k_BT}} dE - n_d(T,E_f). \qquad (3.28)$$

Then, let $u = E - E_g(t)$ and $du = dE$ which gives

$$\Delta n = \beta \int\limits_{E_g(T)-E_g(T)}^{\infty} \sqrt{u} e^{\frac{-\left(u+E_g(T)\right)}{k_BT}} du - n_d(T,E_f). \qquad (3.29)$$

Then, $1/k_BT$ can be taken out of the integral,

$$\Delta n = \beta e^{\frac{-E_g(T)}{k_BT}} (k_BT)^{3/2} \int\limits_{E_g(T)-E_g(T)}^{\infty} \sqrt{\frac{u}{k_BT}} e^{\frac{-u}{k_BT}} \frac{du}{k_BT} - n_d(T,E_f) \qquad (3.30)$$

and then, by letting $z = u/k_BT$ and $dz = du/k_BT$,

$$\Delta n = \beta e^{\frac{-E_g(T)}{k_BT}} (k_BT)^{3/2} \int\limits_{\frac{E_g(T)-E_g(T)}{k_BT}}^{\infty} \sqrt{z} e^{-z} dz \qquad (3.31)$$

where the lower integration limit is equal to zero and integrand gives

73

$$\int_0^\infty \sqrt{z}\, e^{-z}\, dz = \frac{\pi}{2}.$$ (3.32)

The final result is a simpler equation given by

$$\Delta n(T, E_{FC}, E_f) = \frac{\left(2m_c{}^*\right)^{3/2}}{2\pi^2\hbar^3}\left\{ e^{\frac{E_{FC}}{k_B T}} - e^{\frac{E_f}{k_B T}} \right\} e^{\frac{-E_g(T)}{k_B T}} (k_B T)^{3/2}\frac{\pi}{2} - n_d(T, E_f).$$ (3.33)

The same procedure is used to simplify Δp to

$$\Delta p(T, E_{FV}, E_f) = \frac{\left(2m_v{}^*\right)^{3/2}}{2\pi^2\hbar^3}\left\{ e^{\frac{-E_{FV}}{k_B T}} - e^{\frac{-E_f}{k_B T}} \right\}(k_B T)^{3/2}\frac{\pi}{2}.$$ (3.34)

At this point, the experimental set up needs to be considered in the model. The wavelength of the laser, the power of the laser, the beam waist of the laser, and optics used all play a part in the average irradiance that is incident on the sample. In Section 3.5, the details of the geometric optics were discussed. Now, those conclusions will be used to find the number of induced carriers, ΔN, from the photon irradiance. This phenomenon of carrier generation was discussed in Chapter 2, where photons are absorbed and give rise to free electrons or an excited carrier concentration which is given by

$$\Delta N(z, h\nu, E_{FC}, E_{FV}, T) = \frac{E_p(z)}{t}\left(1 - Exp\left(-\alpha(h\nu, E_{FC}, E_{FV}, T)t\right)\right)(1 - R)\tau$$ (3.35)

where E_p is the photon irradiance as a function of distance, t is the thickness of the sample, α is the absorption coefficient, $h\nu$ is the laser's energy, T is the lattice temperature, and E_{FC} and E_{FV} are the quasi-Fermi-energy levels for the conduction and valence bands, respectively, τ is the carrier recombination lifetime of InSb, and R is the Fresnel reflection

$$R = \left(\frac{n_1 - n_2}{n_1 + n_2} \right)^2 \qquad (3.36)$$

where $n_1 = 1$ is the index of refraction of air and $n_2 = 3.9$ is the index of refraction of InSb in the IR.(Ioffe, 2008) This allows for the quasi-Fermi-energy levels to be solved simultaneously, and thus, gives rise to the absorption coefficient, α. Before looking at α, the quasi-Fermi functions need to be defined for the conduction and valence bands, respectively

$$fc_2(hv, E_{FC}, T) = \frac{1}{\left(Exp\left(\dfrac{E_2(T, hv) - E_{FC}}{k_B T} \right) + 1 \right)} \qquad (3.37)$$

$$fv_2(hv, E_{FV}, T) = \frac{1}{\left(Exp\left(\dfrac{E_1(T, hv) - E_{FV}}{k_B T} \right) + 1 \right)} \qquad (3.38)$$

where E_1 and E_2 are energy states in the valence and conduction bands, respectively, given as

$$E_1(T, hv) = -m_r^* \left(\frac{hv - E_g(T)}{m_v^*} \right) \qquad (3.39)$$

$$E_2(T, hv) = E_g(T) + m_r^* \left(\frac{hv - E_g(T)}{m_c^*} \right) \qquad (3.40)$$

where m_r^* is the reduced effective mass, given as

$$m_r^* = \frac{1}{\dfrac{1}{m_c^*} + \dfrac{1}{m_v^*}} \qquad (3.41)$$

75

and $hv_{12} = hv = E_{does} = E_2 - E_1$ is the photon energy for the transition between those two energy states, E_1 and E_2. Then, the absorption coefficient as a function of excited carriers, ΔN, can be expressed as,

$$\alpha(hv, E_{FC}, E_{FV}, T) = \alpha_{TE} \left(fv_2(hv, E_{FV}, T) - fc_2(hv, E_{FC}, T) \right) \tag{3.42}$$

where α_{TE} is at a single photon energy, *i.e.*, that of the laser, and B_{12} and the density-of-states integral become the proportionality constant between $\alpha(E_{deos})$ and $fv_2(E_1) - fc_2(E_2)$. Spectral absorbance measurements were performed on both the 15- and 30-μm InSb samples from 10 to 300 K using a Biorad FTS-60AFTIR spectrometer, and found $\alpha_{TE}(E_{deos})$ to be ~4,000 cm^{-1} at 77 K. (Norman, 2006) The samples also had a second measurement performed on them for $\alpha_{TE}(E_{deos})$ to be ~3,200 cm^{-1} at 78 K.

The quasi-Fermi-energy levels for the conduction and valence bands can now be solved numerically using a similar approach to that which was used to find the extrinsic Fermi-energy level. It was noted earlier that the two quasi-Fermi-energy levels need to be solved simultaneously; this is because ΔN is a function of both quasi-Fermi-energy levels. The quasi-equilibrium hole concentration is understood to equal ΔN and the quasi-equilibrium electron concentration equals ΔN, as well. Knowing this allows for the following two equations to be solved simultaneously

$$\Delta n \left(T, E_{FC}, E_f(T) \right) = \Delta N \left(z, E_{deos}, E_{FC}, E_{FV}, T \right) \tag{3.43}$$

$$\Delta p \left(T, E_{FV}, E_f(T) \right) = \Delta N \left(z, E_{deos}, E_{FC}, E_{FV}, T \right) \tag{3.44}$$

where both Equation (3.43) and (3.44) are solved for the eleven different temperatures along with increasing photon irradiance which increases ΔN as the sample is moved into

76

the focal point of the DEOS Laser. When the iteration is completed, it gives the quasi-Fermi-energy level for the conduction band and valence bands, respectively. These solved values are used in the absorption coefficient, α, (Equation (3.42)) to plot the transmission which is given as

$$T = 1 - R_2 - e^{-\alpha(hv, E_{FC}, E_{FV}, T)t} \tag{3.45}$$

where t is the thickness of the sample and R_2 is the reflection coefficient of the second interface of the sample. The second interface is located at the exiting side of the InSb sample from the laser irradiance.

The data generated by the model was produced by manually selecting values for τ at each of the 50 data points along the z-axis that correspond with the experimental data. Note that only 30 values were manually selected due to time constraints. After the values were recorded, they were fit in Origin to a second-order polynomial, an example is shown in Figure 4.1-6. The polynomial represents τ as a function of irradiance while being investigated in the model as an iteration number. The iteration number represents a defined step size used in the experiment to translate the sample through the z-axis. In the model, the iteration number was used to allow the for-loops to translate the sample through the same z-axis. In simple terms, the irradiance changes at each iteration number to correspond to the same dynamic change found in the experiment. In the model, the iteration number loops the equations from one irradiance level to the next. The new polynomial function for τ allows for the total density of carriers to be found within the material at each irradiance. Having a function for τ produces errors within the model that are then presented in the generated data. Any anomaly present in the generated data sets

77

is due to fitting τ instead of selecting each of the 50 values manually. The error induced by these anomalies is negligible.
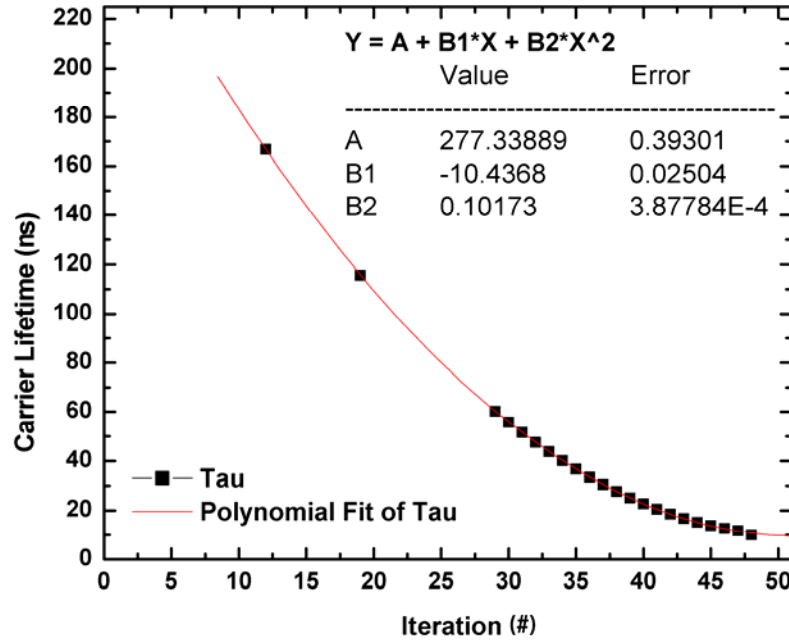
Figure 4.1-6 An example of the second-order polynomial fit of the carrier lifetime as a function of the step iteration number.

4.2 Conclusion to Mathematical Modeling

This chapter explained the mathematical model of the experiment. It also explained how the transmission data was generated by selecting a unique carrier lifetime for each iteration number, where the carrier lifetimes were fit to a second-order polynomial. Having investigated the model, the experimental data will be presented next, in Chapter 5, before comparison to the model's results. The data that was generated by the model will be presented in Chapter 6.

5 Experimental Data and Results

In this chapter, the raw data from the experiment is presented for both of the samples, 15- and 30-μm InSb. The Hall measurements are discussed first, which provides detailed information about the samples. Second, the raw experimental data is presented and discussed. Third and last, the data is presented as transmission versus irradiance, which allows for a comparison between the data sets to be made.

5.1 Hall Data

Hall measurements were taken on both the 15-μm sample and the 30-μm sample. From this data, it has been determined by comparing the data sets graphically that the doping level is identical in both samples (Figure 5.1-1). It can then be assumed that both the samples are identical in physical composition, only dissimilar by geometry because the doping density is the same. If the doping level of the two samples had not been identical, it would have been difficult to form a concise and well-developed understanding of the carrier concentration and mobility interactions and how they affect the absorption and ultimately the saturation of the material at hand.

It should be understood that the sample is being bleached by photons. This process is known as absorption saturation. Thus, the terms saturate, saturation, and bleach are all referring to the same process where the material can no longer absorb photons and becomes transmissive.

79
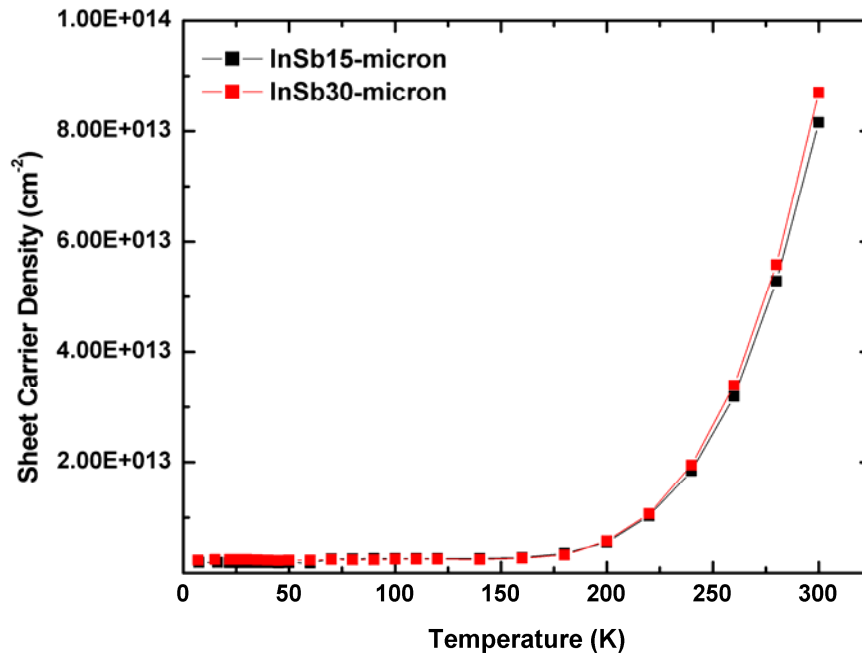
Figure 5.1-1. Comparison of the doping levels for the 15- and 30-μm InSb samples through the sheet carrier density.

5.2 Raw Data

The z-scan experiment produced data (Figure 5.3-21) as a function of position versus voltage response, which was then converted to percent transmission by means of knowing the total photon flux without the sample in place. As the sample position is incremented in the z-axis, the laser irradiance increases, but for comparison reasons, the x-axis of the plots will not be converted yet. At 5 K, both the 15- and 30-μm InSb samples had begun to bleach, where the absorption begins to reduce and transmission increases, as shown in Figure 5.2-1. It is noted that the transmission of the incident photons for both samples under the same conditions reached 40%.
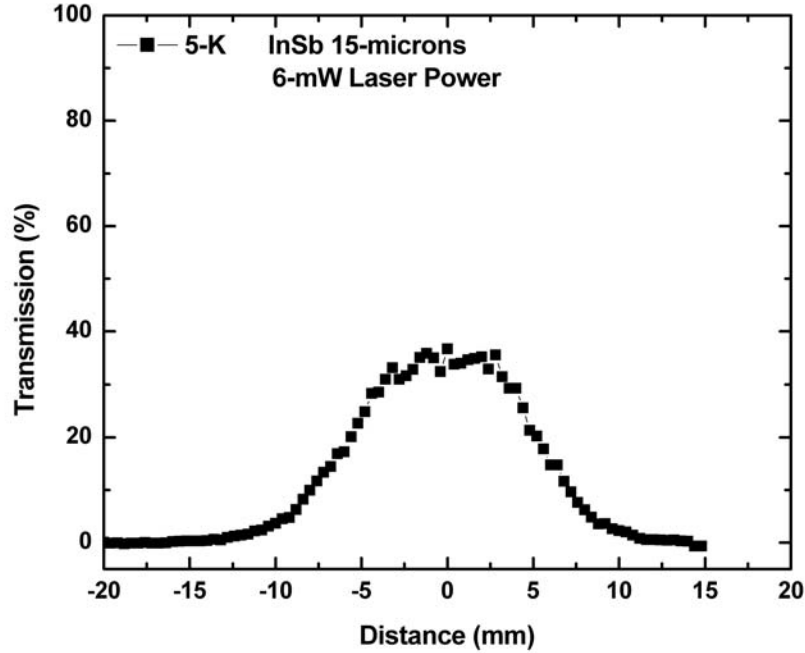
Figure 5.2-1. The 15-μm InSb sample experimental transmission data taken at 5 K. The focal point of the experiment is located at zero on the x-axis, where the irradiance is the highest.

Recalling that the data sets were collected in sequential order by temperature, the continuous run from 5 to 300 K shows that the peak saturation of the samples occurs between absolute zero and liquid nitrogen temperatures. This peak in saturation phenomena at liquid nitrogen temperatures presents a hazard to a normal working FPA where the device would have been cooled for operational use. For the 15-μm InSb sample, the peak saturation phenomenon occurred at 62.5 K, while the 30-μm InSb sample peaked at 22.5 K. The 15-μm InSb sample data for 5 K to 302.5 K is presented as 6 mW and 15.8 mW data sets, corresponding to the peak irradiances of $328 \dfrac{J}{s-cm^2}$ and $864 \dfrac{J}{s-cm^2}$, respectively (Figure 5.2-2). The 15-μm InSb sample data set (Figure 5.2-1),

which produced the 40 % transmission, was bleached at an irradiance of $328 \frac{J}{s-cm^2}$ at

5 K.
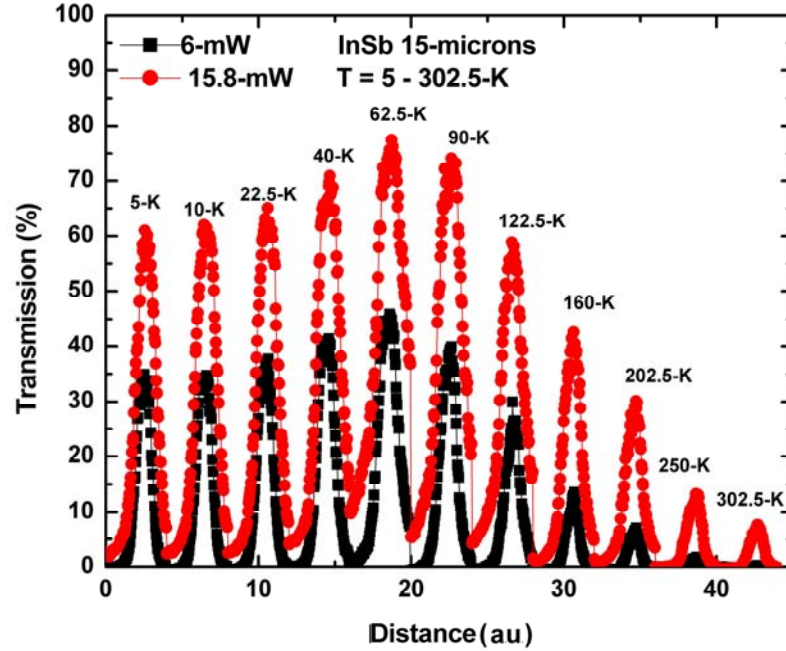
Figure 5.2-2. A continuous run of experimental transmission data taken for the 15-µm InSb sample. Eleven temperatures taken with a laser excitation powers of 6 mW and 15.8 mW are shown. Each peak was formed by passing through a focused laser, from low irradiance to high and then back again to low. Each peak occurs when the sample was located at the focal point having high irradiance as the sample bleaches it allows photons through.

The 30-µm InSb sample was also bleached at the same irradiance as the 15-µm InSb sample allowing 40% transmission. While the 15-µm InSb sample was bleached for all temperatures, the 30-µm InSb sample was bleached only from 5 K to 160 K at a peak irradiance of $328 \frac{J}{s-cm^2}$. Saturation for higher temperatures was achieved by increasing the peak irradiance on the 30-µm InSb sample to $5.85 \times 10^3 \frac{J}{s-cm^2}$ from 160 K to 302.5 K. For the 30-µm InSb sample at temperatures of 5 K to 302.5 K, the data is presented as

6 mW, 20 mW, and 107 mW, with 107 mW corresponding to $5.85 \times 10^3 \dfrac{J}{s-cm^2}$ (Figure

5.2-3). In Figure 5.2-3, the 160-K data set is artificially inflated from the InSb detector

being saturated. This occurred due to the high photon irradiance that was transmitted

through the sample. This irradiance level was higher than the dynamic range of the

detector; thus, an artificial result of 100% transmission was recorded. A more accurate

transmission level, assuming only the losses from the interfaces, from the 160-K data set

would have been at a maximum 75%.
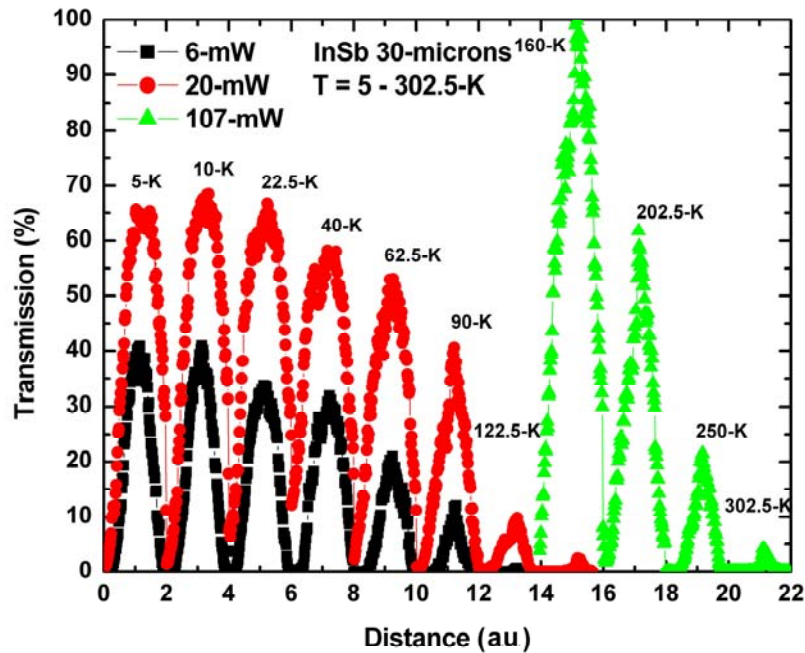
Figure 5.2-3. A continuous run of experimental transmission data taken for the 30-μm InSb sample. Represented are 11 temperature runs taken with a laser excitation powers of 6 mW, 20 mW, and 107 mW. Each peak was formed by passing through a focused laser, from low irradiance to high and then back again to low. Each peak occurs when the sample was located at the focal point having high irradiance. As the sample bleaches, it allows photons through.

The raw experimental data proves that absorption in the InSb can become

saturated. By allowing transmission of the high irradiance IR photons, instead of full

absorption of the photons as expected with low irradiance, the InSb material is bleached. This process is shown to occur with low laser powers provided the irradiance is focused onto the material. An example of this description is any FPA detector system using telescopic optics.

5.3 Transmission and Irradiance

A more intuitive method of examining the data is to view it as irradiance versus transmission. If one laser excitation power generates an irradiance on the z-axis at a specific location, another laser excitation power will generate the same irradiance on the z-axis, but shifted depending on the change in excitation power. This allows the different laser excitation powers to be examined on the same plot.

For the 15-μm InSb sample, the peak saturation absorption occurred at 62.5 K, as shown in Figure 5.3-1, where the 62.5-K data curve is the highest. Bleaching of the sample begins at an irradiance of just $25 \dfrac{J}{s-cm^2}$.

The 30-μm InSb sample, when investigated by transmission versus irradiance, shows that the sample began to saturate at an irradiance of just $25 \dfrac{J}{s-cm^2}$ (Figure 5.3-2). As the sample is saturated, the transmission increases to a point where it no longer increases and flattens off at $250 \dfrac{J}{s-cm^2}$. The peak transmission took place at 5 K for an irradiance of $328 \dfrac{J}{s-cm^2}$.
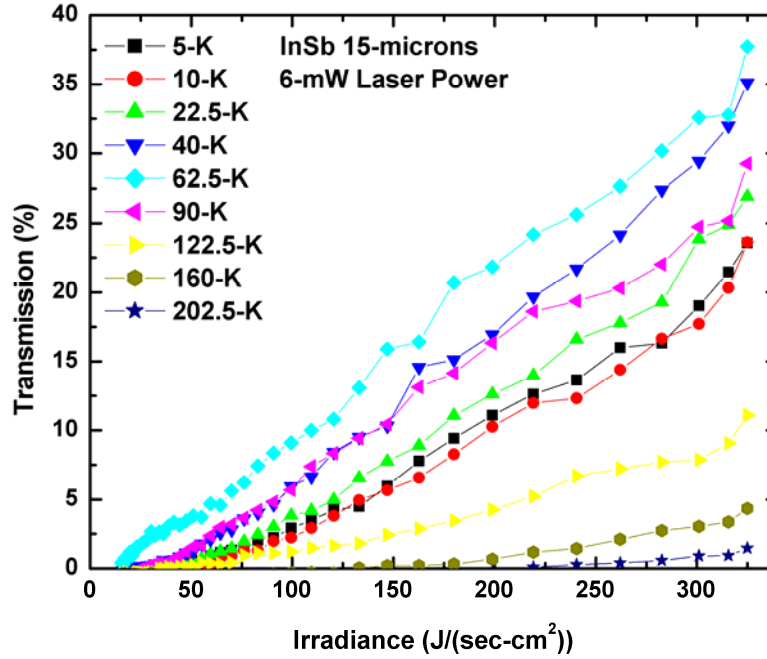
Figure 5.3-1. The 15-µm thick InSb sample experimental transmission data for 5 K to 202.5 K as a function of transmission versus irradiance incident on the sample. As the irradiance increases, the sample saturates with carriers and allows more photons through.

The 30 µm InSb sample was not saturable for the temperatures of 160 to 302.5 K with low irradiances. This occurred because the sample is thicker, giving more material allows more photons to be absorbed before the energy bands are saturated. The difference found in the transmission may be due to the difference in the E_g, from one temperature to the next. Recall that E_g is temperature dependent. Also, recall that E_{DEOS} = 0.269 eV, and at cold temperatures, $E_g(5 \text{ K}) = 0.239$ eV, so that $hv = \dfrac{0.269eV}{0.239eV} E_g =$ 112.5% E_g. This means that the laser is exciting 112.5% into E_g, where 100% would be at the band edge. Then for a warmer temperature, $E_g(160 \text{ K}) \sim 0.216$ eV, so that $hv = \dfrac{0.269eV}{0.216eV} E_g = 124.5\% E_g$. The density of states in the material is greater deeper into the

85

energy bands. Therefore, it will take more photogenerated carriers to fill the bands at higher temperatures. A higher irradiance was needed to induce the absorption-saturation phenomenon for the temperatures of 160 K to 302.5 K. Saturation for the higher temperatures began to occur at an irradiance of $1200\dfrac{J}{s-cm^2}$ (Figure 5.3-3).
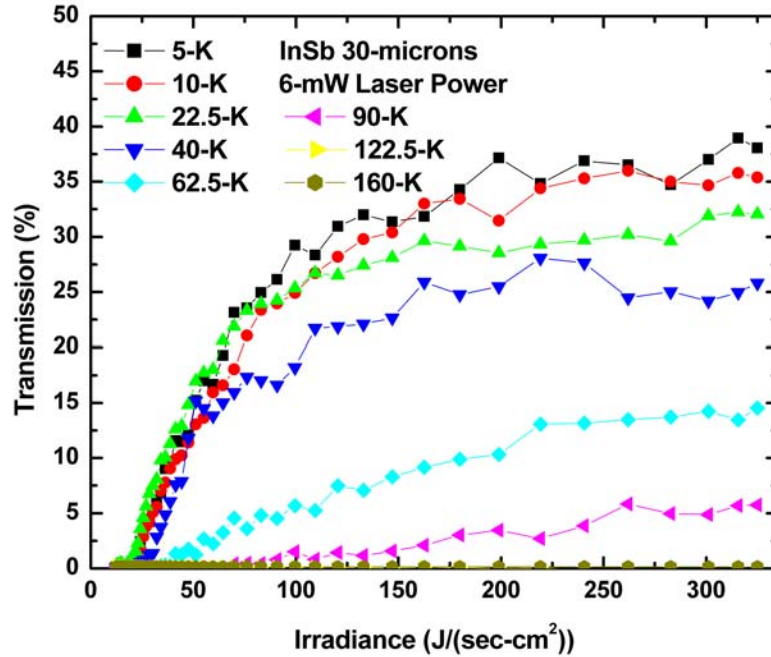
Figure 5.3-2. The 30-µm thick InSb sample experimental transmission data, from 5 to 160 K as a function of percent transmission versus irradiance incident on the sample.   The average laser excitation power is 6-mW.

The sample was not investigated at lower temperatures with the higher irradiance, because the sample would have been completely bleached, allowing the high irradiance to strike the detector which would cause either error in the data or damage to the instrument. Note that the data shown in Figure 5.3-3 has a higher transmission than Figure 5.3-2; this is because the sample had not been fully saturated in Figure 5.3-2. The sample is beginning to be completely saturated in Figure 5.3-3, but the material is still

absorbing photons at the peak irradiance. A higher irradiance would be needed to fully saturate the material.
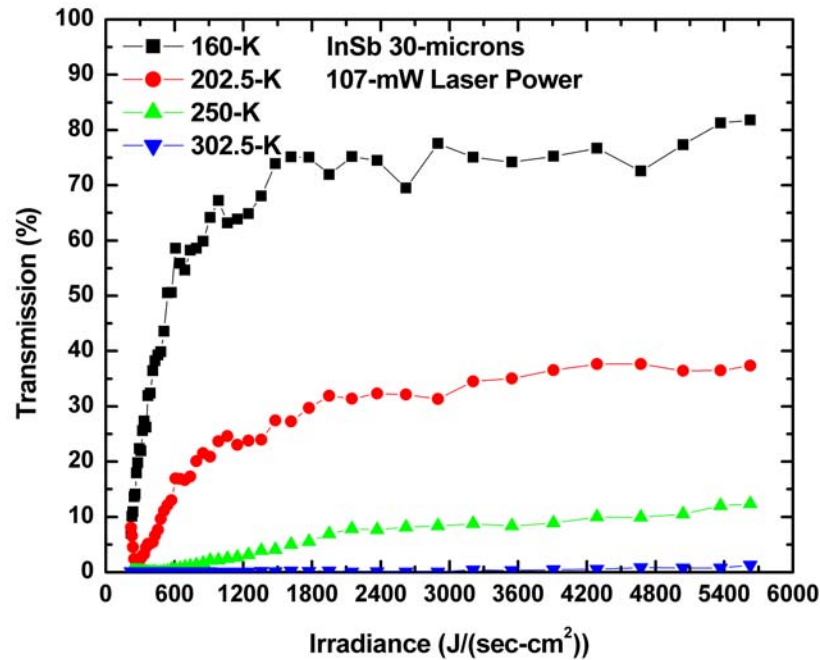
Figure 5.3-3. The 30-µm thick InSb sample experimental transmission data from 160 K to 302.5 K as a function of transmission versus irradiance incident on the sample. Note that the data taken here is only used to prove that at 302.5 K, some absorption saturation can be attained with higher photon irradiances. The average laser excitation power is 107-mW.

Plotting transmission versus irradiance shows that there is good validity in the experimental data sets. The excitation powers of 15 mW and 20 mW incident on the 30-µm InSb sample shown in Figure 5.3-4 where the two data sets are overlaid for comparison, shows that the only large dissimilarity is the first set in black for 4.99 K and 6.02 K. This difference in the two data sets is attributed to the change in lattice temperature of the material and no other physical phenomenon. The rest of the data sets presented show that the experimental data taken for the two different excitation powers are nearly identical. The error that is observed in Figure 5.3-4 is attributed to the DEOS laser output power fluctuating as a function of time. An adjustment to the data sets was

not performed for the laser excitation output power varying, and only raw data is presented. The DEOS laser output power fluctuation was noted in Chapter 3.
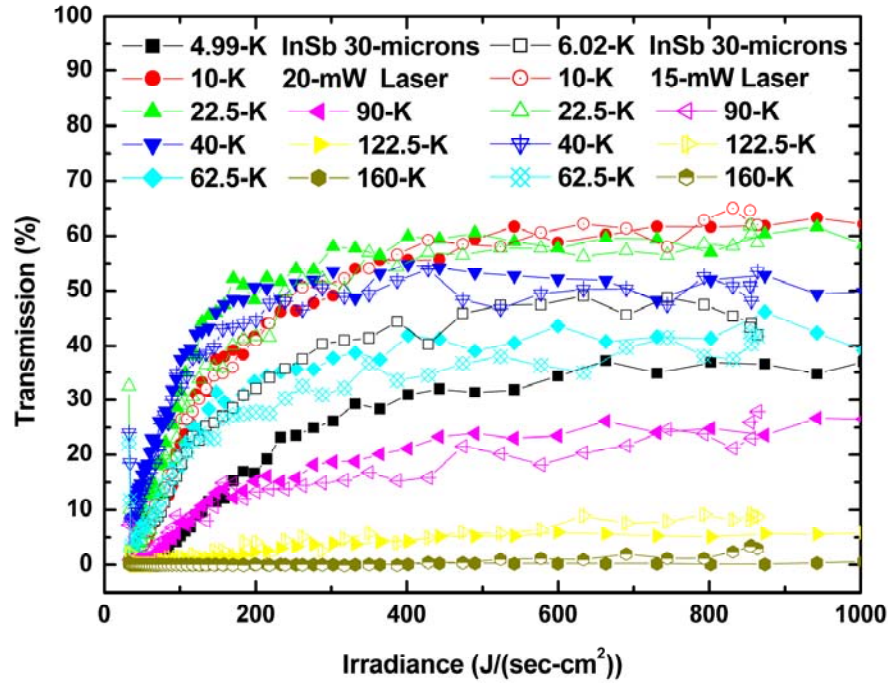
Figure 5.3-4. A comparison between the two experimental transmission data sets taken at 20 mW and 15 mW for the 30-μm thick InSb sample, from 5 K to 160 K as a function of transmission versus photon irradiance incident on the sample. Note that the peak saturation effect takes place at 10 K.

5.4 Conclusion to Experimental Data and Results

From the experimental data results presented, it is evident that InSb up to 30-μm thick can be bleached with relatively low laser output powers. It should be noted that these results have been reproduced in three separate experiments. The first experiment on the material was performed in 2006, where the sample was manually translated through the focal point. The second experiment was performed in late 2007, where the sample was also manually translated through the focal point of the experimental apparatus discussed herein. Finally, the third experiment was performed early in 2008 for this research effort with the automated feature allowing for high resolution data.

6   Modeled Data and Results

The progress made to the model includes different assumptions and alterations that are stated within the chapter at the beginning of each section that pertains to the advances made. Note that Chapter 4 explained only the characteristic model in which the sample is treated as a single unit, with uniform irradiance.   Recall, that the model used a mathematically incorrect expression for Δn and Δp that introduced some error into the generated data. Without this simplified form, it would not have been feasible to model the experimental data with current machine computational capability. The expressions used for Δn and Δp allow the model to be run in a more reasonable time frame. However, the data presented from the model contains a certain amount of error introduced from these expressions. The difference from the actual equations to them will be discussed in Section 6.1.5. Each alteration made to the model builds upon the previous. Then, the generated results from the models are presented. Each section in the chapter represents a subsequent alteration to the model and builds upon the last. The goal is to accurately model the carrier density and carrier lifetime within the bleached samples as stated in Chapter 1.

6.1   Carrier Density and Lifetime

Results from the model were generated by selecting a carrier lifetime that produced values for the quasi-Fermi energy levels appropriate for the number of generated carriers, which were used in Equation (4.43) to plot the transmission (Figure 6.1-1). Each iteration number in Figure 6.1-1 represents a unique irradiance level, where the focal point of the experiment is located at the 50th iteration. The model's results were

overlaid with the experimental transmission data for each irradiance intensity along the z-axis, as shown in Figure 6.1-1. The experimental data is shown in blue and the generated data points are shown in purple. Each iteration number has a unique carrier lifetime, τ, associated to it. This process of selecting τ was completed for each of the six models. Each model assumes that the crystal lattice is held at a constant 62.5 K, and that the peak irradiance found at the focal point is $325 \dfrac{J}{s - cm^2}$.
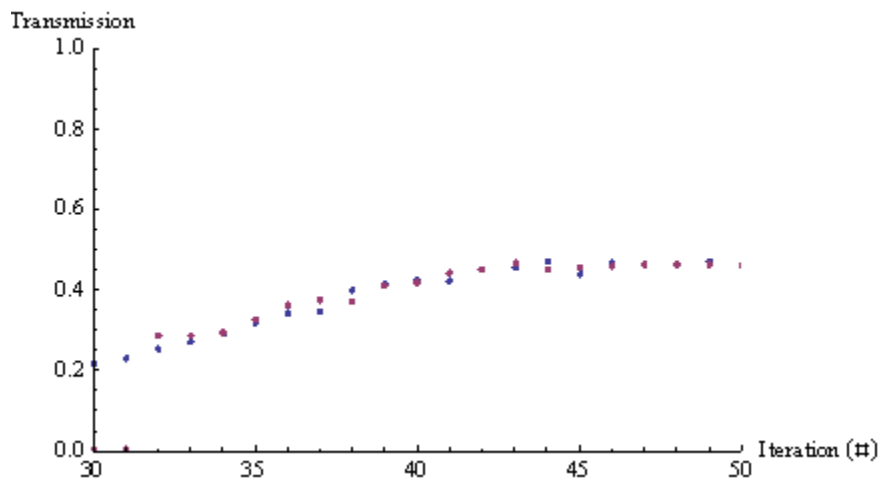
Figure 6.1-1. The experimental transmission data is shown in blue and the modeled transmission data is shown in purple. The fitted data was found by iterating τ until the data sets were aligned. Each iteration number corresponds to a unique irradiance value, where the 50th iteration is at the focal point. On the y-axis one is equal to 100% transmission.

6.1.1 Single Block

In this model, the sample is interrogated as a single block 15-μm and 30-μm thick, and the irradiance incident on the sample is assumed to be a uniform distribution. The results from the model give rise to the carrier lifetime, τ, and the total number of carriers, N. Recall that τ is a function of the N and T, where T = 62.5 K. Note that N varies at each iteration point with the increase in irradiance. As N increases, τ decreases and appears to follow a general trend of a Bradley function for all the models investigated as

90

shown in Figures 6.1-2 and 6.1-3, for the 15- and 30-μm InSb samples, respectively. The

predicted τ's range from 9-20 ns at the focal point (peak irradiance). Values for τ are

presented versus N for the 15- to 30-μm InSb samples as shown in Figures 6.1-2 and 6.1-

3, respectively. The changes in N and τ are noted to increase only slightly under the same

irradiance levels and temperature conditions between the two samples. The data

presented in both Figures 6.1-2 and 6.1-3 are truncated results where only the bleached

portion of the data is presented. Data for the unbleached portion of the sample was not

calculated.
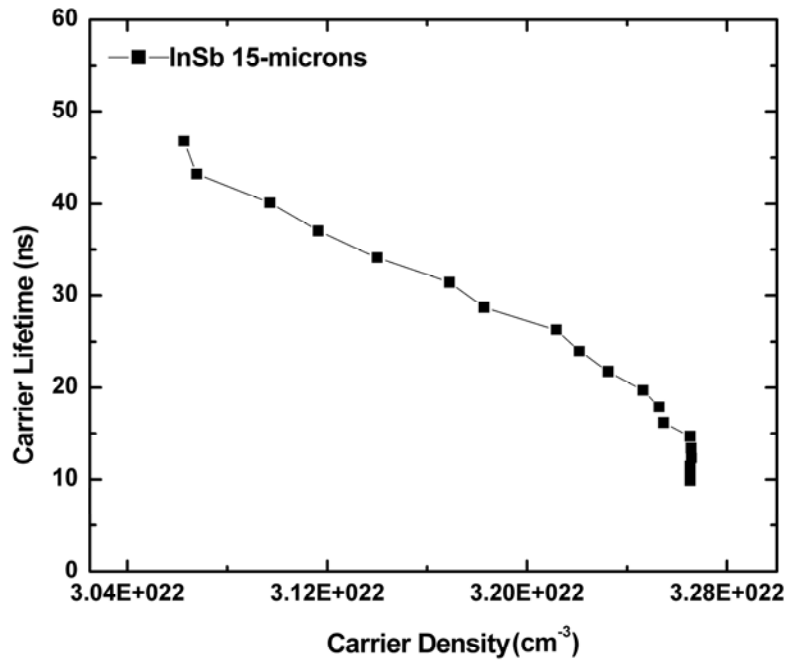
Figure 6.1-2. Shown is the carrier lifetime as a function of carrier density for the 15-μm InSb sample, (from left to right the sample at low irradiance moving to higher irradiance). The carrier lifetime decreases as the density of carriers increases. The peak density of carriers, when saturated, is 3.26×10^{22} cm^{-3}.

91
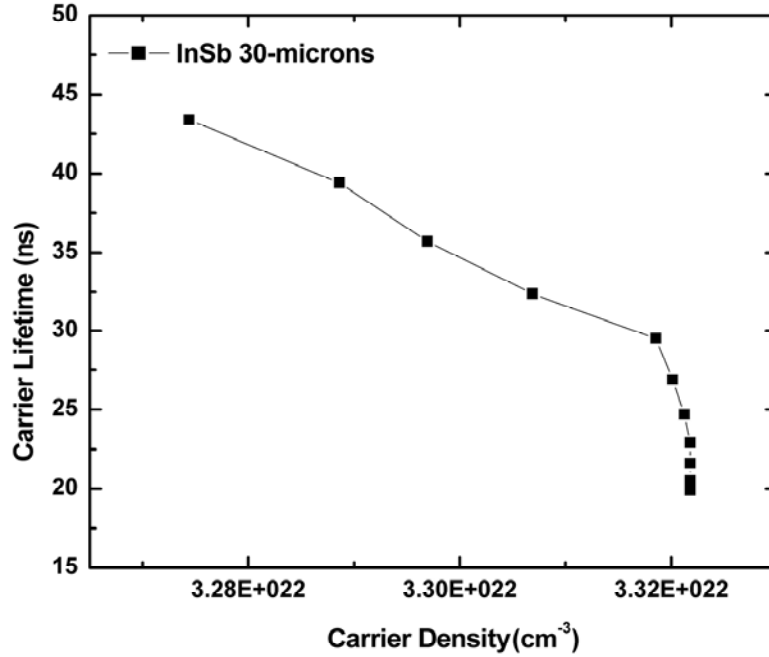
Figure 6.1-3. Shown is the carrier lifetime as a function of carrier density for the 30-μm InSb sample. The peak density of carriers when saturated is 3.32×10^{22} cm^{-3}.

The irradiance versus τ shown in Figure 6.1-4 shows the difference in τ for the two samples under the same irradiance conditions. In general, what is observed from the model is that as the irradiance increases, the number of carriers excited also increases due to absorption of the photons by the electrons; as more carriers are excited and the sample begins to saturate, τ starts to decrease. When the sample is completely bleached from saturable absorption, the model predicts that τ will be 9 ns for the 15-μm InSb sample and 19 ns for the 30-μm InSb sample, where the predicted carrier lifetimes occur at an irradiance of $325 \dfrac{J}{s-cm^2}$. The model predicts that when the sample is absorbing all of the incident irradiance and no transmission occurs, *ie.* not bleached, it will have a correspondingly longer carrier lifetime up to 250 ns. It should be noted here that the transcendental nature of τ in the model was designed for the bleached regime. Since the

laser pulse width is 92 ns, and even though the pulse repetition time is 683 ns, model

results for τ greater than ~90 ns are not considered valid.
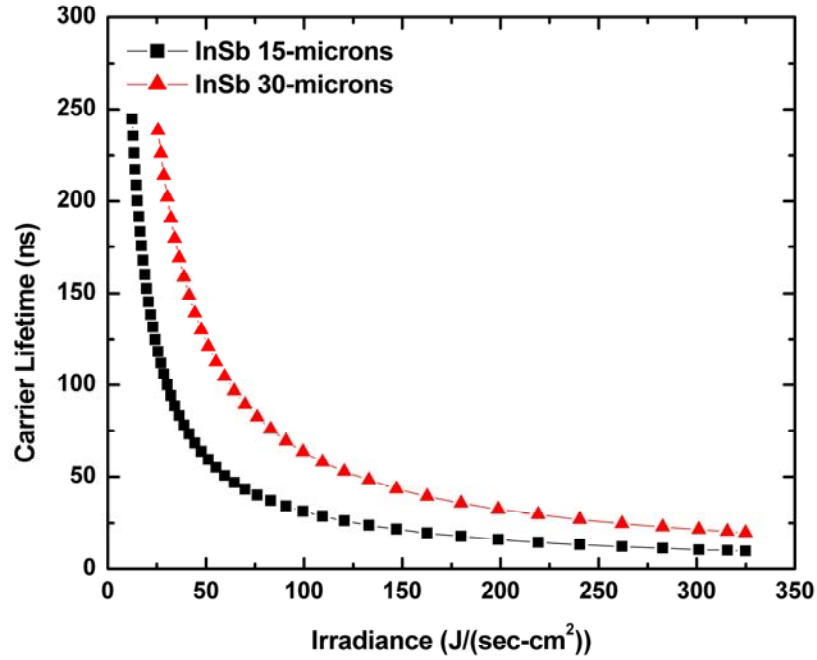
Figure 6.1-4. Shown is the carrier lifetime as a function of irradiance on the 15- and 30-μm InSb samples.

The carrier lifetime versus irradiance figures are important to the modeling

process. These figures are provided to show that the closer τ *vs*. E_e (where E_e is the

irradiance) is to converging, the closer τ vs. N will be to converging. In the model, it is

easier to produce τ *vs*. E_e to see how close the data set is to converging, before producing

τ vs. N, which takes a great deal more time to generate.

6.1.2 Dual-Irradiance Pattern

The difference found between the two samples may have been caused from the

assumptions used in the original single block model, where the irradiance incident on the

sample was assumed to be uniform. An effort to correct for this error introduced three variations of the model. In the original model, the laser irradiance on the sample was assumed to be a uniform spot, but realistically the laser irradiance on target produces a Gaussian distribution. This causes the center of the irradiance pattern on the sample to bleach first because the power per unit area is higher there. After the center of the sample bleaches, the surrounding area would begin to bleach as the irradiance increases during the sample translation into the focal point. A Gaussian function was not used in the model to correct for the error due to the large number of iterations that would have been needed to produce a smooth data set. Instead, the irradiated spot on the sample was considered in separate circular sections that follow a Gaussian function's average distribution over the section (Figure 6.1-5).

The irradiance pattern was formed by consecutive circles forming a bulls-eye, where the center of the bulls-eye was investigated at several different radii from 5 μm to 40 μm. As the number of circles increased in the bulls-eye, no notable change was observed in the data for the generated number of carriers, or carrier lifetime, past two consecutive circles. In this pattern, only the center circle and an outlaying ring are considered in the model (Figure 6.1-5). The center was assumed to have a diameter measured from the full width half max (FWHM) of the Gaussian function, and the ring in the irradiance patterns diameter was measured from the FWHM to $\frac{1}{e^2}$. Consider that the center of the irradiance pattern is Part-A and that the ring is Part-B.

Having two separate irradiances also resulted in the need for splitting the excitation power appropriately between the two, where Part-A was excited by 4.23 mW and Part-B by 2.27 mW. The division between the two areas assumed that the average

laser output power was 6.5 mW, and that 65% percent of the power was selected to be in Part-A, while 35% of the power was selected to be in Part-B. These two separate excitation powers give rise to two sets of irradiances on the sample, giving a more realistic view of the results. The τ for Part-A was selected manually, while τ for Part-B was related to Part-A by an equation. The equation that relates the two τ will be presented with the data sets.
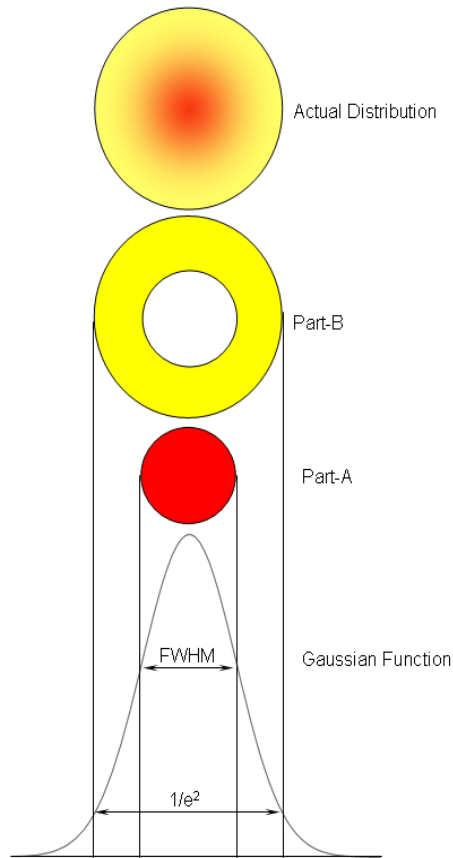
Figure 6.1-5. The Gaussian distribution function applied to the dual irradiance pattern, where the outer ring Part-B has less intensity than that of the center Part-A. Note that the actual irradiance distribution is shown on top. A Gaussian function (below) is divided to show the two separate irradiance patterns used in the model, where Part-A has a diameter equal to the full width at half max of the Gaussian function and Part-B has a diameter equal to $1/e^2$. The actual distribution of the Gaussian function is shown on the bottom.

In the first attempt of the dual-irradiance model, τ was assumed to be a fraction, where 35% was attributed to Part-A and 65% was attributed to Part-B. The fraction used

was assumed from the incident irradiance fraction for the dual-irradiance. Having the model run in this way allowed for a single value for τ to be selected. This then allowed for easy manipulation to achieve the correct generated transmission data matching the experimental data. The data presented in both Figures 6.1-6 and 6.1-7 are truncated results where only the portion of the data presented is where the sample had been bleached. Data for the unbleached portion of the sample was not calculated. The density of carriers found in both the irradiated sections of the sample for the 15-μm InSb sample are less than the density of carriers found in the 30-μm InSb sample. This is expected due to the increased thickness of the sample; having more material naturally allows there to be more carriers present. The reason for the difference in carrier density between the two samples is that more photons can be absorbed in a thick sample before transmission occurs. However, this increased thickness lowers the transmission.

Interestingly, the irradiance versus τ plot (Figure 6.1-7) shows that, when using the ring irradiance pattern for the 15 μm InSb sample, the two irradiated areas produce values for τ where the difference is only 5 ns between the two irradiance patterns. Having the two values of τ for Part-A and –B closely related suggest that the realistic value of τ is close to these values. For the 30-μm InSb sample, τ is once again greater than the 15-μm InSb sample's data. The irradiance data for both samples' Part-B do not continue down to lower carrier lifetimes. This is due to the low irradiance levels that reach Part-B, which follows the same general trends that were observed in the original model, low irradiance causes τ to be high.
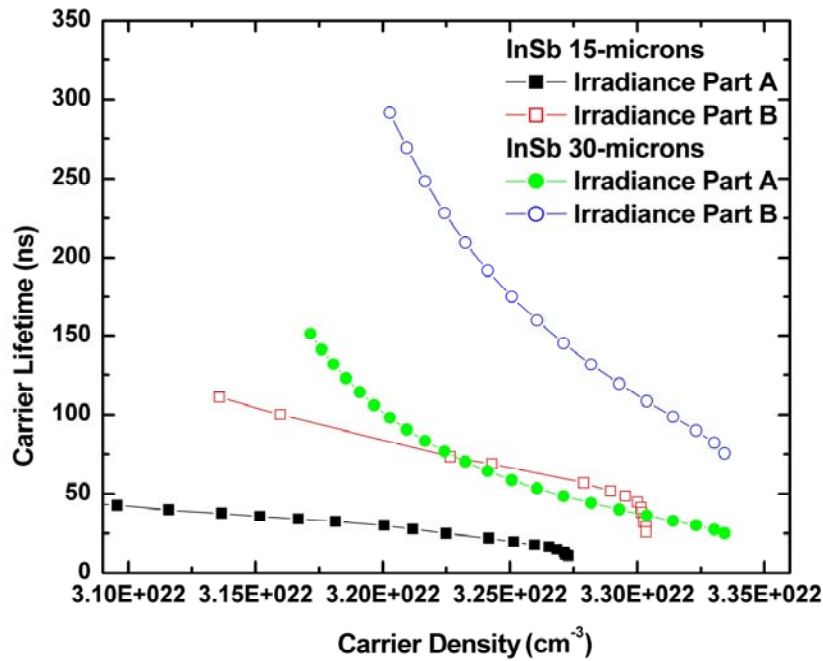
Figure 6.1-6. The carrier lifetime for the 15- and 30-μm InSb samples versus the carrier density. A bulls-eye irradiance pattern is used in the model where the center is Part-A and the outside ring is Part-B. The peak density of carriers when saturated for the 15-μm InSb sample Parts-A and –B are 3.27×10^{22} cm^{-3} and 3.30×10^{22} cm^{-3}, respectively. For the 30-μm InSb sample, Parts-A and –B are 3.33×10^{22} cm^{-3} and 3.33×10^{22} cm^{-3}, respectively.

Having the two samples' data sets for the two separate irradiated segments for the irradiance versus carrier lifetime (Figure 6.1-7) separated suggests that the model is flawed. It was expected that the two parts would have been more closely related. However, having an unknown exitance from the sample, and not being able to accurately predict it, leads to errors. An attempt to correct for this error leads to altering the relationship between Parts-A and -B's carrier lifetimes, in an effort to allow the two parts' data sets to overlay each other. It is expected that the N would be the same for the same τ regardless of all other factors. For this reason, the N versus τ for Parts-A and –B should be identical.
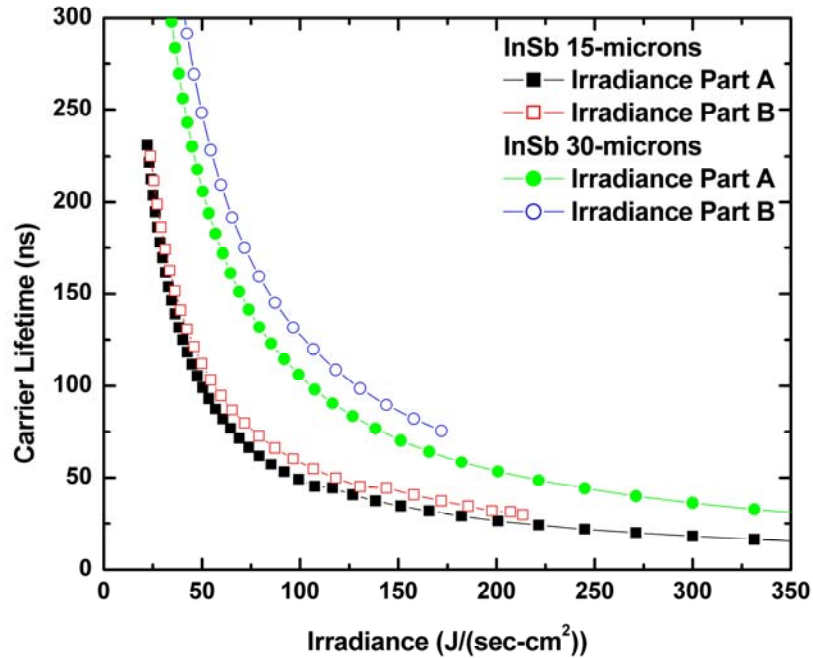
Figure 6.1-7. The carrier lifetime of the 15- and 30-μm InSb samples versus the irradiance on the samples. A bulls-eye (ring) irradiance pattern is used in the model where the center is Part-A and the outside ring is Part-B.

A second run of the model produced better results that showed promise. These results were generated by carefully selecting realistic values for τ once a general trend was observed by running subsequent iterations of the model shown in Figure 6.1-8. Having the two irradiance area's results closer to converging is what is desired. From Figure 6.1-6 to Figure 6.1-8, it can be observed that the two data sets in the second figure are, in fact, closer to converging than the first.
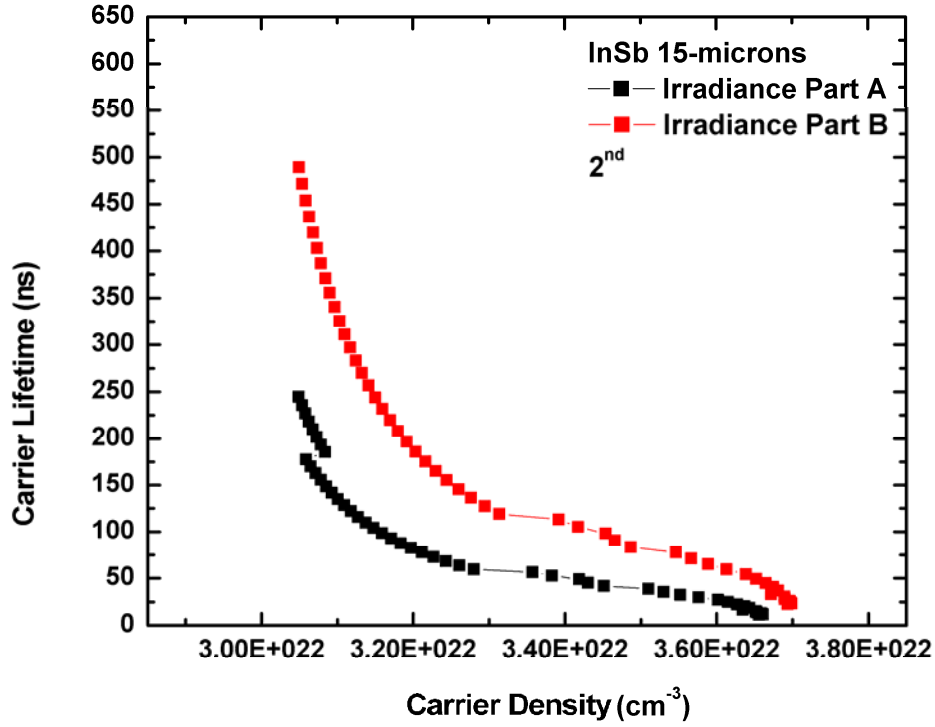
Figure 6.1-8. The second attempt at running the dual-irradiance model.

A third attempt at the model related the two τ's with a simple equation given as

$$\tau_B = \tau_A 1.25 + z 0.4 \qquad\qquad (6.1)$$

where τ_B is the carrier lifetime found in Part-B, τ_A is the carrier lifetime that was manually

selected in Part-A, and z is the iteration number. The results using Equation (6.1) are

shown in Figure 6.1-9. Several different alterations of Equation (6.1) were tried, where

the constants were varied in an attempt to converge the two data sets presented in Figure

6.1-9. Unfortunately, this is the closest the two data sets came to converging.

Further attempts at improving the model did not produce superior results. These

attempts included several more equations relating the two τ's, and are given as,

$$\tau_B = z 2.05 , \qquad\qquad (6.2)$$

$$\tau_B = \tau_A 1.75 + z 0.5 \qquad\qquad (6.3)$$

99

and

$$\tau_B = A + Bz + Cz^2 \tag{6.4}$$

where *A, B,* and *C* are constants that follow from knowing τ versus the iteration number, where $A \sim 270$, $B \sim -10.58$, and $C \sim 0.10373$.
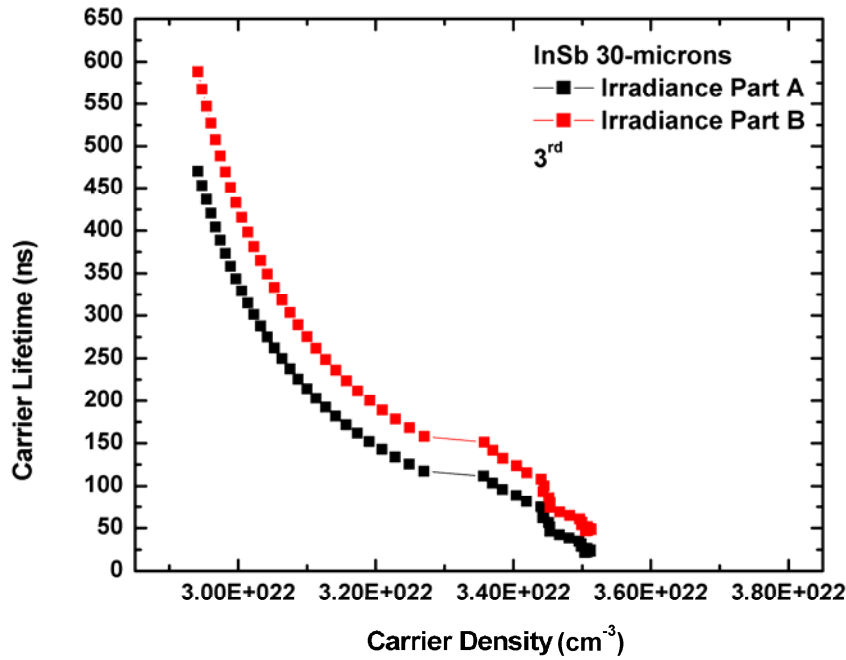
Figure 6.1-9. The third attempt at running the dual-irradiance model.

It was assumed that attempting to generate data with Equation (6.4) would have yielded better results. This belief came about from Chapter 4 where the previous data sets were generated by selecting a handful of τ and using a polynomial fit to generate the rest, dependent on the iteration number. Instead, the data set that was generated from Equation (6.4) appears to fall apart. From this point, it would appear that no amount of tweaking will cause the two data sets to converge. For this reason, another step is taken to increase the fidelity of the model, bisecting the sample.

6.1.3 Bisected Sample

A variation of the block model has taken into account the sample thickness. In this model, the irradiance on the sample is once again considered to be a uniform distribution. Instead of assuming that the 30-μm InSb sample was one piece, as in the original model, it was separated in two 15-μm sections. The first section absorbed some of the incident photons and the next segment was irradiated by the transmitted exitance from the first. The sample was not segmented farther than bisection because there would have been no reference point for the smaller thicknesses. The results produced from bisecting the 30-μm InSb were compared to the 15-μm InSb samples transmission data. It was assumed that the first half of the bisected 30-μm InSb sample would have a comparable transmission to that of the 15-μm InSb sample.

The 30-μm InSb sample, when bisected, presented an N that is greater than the rest of the modeled data (Figure 6.1-10), but is still closely related to the rest of the modeled results. This increase in carrier density is attributed to the model's ability to accurately account for the generated carriers found in the two sample sections. The data shown is truncated where only the bleached portion of the data is presented. Data for the unbleached portion of the sample was not calculated.

The 30-μm InSb sample, when bisected, generates an irradiance versus carrier lifetime that closely follows that of the 15 μm InSb sample original block model (Figure 6.1-11). At the peak irradiance of $328\frac{J}{s-cm^2}$, the carrier lifetime was 10.2 ns for the bisected model while the original model yielded $\tau = 9$ ns. The error between the two data sets is only 2.5 ns, when calculated as a running average.
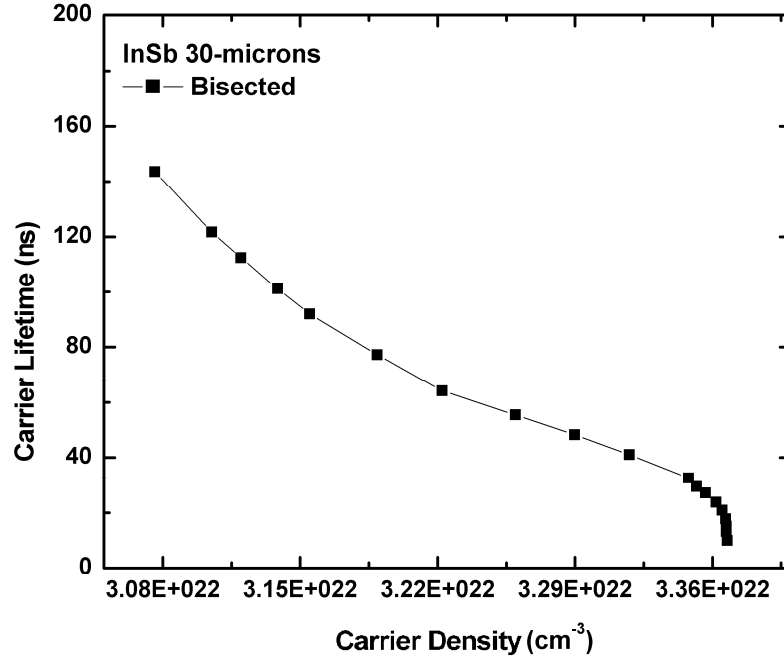
Figure 6.1-10. **The carrier lifetime of the 30-μm InSb sample versus the carrier density, while being bisected. The peak density of carriers when saturated for the 30-μm InSb bisected sample is $3.36 \times 10^{22} cm^{-3}$.**

After finding consistent results between two of the models for the two sample thicknesses, a correlation can be made for the carrier lifetime of the sample. While the sample is being bleached at $328 \frac{J}{s-cm^2}$, the carrier lifetime can be estimated to be 10 ns from the relationship between the two models. The model is still not realistic as it does not account for the change in irradiance across the sample's surface during bleaching. Attempting to account for both the irradiance and sample thickness leads to a combination between the dual-irradiance pattern and the bisected models (Section 6.4.1).
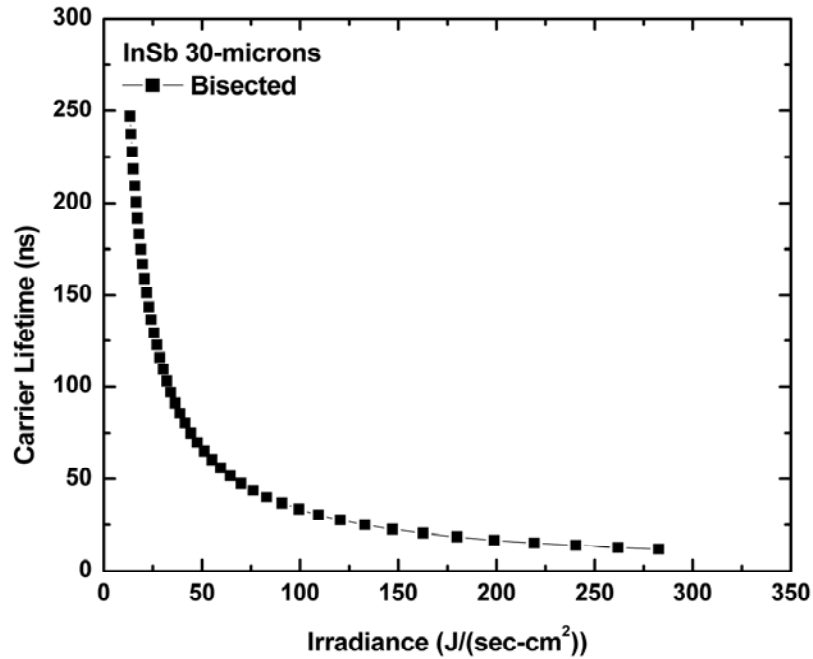
Figure 6.1-11. **The carrier lifetime of the 30 μm InSb sample versus the irradiance, while being bisected.**

6.1.4 Dual-Irradiance Bisected

The dual-irradiance bisected model solves for four separate sections of the 30-μm InSb sample. There is the front and the back half of the sample that takes into account the bisection. Within each bisected area, the ring irradiance pattern is used, which leads to two more sections of the sample: the center and outlaying region of the ring (Figure 6.1-5). In turn, the data is presented in these four separate sets which corresponds to the four divisions. Shown in Figure 6.1-12 is the carrier density versus the carrier lifetime of the 30-μm InSb sample for the first part of the bisected sample with the two separate irradiance regions, where 30 EP-A Bi-1 is the center of the bulls-eye and 30 EP-B Bi-1 is the outlaying ring of the irradiance pattern. The data set presented contains the full range from no saturation to full saturation, left to right, respectively, and the full data set has

103

been calculated for an irradiance of $0\dfrac{J}{s-cm^2}$ to $328.964\dfrac{J}{s-cm^2}$. The density of carriers

found in the first section of the sample is close to that of the previous models.
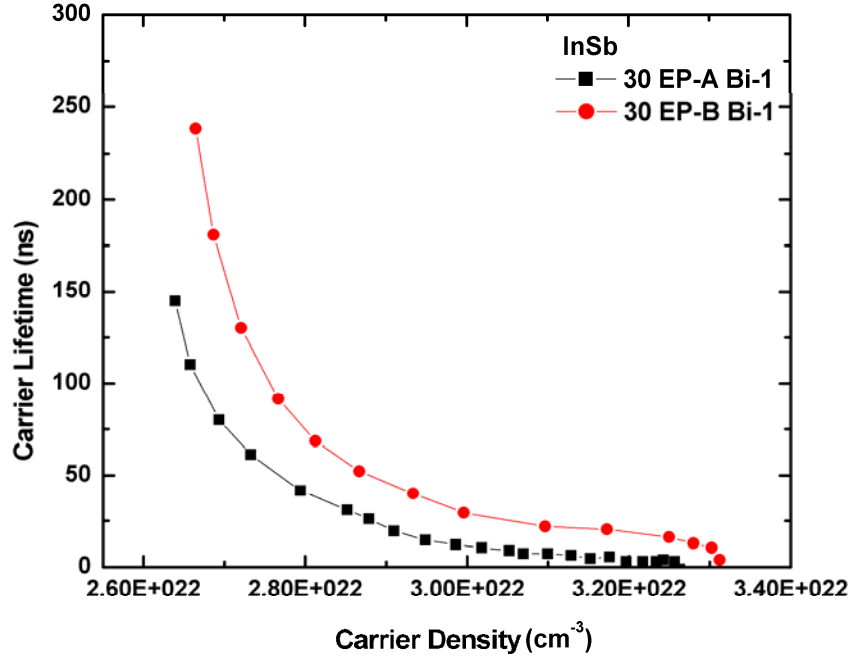
Figure 6.1-12. The carrier lifetime of the 30 μm InSb sample versus the carrier density. A bulls-eye irradiance pattern is used in the model along with bisecting the sample, where the irradiance pattern's center is EP-A and the outside ring is EP-B, and the first half of the bisected sample is presented Bi-1. The peak density of carriers, when saturated, for the 30-μm bisected InSb sample, first half, Parts-A and –B are 3.26×10^{22} cm^{-3} and 3.31×10^{22} cm^{-3}, respectively.

The carrier densities for the second half of the bisected sample are presented in

Figure 6.1-13, where the values predicted by the model are about half the value given by

the other models. It was expected that the results for the density of carriers in the

material from the 2nd part of the bisected sample would be less than the first due to the

irradiance being less than what was incident on the first half. As the irradiance is

decreased, the carrier lifetimes increases, and in turn, the density of carriers in the

material decreases. As discussed earlier, the irradiance in the outlaying ring is less than

that in the center portion. Thus, it is expected that the density of carriers would be greater in the center than in the outer ring. This is exactly what the model predicts (Figures 6.1-15 and 6.1-16), where the irradiance is high, the carrier lifetime is short, and the density of carriers is the largest. The same argument applies for the first part of the bisected sample shown in Figure 6.1-12.
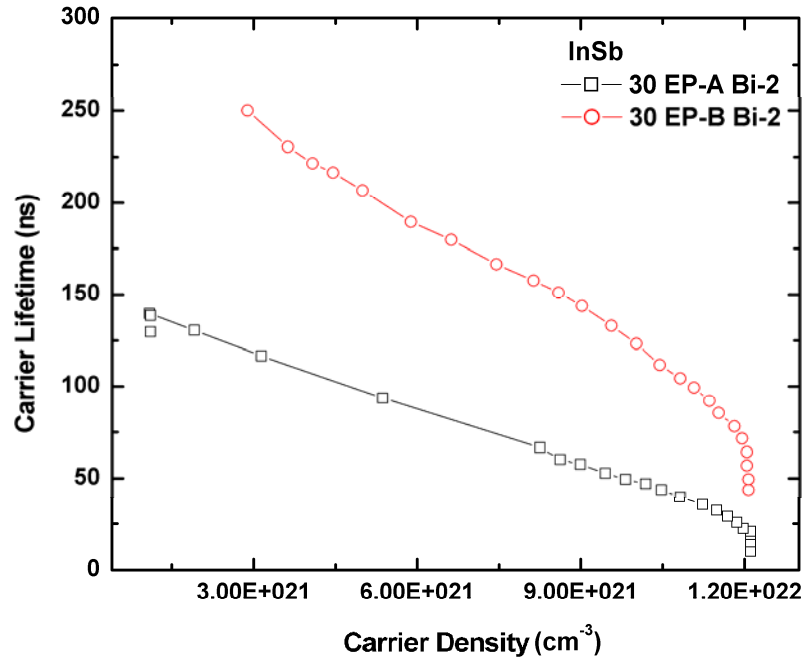

Figure 6.1-13. The carrier lifetime of the 30-μm InSb sample, versus the carrier density. A bulls-eye irradiance pattern is used in the model along with bisecting the sample, where the irradiance pattern's center is EP-A and the outside ring is EP-B, and the second half of the bisected sample is Bi-2. The peak density of carriers when saturated for the 30-μm bisected InSb sample, second half, Parts-A and –B are 1.20×10^{22} cm^{-3} and 1.21×10^{22} cm^{-3}, respectively.

The irradiance versus the carrier lifetime for the four parts is shown in Figure 6.1-14. Results from the first section of the bisected sample behave as expected, and follow the general trend of the previous model's results, where the low irradiance area has a longer carrier lifetime than the high irradiance portion, which has a shorter carrier lifetime. However, the results from the second section of the bisected sample for the

irradiance versus carrier lifetime were a surprise. The two irradiance area's data sets overlap in the second section of the bisected sample. It was expected that the results would have been similar to that of the first piece of the bisected sample, where the data sets do not overlap. Having little error between the two data sets for the irradiance suggest that in the second half of the bisected sample the dual irradiance patterns may predict a carrier lifetime that is more realistic than the previous models.
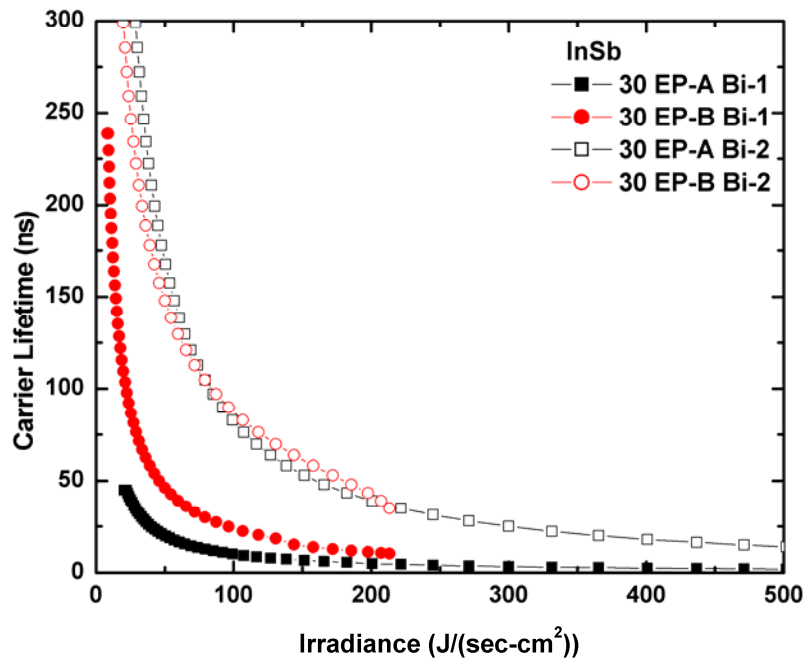
Figure 6.1-14. The carrier lifetime of the 30-μm InSb sample versus the irradiance.

The results predicted by the dual-irradiance bisected model show promise. Having not changed compared to the general trend of the other models, it may be tweaked so that all four pieces overlap. The 15-μm InSb sample was not bisected again for the same reasons stated before; there would have been no reference point for the 7.5-μm thick sample's transmission data. Without the transmission data set there is no scientific way to model the carrier lifetimes.

6.1.5 Comparison of Models' Results

Comparing the models by E_e versus τ in Figure 6.1-15 shows that the carrier lifetimes that the models predicted, in general, indicate that the carrier lifetime follows the general trend of decreasing lifetime with increasing irradiance. The results predicted by the models at a peak irradiance of $328 \dfrac{J}{s-cm^2}$, where the sample is bleached, the longest carrier lifetime predicted by the models is 33 ns and the shortest is 3 ns. In Table 6.1-1, a complete list of carrier lifetimes is given for the six models, where the sample is at the peak irradiance, and the average carrier lifetime for all the models is 16.8 ns at $328 \dfrac{J}{s-cm^2}$. Note that τ is a function of N, and the τ's that are reported in Table 6.1-1 are only for a single value for N, which is also reported in the table.

A comparison of the six models' carrier densities versus carrier lifetimes are presented in Figure 6.1-16 where the bisected model generated the largest number of carriers, $N = 3.36 \times 10^{22}$ cm^{-3}, at the longest τ. The 15-µm InSb and the 15-µm InSb Part-A are nearly identical due to the irradiance on the sample being almost identical. All of the models investigated produce results that are extremely close in orders of magnitude, except those predicted for the dual-irradiance bisected model's second half of the bisected sample. The carrier densities in the second portion of the sample are predicted to be 1.20×10^{22} cm^{-3} and 1.21×10^{22} cm^{-3} for Parts-A and –B, respectively. The carrier density, N, is listed for all six models in Table 6.1-1.

107
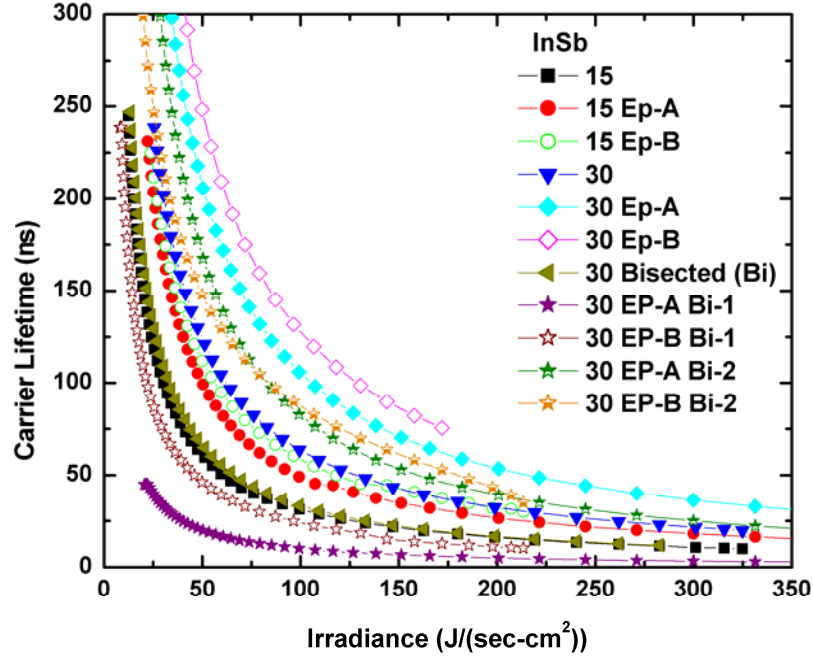
Figure 6.1-15. A comparison for all six models' results of the carrier lifetime on the 15- and 30-μm InSb samples versus the irradiance. The models are (1) 15 (single Block model for the 15-μm InSb sample), (2) 15 Ep-A, 15 Ep-B (Dual-irradiance pattern model for the 15-μm InSb sample) (3) 30 (single Block model for the 30-μm InSb sample), (4) 30 Ep-A, 30 Ep-B (Dual-irradiance pattern model for the 30-μm InSb sample), (5) 30 Bisected (Bisected model for the 30-μm InSb sample), (6) 30 EP-A Bi-1, 30 EP-B Bi-1, 30 EP-A Bi-2, 30 EP-B Bi-2 (Dual-irradiance pattern and bisected model for the 30-μm InSb sample).

Now that the data has been presented, the error that was introduced in the model can be discussed. The errors used in the model are Equations (4.27) and (4.28) for Δn and Δp, respectively. The actual equations for Δp and Δn are Equations (4.8) and (4.9), respectively. The model was run again for three data points along the z-axis at iteration numbers 30, 40, and 50. This allows for a comparison to be made between the error for Δn and Δp and the actual equations. Recall that without the error, the computer time would have been fourfold. The carrier lifetimes and carrier densities for the exact equations were compared to the error, and it was found that the error produced a dynamic change to the data. In other words, the error is different at each iteration point. The

results comparing the known error are shown in Table 6.1-2. It would appear from these

results that the actual carrier lifetimes produced by the model should be higher than those

presented.
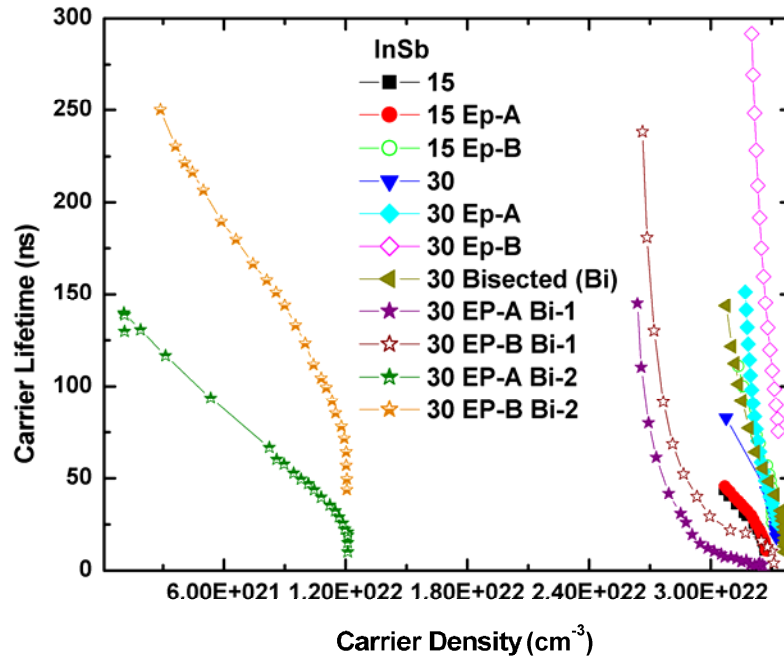
Figure 6.1-16. A comparison for all six models' carrier lifetime for the 15- and 30-μm InSb samples versus the carrier density. The models are (1) 15 (single Block model for the 15-μm InSb sample), (2) 15 Ep-A, 15 Ep-B (Dual-irradiance pattern model for the 15-μm InSb sample) (3) 30 (single Block model for the 30-μm InSb sample), (4) 30 Ep-A, 30 Ep-B (Dual-irradiance pattern model for the 30-μm InSb sample), (5) 30 Bisected (Bisected model for the 30-μm InSb sample), (6) 30 EP-A Bi-1, 30 EP-B Bi-1 (Dual-irradiance pattern and bisected model for the 30-μm InSb sample). Both sections of the 6th model are presented.

Table 6.1-1. **The predicted results from the six models.** **Each measurement indicated with a (*) indicates the measurement was taken at an irradiance of** $328\frac{J}{s-cm^2}$ **and is used in the averaged results.**

Model	Carrier Lifetime (τ-ns)	Carrier Density (N-cm^{-3})
15	10.4 ns *	3.26x10^{22} cm^{-3} *
15 Ep-A	16.7 ns *	3.27x10^{22} cm^{-3} *
15 Ep-B	30.1 ns	3.30x10^{22} cm^{-3} *
30	20.3 ns *	3.32x10^{22} cm^{-3} *
30 Ep-A	33.7 ns *	3.33x10^{22} cm^{-3} *
30 Ep-B	75.7 ns	3.33x10^{22} cm^{-3} *
30 Bisected	11.3 ns	3.36x10^{22} cm^{-3} *
30 Ep-A Bi-1	3.8 ns *	3.26x10^{22} cm^{-3} *
30 Ep-B Bi-1	10 ns *	3.31x10^{22} cm^{-3} *
30 Ep-A Bi-2	22.9 ns *	1.20x10^{22} cm^{-3}
30 Ep-B Bi-2	35 ns	1.21x10^{22} cm^{-3}
Averaged Results At Peak Irradiance *	16.8 ns	3.30 x10^{22} cm^{-3}

Table 6.1-2. **The generated carrier lifetimes from the dual irradiance model, 3rd attempt, with and without the mathematical error.**

Carrier Lifetime (τ-ns)	*Error* 30 Ep-A-B	*Actual* 30 Ep-A-B	Percent *Error* (%)
Iteration 50 (focal point)	9.3 ns	15.4 ns	39.6 %
Iteration 40	22.5 ns	36 ns	37.5%
Iteration 30 (low irradiance)	52.2 ns	64 ns	18.4%

6.2 Conclusion to Modeled Data and Results

It is interesting to observe that the predicted carrier densities for the six models are nearly identical, except those for 30 Ep-A –B Bi-2. Recall that both samples were doped at the same concentration, so that the carrier density per unit volume prior to bleaching would have been the same. After bleaching, at the same irradiances for both samples, it would be expected that the number of generated carriers per unit volume

would have been the same, as well. The minute changes that are predicted are due solely

to the adaptations to the models.

7   Conclusion

In this thesis, the InSb FPA was first introduced along with its limitations concerning low to high irradiances. The physics of the semiconductor material were discussed for completeness. The main points covered were the interactions of the electrons from the conduction band and valence band during the absorption process of photons. These basic concepts and assumptions were used in the mathematical model. Detailed explanations of the experimental apparatus were provided to allow future research to be performed or allow for reproduction of the results by another party without any assumptions. A solid state physics model for the absorption-saturation phenomenon was developed. The model predicts and verifies the experimental data, by allowing a unique carrier lifetime to be found for each unique carrier density, and is temperature and irradiance dependent. The results from the experimental data were presented, and from them, it is evident that InSb up to 30-μm thick can be bleached with relatively low laser output powers. This would lead to optical blooming in an FPA detector system. The results from the experiment were modeled. From the modeled results, the carrier lifetimes and carrier densities were generated for the bleached samples. However, function to accurately represent $\tau(N)$ was not found.

The experimental results of this work have shown that, under high irradiance, InSb material can be bleached from 5 K to 300 K, room temperature. The FPA system may be operated at warmer temperatures to limit the saturation-absorption phenomena, but only to a point. Raising the temperature above 77 K would also limit the FPA's ability to function as a detector. It is also possible to bleach the material with lower irradiances as the material is cooled. Noting that the absorption-saturation phenomenon can occur at

any temperature, provided there is sufficient irradiance, suggests that if at all possible, a prefilter or optical limiter should be used in the detector system. Further discussion of optical limiting and mitigation of absorption-saturation are beyond the scope of this document.

Recommendations for future work entail tweaking the model so that a single carrier lifetime curve is generated, by which, a consistent well-developed equation can be defined that relates the two separate irradiance areas for the dual-irradiance pattern. This equation should include the dependence of the lifetime as a function of the total carrier density while the sample is being bleached. It may be necessary to account for the index of refraction changing within the InSb material, due to the density of carriers increasing with the increases in irradiance. The rest of the data set for other temperatures should also be modeled. This work only included modeled results at liquid nitrogen temperature due to time constraints.

Bibliography

Acton F.S., *REAL Computing made real: preventing errors in scientific and engineering calculations.* New Jersey: Princeton University Press, 1996.

Advanced Research Systems (ARS), *Models LT-3-110 and LT-3B Helitran® Open Cycle Cryogenic Refrigeration System: Technical Manual.* 2001.

Bennett B.R., Soref R.A., and Del Alamo J.A*., Carrier-Induced Chang in Refractive Index of InP, GaAs, and InGaAsP.* IEEE Journal of Quantum Electronics, Vol. 26, No.1, 1990.

Bhattacharya P*., Semiconductor Optoelectronic devices.* New Jersey: Prentice Hall, 1997.

Bohn M., *Error Calculations*, Private conversations, 2007.

Chakraborty P.K., Singh L.J., and Ghatak K.P., *Simple theory of the optical absorption coefficient in nonparabolic semiconductors.* Journal of applied physics, Vol. 95 No. 10, 2004.

Del Mar Ventures. http://www.sciner.com/Opticsland/ZnSe.htm Accessed 2 March 2006.

Farlow, G., *PHY 461: Elementary Solid State Physics*, Course Notes. Wright State University/Department of Physics 2004.

Fox, M., *Optical Properties of Solids.* Great Britain: Oxford University Press, 2001.

Ioffe, *http://www.ioffe.rssi.ru/SVA/NSM/Semicond/InSb/bandstr.html.*Accessed Feb. 2008

Kai-Gui Z., Qing-Yi S., and Jian-Zhong S., *Nonlinear Optical Absorption of Glassy Thin Films Containing InSb Nanocrystals.* Chinese Physics Letters Vol. 18, No. 6, 2001.

Kittel C., *Introduction to Solid State Physics*, New York: Wiley, 1996

Krishnamurthy S., and Guha S., *Accurate calculation of Auger rates in infrared materials.* Journal of Applied Physics Vol. 82, No. 11, 1997.

Krishnamurthy S., Yu Z.G., Gonzalez L. P., and Guha S., *Accurate evaluation of nonlinear absorption coefficients in InAs, InSb and HgCdTe alloys.* Journal of Applied Physics, Vol. *101*, 2007.

Kuzmany H., *Solid-State Spectroscopy an Introduction.* New York: Springer, 1998.

Bibliography (continued)

Levinshtein M., Rumyantsev S. L.; Shur M.;, *Handbook series on semiconductor parameters,* Vol. 2, London: World Scientific, 1996.

Li S.S., *Semiconductor Physical Electronics second edition.* New York: Springer, 2006.

Marciniak M.A., *Optical Characterization of Indium Arsenide Antimonide Semiconductors Grown by Molecular Beam Epitaxy.* Ph.D. Dissertation, Air Force Institute of Technology, 1995.

Mckelvey J.P., *Solid State Physics for Engineering and Materials Science,* Malabar, Fla: Krieger Publishing Company, 1993 .

Michel E., Xu J., Kim J.D., Ferguson I., and Razeghi M., *InSb Infrared Photodetectors on Si Substrates Grown by Molecular Beam Epitaxy.* IEEE Photonics Technology Letters, Vol. 8, No.5, 1996.

Moss T.S., *The Interpretation of the Properties of Indium Antimonide.* Proceedings of the Phyics Society Sec. B **67** 775-782, 1954.

Moss T.S., Burrell G.J., Ellis B., *Semiconductor Opto-Electronics.* New York: John Wiley & Sons, 1973.

Norman J.D., *Characterization of Optical Blooming In Indium Antimonide Focal Plane Arrays Under High Irradiance Conditions.* MS Thesis, Air Force Institute of Technology, 2006.

Nurmikko A.V., *Saturation of Optical Absorption in InSb.* Optics Communications Vol. 16, No. 3, 1976.

Pankove, Jacques, *Optical Processes in Semiconductors,* Dover Publication, Inc., New York, 1971

Ristich, C., Martic, M. *"Counter Precision Guided Munitions"*, 1996, unpublished.

Rogalski, A. "*Infrared Devices and Techniques*", Opt-Electronics Review 10(2), 2002.

Saleh, B.E.A. & Teich, M.C. *Fundamentals of Photonics.* New York: John Wiley & Sons, 1991.

Szafranek I., Amir O., Calahorra Z., Adin A., and Cohen C., *Blooming effects in indium antimonide focal plane arrays.* The Society of Photographic Instrumentation Engineers Proceedings Vol. 3061, 1997.

Bibliography (continued)

Szafranek, L. et al, *"Blooming effects in Indium Antimonide Focal Plane Arrays"*, SPIE Vol. 3061, 1997.

Verdeyen, Joseph T., *Laser Electronics*, Prentice hall, NJ, 1995.

Wertheim G. K., *Carrier Lifetime in Indium Antimonide*. Physical Review, Vol. 104 No. 3, 1956.

Wysocki, Bryant, *"Characterization of Optical Blooming in an InSb Focal Plane Array"*, 2005, unpublished.

Yu Z.G., Krishnamurthy S., Guha S., *Photoexcited-carrier-induced refractive index change in small bandgap semiconductors.* Journal of Optical Society of America Vol. 23, No. 11, 2006.

Zaber, *T-Series Positioning Products User's Manual Firmware 5.00 and Up.* 2008

1. REPORT DATE (DD-MM-YYYY)	2. REPORT TYPE	3. DATES COVERED (From – To)
12-09-2008	Master's Thesis	March 2007 – August 2008

4. TITLE AND SUBTITLE

A STUDY OF THE IRRADIANCE- AND TEMPERATURE-DEPENDENCE OF MID-WAVE-INFRARED (MWIR) ABSORPTION IN INDIUM ANTIMONIDE (InSb)

5a. CONTRACT NUMBER

5b. GRANT NUMBER

5c. PROGRAM ELEMENT NUMBER

6. AUTHOR(S)

Callahan, John M.

5d. PROJECT NUMBER
If funded, enter ENR #

5e. TASK NUMBER

5f. WORK UNIT NUMBER

7. PERFORMING ORGANIZATION NAMES(S) AND ADDRESS(S)
Air Force Institute of Technology
Graduate School of Engineering and Management (AFIT/EN)
2950 Hobson Way, Building 640
WPAFB OH 45433-8865

8. PERFORMING ORGANIZATION REPORT NUMBER
AFIT/GEO/ENP/08-S01

9. SPONSORING/MONITORING AGENCY NAME(S) AND ADDRESS(ES)

LEFT BLANK INTENTIONALLY

10. SPONSOR/MONITOR'S ACRONYM(S)

11. SPONSOR/MONITOR'S REPORT NUMBER(S)

12. DSTRIBUTION/AVAILABILITY STATEMENT

APPOVED FOR PUBLIC RELEASE; DISTRIBUTION UNLIMITED.

13. SUPPLEMENTARY NOTES

14. ABSTRACT

This work entails further investigation of the absorption of photons in indium antimonide (InSb). Previously work at the Air Force Institute of Technology (AFIT) attributed laser blooming effects in InSb focal plane arrays (FPA's) to the Burstein-Moss effect. The contributing effect is from a decrease in the absorption of the InSb material, such that the transmitted optical energy scatters off the integrated circuitry beneath the InSb thin film back into the optical system. To evaluate this, irradiance-dependent laser-absorption experiments were performed on thinned, InSb wafers prior to their FPA fabrication. The samples were illuminated with a focused CO_2 laser at 4.6 μm, and translated along the optical axis to vary the irradiance. A control process to remotely manage the experiment's apparatuses during data collection has been developed utilizing LabView 8.5. The transmission of the InSb sample was measured at different laser powers and temperatures. As the temperature decreases for a determined laser irradiance, it has been observed that the absorption decreases nonlinearly. A model of the absorption-saturation phenomena is also developed so that agreement between the measured and modeled results can be studied for the carrier lifetime and density of carriers.

15. SUBJECT TERMS

16. SECURITY CLASSIFICATION OF:			17. LIMITATION OF ABSTRACT	18. NUMBER OF PAGES	19a. NAME OF RESPONSIBLE PERSON
a. REPORT	b. ABSTRACT	c. THIS PAGE			Dr. M.A. Marciniak, Lt Col, USAF (Ret)
U	U	U	UU	133	19b. TELEPHONE NUMBER (Include area code) (937) 255-6565, ext 4529 (Michael.Marciniak@AFIT.edu)